

Formation Mechanisms of Combustion Chamber Deposits

by

Christopher O'Brien

A.B. in Chemistry  
Princeton University, 1994

Master of Science  
Massachusetts Institute of Technology, 1996

Submitted to the Department of Mechanical Engineering  
in Partial Fulfillment of the Requirements for the Degree of

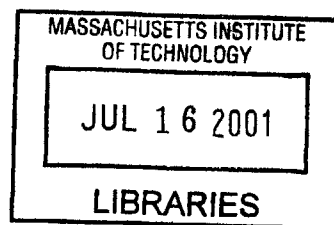
Doctor of Philosophy

at the  
Massachusetts Institute of Technology  
January, 2001

[February 2001]

© 2001 Massachusetts Institute of Technology  
All rights reserved

**BARKER**



Signature of Author \_\_\_\_\_

Department of Mechanical Engineering  
January 19, 2001

Certified by \_\_\_\_\_

Simone Hochgreb  
Lecturer, Department of Mechanical Engineering  
Thesis Supervisor

Accepted by \_\_\_\_\_

Ain A. Sonin  
Chairman, Department Committee on Graduate Students



# Formation Mechanisms of Combustion Chamber Deposits

by

Christopher O'Brien

Submitted to the Department of Mechanical Engineering  
on January 19, 2001 in Partial Fulfillment of the  
Requirements for the Degree of Doctor of Philosophy

## Abstract

Combustion chamber deposits are found in virtually all internal combustion engines after a few hundred hours of operation. Deposits form on cylinder, piston, and head surfaces that are in contact with fuel-air mixture during the engine cycle. The effects of deposits include increased engine-out NO<sub>x</sub> emissions, octane requirement increase, and changes in flame speed and thermal efficiency.

A framework is developed for examining the physical and chemical processes that contribute to the formation of combustion chamber deposits. First, a hypothesis for the general mechanism of deposit formation is developed from a review of previous work on this issue. The key features of this mechanism are formation of deposit precursor species from fuel and air as the flame quenches at the engine wall, diffusive and convective transport of these species to the wall, and condensation or adsorption at the wall surface. The experimental system and methodology developed in this work are meant to provide insight into the interactions between these processes, and in particular to study the chemical mechanisms that contribute to the formation of deposit precursor species. A cooled low pressure flat flame burner is used to produce steady-state propane-air flames doped with toluene, a known deposit forming species. Profiles of concentrations and temperature are measured using infrared spectroscopy and gas chromatography techniques. In conjunction with the experiments, a one-dimensional numerical model is developed, capable of simulating flame quenching with deposition over a range of conditions extending from the low pressure, steady state burner experiments to high pressure, rapid transient engine conditions, using chemical mechanisms of precursor formation that may be determined experimentally.

Modeling of deposition with simplified chemical mechanisms reveals that deposition by condensation can reproduce trends observed in experiments by other researchers; however, adsorption could still be a contributing factor. Experimental observations of toluene-doped flames show the formation of oxygenated compounds such as benzaldehyde and benzofuran, which are likely deposit precursor candidates. The methodology developed in this thesis shows promise for determining deposit precursor identities and formation mechanisms for important fuel components, and for clarifying the role of gas-phase processes in the formation of combustion chamber deposits.

Thesis Supervisor: Simone Hochgreb  
Title: Lecturer, Department of Mechanical Engineering



## Acknowledgements

Let me begin these acknowledgements with a disclaimer: I couldn't possibly succeed in thanking everyone who deserves to be recognized here. In my seven years at MIT, so many people have enriched my experience, both in academic life and in the rest of life, that it would be futile to list even a fraction of them. Nevertheless, I'll go ahead and do just that.

The members of my thesis committee, Simone Hochgreb, Jim Keck, Ahmed Ghoniem and Jack Howard, played their roles well. They were never at a loss for questions and suggestions, and the committee meetings always resulted in lively discussion and dissection of the results.

Tom Dorsey and Art Lafleur at the Center for Environmental and Health Sciences at MIT were instrumental in making the GC/MS analysis possible. The excellent results from the sampling and gas chromatography work formed a cornerstone of this thesis, and would not have been possible without their experience and assistance.

The Sloan Automotive Laboratory has been an interesting and at times amusing place to spend the last few years. There have been few constants over my tenure as a Sloan Lab student, save for the consistent good nature and willingness to help of my colleagues. As I leave the lab, a new generation is entering; I hope that this tradition will continue for them.

Certain invaluable members of the lab deserve special recognition; without the constant and skillful assistance of Nancy Cook, Brian Corkum, and Susan Lutin, it would certainly have taken me even longer to complete my doctorate, and would have been a much less enjoyable process. Brian in particular brought a wealth of experience to the process of building the flat flame burner apparatus with me, which resulted in a wonderfully reliable and productive laboratory for the project.

Several students at the Sloan Lab have been particular inspirations to me. Mike Norris, Jon Fox, Alan Shihadeh and Patia McGrath all helped me to believe that graduate school could be an extension of one's life, rather than a suspension of it. I hope that I have learned something for each of my fellow students at the lab; these will be some of the most important lessons I bring with me into my future endeavors.

These acknowledgements would be incomplete without recognition of Leslie Regan and Joan Kravit in the Mechanical Engineering Graduate Office, both of whom have been consistently available, helpful, and friendly, despite the endless string of unique administrative challenges I brought to their door.

My family and friends have been a constant support throughout this part of my life. My parents and sister, Bill, Sue and Kathleen O'Brien, have given me the character to do this, and have been there for me for the whole (long) process. My mother-in-law Birte Jackson has been a great friend during this time, which sometimes just meant not waking the tired graduate student who kept falling asleep on the couch. I have also been lucky to have an excellent group of friends in Boston and elsewhere to help forget grad school, consider it from a different angle, or just live through it, as necessary.

This thesis is dedicated to Kristine Forssén O'Brien, my wife and best friend, who has been a companion, critic, and colleague, who reminded me when I was being unreasonable, and when being unreasonable was the only sensible thing to do, and for whom I have boundless love and respect. I have learned more and found more inspiration from her than any degree could possibly represent.



## Table of Contents

Chapter 1 – Introduction .....	19
1.1 Combustion Chamber Deposits .....	19
1.2 Research Methods and Unanswered Questions .....	20
1.3 Project Motivations and Goals.....	21
1.4 Thesis Outline.....	22
1.5 References .....	22
Chapter 2 – Background and Previous Work.....	23
2.1 History of Combustion Chamber Deposit Research.....	23
2.2 Composition of Combustion Chamber Deposits.....	23
2.3 Morphology and Physical Properties.....	24
2.4 Effects of Combustion Chamber Deposits on Engine Performance and Emissions.....	25
2.5 Effects of Engine and Fuel Parameters on Deposit Formation Rates .....	27
2.6 Current Theories of Combustion Chamber Deposit Formation .....	29
2.7 References .....	30
Chapter 3 – Deposit Formation Hypothesis and Project Objectives.....	33
3.1 Mechanistic Inferences from Literature Data.....	33
3.2 Deposit Formation Mechanism Hypothesis .....	36
3.3 Non-Dimensional Model and Characteristic Parameters.....	38
3.4 Open Questions in Combustion Chamber Deposit Formation .....	40
3.5 Objectives of this Study .....	41
3.6 Joint Numerical - Experimental Methodology.....	42
3.7 Intended Contributions to Combustion Chamber Deposit Research.....	45
3.8 References .....	46
Chapter 4 – Numerical Analysis Methodology .....	47
4.1 Numerical Analysis Goals .....	47
4.2 One-Dimensional Approximation .....	48
4.3 Model Definitions and Assumptions .....	50
4.4 Governing Equations and Model Formulation.....	51
4.5 Boundary Conditions and Deposition Model.....	52
4.6 Mass-Based Coordinate Transform.....	52
4.7 Adaptive Spatial Mesh Redistribution.....	53
4.8 Discretization and Numerical Solution Techniques.....	54
4.9 Code Structure and Organization.....	55
4.10 References .....	56

## Table of Contents

Chapter 5 – Numerical Simulation of Quenched Flame Deposition.....	57
5.1 Objectives of the Modeling Study .....	57
5.2 Simulation of Atmospheric Pressure Flame Quenching with Deposition.....	57
5.3 Single Step Precursor Formation Chemistry Approximation.....	60
5.4 Deposition from Single Flame Quench Events.....	61
5.5 Comparison with Literature Data .....	66
5.6 Conclusions .....	66
5.7 References .....	67
Chapter 6 – Flat Flame Burner Apparatus and Diagnostics .....	69
6.1 Experimental Objectives.....	69
6.2 Flat Flame Burner System .....	69
6.3 Vacuum System and Pressure Control .....	73
6.4 Flow and Temperature Measurements and Control.....	74
6.5 Dopant Vaporization and Injection System.....	75
6.6 Flame Temperature Measurements and Radiation Corrections.....	76
6.7 Observed Flame Properties and Operational Limits.....	77
6.8 References .....	79
Chapter 7 – Gas Sampling and Analysis Techniques.....	81
7.1 Gas Sampling Apparatus and Probe Sampling Considerations.....	81
7.2 Microprobe Sampling Apparatus.....	81
7.3 FT-IR Analysis of Major Species Concentrations .....	84
7.4 Thermal Adsorption / Desorption Sampling and GC/MS Analysis for Minor Species Identification and Quantification.....	87
7.5 Error Analysis of Species Concentration Measurements.....	90
7.6 References .....	92
Chapter 8 – Experimental Validation via Propane-Air Flame Measurements .....	93
8.1 Objectives of Validation Experiments.....	93
8.2 Experimental Method.....	93
8.3 Minor Species Storage Effects in the Sampling System.....	94
8.4 Observed Species and Temperature Profiles in Propane-Air Flames .....	98
8.5 Numerical Modeling of Burner Flames.....	102
8.6 Numerical-Experimental Comparison.....	103
8.7 Conclusions .....	106
8.8 References .....	107
Chapter 9 – Experimental Observations of Toluene Oxidation Chemistry in the Pre-Flame Zone .....	109
9.1 Experimental Objectives.....	109
9.2 Experimental Method.....	109



9.3	Observed Species and Temperature Profiles in Toluene-Doped Propane-Air Flames...	111
9.4	Identification of Deposit Precursor Candidate Species .....	121
9.5	Suggested Toluene Partial Oxidation Mechanism .....	122
9.6	Reaction / Diffusion / Convection Analysis for Identified Precursor Candidates .....	122
9.7	Conclusions .....	124
9.8	References .....	124
Chapter 10 – Numerical Simulation of Deposition with Toluene Fuel .....		125
10.1	Mechanistic Evidence from Experiments.....	125
10.2	Comparison of Observed Species Profiles with Literature Mechanisms.....	125
10.3	Proposed Mechanism of Toluene Partial Oxidation in the Quench Layer.....	126
10.4	Numerical Simulation of Toluene Partial Oxidation in Propane Flames.....	128
10.5	Simulated Deposition with Toluene Fuel.....	130
10.6	Conclusions .....	135
10.7	References .....	135
Chapter 11 – Conclusions.....		137
11.1	Introduction .....	137
11.2	Experimental Conclusions .....	137
11.3	Numerical Analysis Conclusions.....	138
11.4	Comments on Methodology.....	139
11.5	Future Directions.....	140
11.6	Summary.....	141
Appendix I – Simplified Oxidation Mechanism for Light Hydrocarbons .....		143
I.1	Introduction .....	143
I.2	Mechanism .....	143
I.3	References .....	146
Appendix II – Propane Oxidation Mechanism .....		147
II.1	Introduction.....	147
II.2	Mechanism.....	147
II.3	References.....	157

Table of Contents

## List of Figures and Tables

Table 2.1	Elemental composition of combustion chamber deposits. ....	24
Table 2.2	Effects of combustion chamber deposits on emissions of criteria pollutants. ....	27
Table 2.3	Effects of various engine and fuel properties on the equilibrium mass, formation rate and chemical structure of combustion chamber deposits, along with suggested mechanisms for the observed effects. ....	28
Figure 3.1	Deposit mass and measured wall temperatures for two-hour engine tests at varying fuel-air equivalence ratios. ....	34
Figure 3.2	Hypothesized mechanism for combustion chamber deposit formation. ....	36
Figure 3.3	Schematic diagram of study methodology, using a detailed chemistry numerical simulation to connect experimentally observed chemical mechanisms with deposition at engine operating conditions. ....	43
Figure 4.1	Schematic representation of the one-dimensional modeling domain. The surface at the left boundary could represent the piston top or any of the other head surfaces where combustion deposits form, particularly in the end-gas region. The right boundary should extend sufficiently far past the flame front to ensure negligible gradients in temperature and species concentrations. ....	49
Figure 4.2	Structure and data flow in the numerical simulation code. ....	55
Figure 5.1	Typical initial condition species and temperature profiles for the ethylene/toluene/air flame quenching simulations. Nitrogen and several minor species are not shown. The "precursor" species refers to a hypothetical deposit precursor whose physical properties may be varied to model a range of different input fuels. ....	59
Table 5.1	Range of parameters used in the ethylene/toluene/air flame quenching simulations. ....	61
Figure 5.2	Time evolution of temperature profiles in a quenching ethylene / toluene / air flame. ....	62
Figure 5.3	Concentration profiles of toluene and the deposit precursor species at several times during the flame quench event (see temperature profile in Figure 5.2.) ....	63

List of Figures and Tables

Figure 5.4	Deposition rate and integrated total deposition at the wall surface during the flame quenching process shown in Figures 5.2 and 5.3. ....	64
Figure 5.5	Deposit mass fraction versus reduced partial pressure of toluene for the simulations described in Table 5.1. Primary y axis is in units of deposit mass fraction (see equation 5.3); secondary y axis is converted to units of mg/mole for comparison with the data of Price, <i>et al.</i> ....	65
Figure 6.1	Schematic diagram of the flat flame burner apparatus. ....	70
Figure 6.2	Copper burner plate (3:4 scale). Total plate thickness is 1/4". The central region of the plate is drilled with 1481 holes, 3/64" in diameter, in a centered grid with center-to-center spacing of 0.09". ....	71
Figure 6.3	The flat flame burner mounted on the vacuum chamber baseplate. ....	72
Figure 6.4	Vacuum chamber and diagnostic feedthrough systems. Viewing port not shown (located at 90° around the chamber circumference from the feedthrough flanges, and at the same height). ....	73
Figure 6.5	Dopant vaporization and delivery system. ....	75
Figure 6.6	Uncorrected and corrected temperature profiles from a propane air flame, at $\phi = 1.0$ , $p = 165$ millibar, and unburned gas velocity of 15 cm/s. ....	77
Figure 6.7	Typical propane-air flame, at an equivalence ratio of 1.0, operating pressure of 70 millibar, and surface temperature of 60 °C. Horizontal line corresponds to burner surface at the flame center; large scale divisions correspond to 1 cm. ....	78
Figure 6.8	Measured radiation-corrected temperature profiles for several stoichiometric propane - air flames, at differing chamber pressures and unburned gas velocities. ....	79
Figure 7.1	Quartz microprobe used for gas sampling. Probe diameter at the tip is less than 1 mm. ....	81
Figure 7.2	Schematic diagram of the quartz microprobe sampler system and associated sample train with infrared spectroscopy cell and hydrocarbon adsorption traps for gas chromatography sample storage. ....	82
Figure 7.3	Mass flow through the sampling system as a function of pressure and temperature at the probe tip. ....	83

Figure 7.4	Reaction quenching as a function of pressure and temperature at the probe tip. ....	84
Figure 7.5	A typical FTIR spectrum of a sample taken from the flame zone, showing the calibration regions for major species. ....	85
Figure 7.6	Calibration curve and linear fit for propane in the 2809 - 3040 $\text{cm}^{-1}$ range. ....	86
Figure 7.7	Calibration curve and linear fit for carbon monoxide in the 2071 - 2141 $\text{cm}^{-1}$ range. ....	86
Figure 7.8	Calibration curve and linear fit for carbon dioxide in the 2322 - 2348 $\text{cm}^{-1}$ range. ....	86
Figure 7.9	Calibration curve and linear fit for carbon dioxide in the 3695 - 3700 $\text{cm}^{-1}$ range. ....	86
Figure 7.10	Schematic diagram of the thermal desorber and gas chromatograph system with mass spectrometer detector. The sample is first transferred from the (heated) sample trap to the (cooled) secondary trap; the secondary trap is then connected to the gas chromatograph and rapidly heated, injecting the sample onto the column. ....	88
Figure 7.11	Typical chromatogram from a flame with fuel composition of 95% propane, 5% toluene (molar basis). Oven temperature is maintained at 50 °C for the first ten minutes, and then ramped up at 8 °C per minute to 300 °C. ....	89
Figure 7.12	Sample mass spectrum from the chromatogram shown in Figure 7.11. Spectrum corresponds to a retention time of 5.2 minutes; the species is identified as benzaldehyde ( $\text{C}_6\text{H}_5\text{CHO}$ , structure shown above). ....	89
Table 7.1	Gas sampling and analysis error sources and magnitudes. ....	90
Table 8.1	Flame characteristics for propane-air flame validation experiments. ....	94
Figure 8.1	Evidence of hydrocarbon retention in the GC/MS sampling system (initial configuration). The first chromatogram is of samples taken in the pre-flame zone of a rich flame ( $\phi = 1.25$ ); the second is from the product region of a lean flame ( $\phi = 0.9$ ), taken after the first sample; the third is a sample of air only, taken immediately following the second sample. Each peak in the chromatograms represents a hydrocarbon species. The significantly larger	

	peaks in the third chromatogram are due to a much larger mass flow rate of air through the sample traps. ....	96
Figure 8.2	Elimination of hydrocarbon retention in the GC/MS sampling system. These chromatograms are from the same set of tests as Figure 8.1; the sampling configuration was altered to place the adsorption traps upstream of the sampling pump. The differences suggest that almost all the peaks in the chromatograms shown in Figure 8.1 were due to species adsorbed within the sample pump system from previous samples. ....	97
Figure 8.3	Temperature and species profiles from a propane-air flame at $\phi = 0.90$ . Filled symbols in the plots represent directly measured quantities; open symbols represent concentrations calculated via mass balance. The flame is shown in the image to the right. The horizontal line marks the burner surface at the flame center; each large scale division corresponds to 1 cm. Shadow at flame center is a bolt between flame and camera. ....	99
Figure 8.4	Temperature and species profiles from a propane-air flame at $\phi = 1.00$ . Filled symbols in the plots represent directly measured quantities; open symbols represent concentrations calculated via mass balance. The flame is shown in the image to the right. The horizontal line marks the burner surface at the flame center; each large scale division corresponds to 1 cm. Shadow at flame center is a bolt between flame and camera. ....	100
Figure 8.5	Temperature and species profiles from a propane-air flame at $\phi = 1.20$ . Filled symbols in the plots represent directly measured quantities; open symbols represent concentrations calculated via mass balance. The flame is shown in the image to the right. The horizontal line marks the burner surface at the flame center; each large scale division corresponds to 1 cm. Shadow at flame center is a bolt between flame and camera. ....	101
Figure 8.6	Minor species concentrations measured via GC/MS for the flame shown in Figure 8.5. The C4+ series represents the total concentration of smaller partially unsaturated hydrocarbons (C4 - C6) that are not resolved fully in the chromatogram. ....	102
Figure 8.7	Comparison of experimental results and direct numerical simulation of a propane-air flame at $\phi = 0.9$ . The rest of the data for this flame is found in Figure 8.3. ....	104

Figure 8.8	Comparison of experimental results and direct numerical simulation of a propane-air flame at $\phi = 1.0$ . The rest of the data for this flame is found in Figure 8.4. ....	104
Figure 8.9	Comparison of experimental results and direct numerical simulation of a propane-air flame at $\phi = 1.2$ . The rest of the data for this flame is found in Figure 8.5. ....	105
Table 8.2	Heat loss versus heat release for burner-stabilized propane-air flames. ....	106
Table 9.1	Flame characteristic parameters for toluene-doped propane flame experiments. ...	110
Table 9.2	Observed toluene reaction products from toluene-doped propane-air flames. ....	111
Figure 9.1	Major species and temperature profiles for a toluene-doped propane flame at $\phi = 0.86$ , pressure of 144 millibar, and unburned gas velocity of 20.5 cm/s. Flame image is shown at right; shadow in image is due to a bolt between the flame and camera. ....	113
Figure 9.2	Minor species profiles for a toluene-doped propane flame at $\phi = 0.86$ (see Figure 9.1). ....	114
Figure 9.3	Major species and temperature profiles for a toluene-doped propane flame at $\phi = 0.96$ , pressure of 143 millibar, and unburned gas velocity of 20.5 cm/s. Flame image is shown at right; shadow in image is due to a bolt between the flame and camera. ....	115
Figure 9.4	Minor species profiles for a toluene-doped propane flame at $\phi = 0.96$ (see Figure 9.3). ....	116
Figure 9.5	Major species and temperature profiles for a toluene-doped propane flame at $\phi = 1.00$ , pressure of 144 millibar, and unburned gas velocity of 20.3 cm/s. Flame image is shown at right; shadow in image is due to a bolt between the flame and camera. ....	117
Figure 9.6	Minor species profiles for a toluene-doped propane flame at $\phi = 1.00$ (see Figure 9.5). ....	118
Figure 9.7	Major species and temperature profiles for a toluene-doped propane flame at $\phi = 1.10$ , pressure of 143 millibar, and unburned gas velocity of 20.5 cm/s. Flame image is shown at right; shadow in image is due to a bolt between the flame and camera. ....	119

List of Figures and Tables

Figure 9.8	Minor species profiles for a toluene-doped propane flame at $\phi = 1.10$ (see Figure 9.7). .....	120
Figure 9.9	Comparison of benzaldehyde, benzofuran, and styrene profiles resulting from different equivalence ratios. ....	121
Figure 9.10	Calculated fluxes at the wall surface for several experimentally observed toluene derivatives. All fluxes are in moles/m <sup>2</sup> /s. Benzene and ethylbenzene demonstrate fluxes away from the wall, this is physically unreasonable for species produced in the flame, and indicates that the assumption of insignificant reaction in the area before the first measurable concentrations is not valid for these species; styrene, benzaldehyde and benzofuran show fluxes towards the wall. ....	123
Figure 10.1	Simplified reaction mechanism for the partial oxidation of toluene in flame quench zones. ....	127
Table 10.1	Reactions and rate coefficients for the mechanism shown in Figure 10.1. (Subset of Emdee, Brezinsky and Glassman, 1992). Units of A are moles, seconds, cm and K, depending on the reaction stoichiometry; E <sub>a</sub> units are cal/mole. Reaction rates are calculated as in Equation 4.2. ....	128
Figure 10.2	Comparison of measured and calculated toluene partial oxidation product concentrations in a toluene-doped propane-air burner flame, with toluene at 10 percent by carbon, $\phi = 1.0$ , and unburned gas flow of 3.6 mg/m <sup>2</sup> /s. ....	129
Figure 10.3	Saturated vapor pressure of benzaldehyde as a function of temperature. ....	131
Figure 10.4	Initial condition for simulation of flame quenching and deposition with toluene / benzaldehyde chemistry. ....	132
Figure 10.5	Time evolution of toluene, benzaldehyde and temperature profiles during a flame quench event at a wall temperature of 300 K. ....	133
Figure 10.6	Calculated deposition fluxes and integrated deposition amounts for benzaldehyde as a function of wall surface temperature. The deposition for the T <sub>w</sub> = 340 K case is within the numerical error. ....	134







## 1.1 Combustion Chamber Deposits

Combustion chamber deposits are found in almost all internal combustion engines – and there are many millions of internal combustion engines in use today. When a deposit-free engine is operated on gasoline fuel, carbonaceous deposits begin to build up on the surfaces of the cylinder head and piston that are exposed to the burning fuel-air mixture. The process will continue until the deposits reach an equilibrium thickness after a few hundred hours of engine operation, leaving a stable deposit layer that impacts the engine performance and emissions in numerous ways.

Some of the most significant effects of combustion chamber deposits on the engine occur via a very straightforward physical mechanism: insulation of the cylinder. The deposits have much lower thermal conductivity than the engine walls; hence, the presence of deposit layers causes the temperatures in the cylinder to be slightly elevated, and increases the chances of early combustion of the fuel-air mixture, or “knock.” Knock has been a persistent challenge in engine design; the only available solutions have been to use higher octane fuels, which are less likely to combust spontaneously, or to lower the engine compression ratio, which decreases temperatures before combustion. The difference in the octane number of the fuel required by an engine with deposits and that of the fuel for the same engine when clean is known as the octane requirement increase, or ORI. Increasing the octane number of gasoline requires expensive additional refining of the fuel, and reduction of compression ratio decreases the efficiency of the engine; nevertheless, both measures are used in modern automobiles.

An estimate of the societal costs of combustion chamber deposits can help to put the problem in perspective. The standard compression ratio decrease to counteract the effects of deposits is about 0.3 to 0.5; this corresponds to a decrease in BMEP (a measure of engine work output) of about two percent, or a reduction in vehicle fuel efficiency of approximately one percent. In itself, this seems like a minimal effect, and is essentially imperceptible to consumers given U.S. gasoline prices. However, 260 billion liters of fuel were consumed by automobiles in

the United States in 1996 (AAMA, 1998). A one percent improvement in average fuel economy gained by elimination of deposits in the United States alone would save 2.6 billion liters of fuel; this also corresponds to elimination of 6.5 million tons of carbon dioxide emissions - 0.1 percent of the *world's* annual man-made CO<sub>2</sub> output.

Despite the clear costs of these engine design workarounds for combustion chamber deposits, no other viable option is currently available for addressing the problem of deposits in gasoline spark-ignition engines. Fuel additives that have proved effective against other types of engine deposits have little impact on combustion chamber deposits; in some cases, these additives cause increased deposition in the combustion chamber. Also, in addition to loss of efficiency, there are other effects of combustion chamber deposits, such as increased engine-out emissions, that still need to be addressed. In order to develop long term solutions to these issues, a better understanding of combustion chamber deposits and the mechanisms for their formation is required.

## **1.2 Research Methods and Unanswered Questions**

There has been active research work on combustion chamber deposits in the auto and oil industries for over fifty years. A wide range of studies have been performed, including measurements of deposit weight after engine tests, use of radioactive tracer compounds to follow molecules from the fuel into deposits, and observation of rates of deposit formation in highly specialized flame experiments, to name a few. While much has been determined about the nature and physical properties of deposits, and some basic effects of engine and fuel characteristics on deposition are known, there are still major questions to be answered. The most fundamental of these is the mechanism by which the fuel and air in the engine produce combustion chamber deposits. Part of the reason for this is the inherent difficulty in developing conclusions about molecular level events in engine combustion chambers from long-term tests with large degrees of variation in the engine operating conditions, as is the case with most fleet tests or typical engine deposit studies. In the past few years, more controlled experiments have begun to be performed, but they remain largely limited to the physical processes of deposition, and interaction of the gas

phase and the cylinder surfaces. Key gas-phase only processes that contribute to deposition, such as the formation of depositing molecules from fuel and air in the engine quench layer, remain unexamined, and leave a number of open questions in the mechanism of deposit formation.

### **1.3 Project Motivations and Goals**

The aim of this work is to study the formation mechanisms of combustion chamber deposits from a fundamental viewpoint, concentrating on the chemical and physical processes that contribute to deposit formation in the engine quench zones and at the cylinder surface. In particular, we focus on the chemical interactions occurring in quenching flames that can lead to the production of molecular species that are likely to cause deposits. This is a challenging objective, requiring the measurement of concentration profiles of chemical species between a flame and a cooled surface. This region is at most only a few millimeters in length, even at low operating pressures. The concentration measurements can be made with the required accuracy only at low pressure, steady state conditions, which are significantly removed from the high pressure, transient regimes that prevail in combustion engine cylinders.

To maintain relevance to engine systems despite the restricted range of experimental conditions available, we employ a joint numerical - experimental approach, in which the experimental and practical regimes are connected through a numerical simulation. The simulation utilizes experimental data on the gas-phase chemistry and transport mechanisms involved in deposit formation as the basis for numerical modeling of the transient physical and chemical processes that contribute to deposition at realistic conditions. A large portion of the work of this thesis is dedicated to the development of this approach; thus, our goals are not only to provide insights into the formation of combustion chamber deposits, but also to provide productive avenues and methodologies for future research into the fundamental aspects of this problem.

## 1.4 Thesis Outline

The thesis begins with a brief review of previous research on the various aspects of the combustion chamber deposit problem. Following this, the specific hypothesis of deposit formation, goals of the work, and joint numerical - experimental methodology are presented. The numerical model and experimental apparatus are introduced separately: first, the development and implementation of the numerical simulation, along with preliminary application of this tool to deposition from quenching flames, followed by the details of the experimental setup, diagnostics and calibration, and validation experiments. The last part of the thesis describes the experimental results from observation of toluene-doped propane flames, and their implications for the mechanisms of combustion chamber deposit formation from gasoline components. The mechanistic information derived from these experimental results is used in combination with the numerical simulation to compare deposition predicted by the deposit formation hypothesis postulated herein with literature data on deposit formation rates.

## 1.5 References

American Automobile Manufacturer's Association (AAMA), *Motor Vehicle Facts and Figures* 98, Government Affairs Division of the AAMA (1998).

## **2.1 History of Combustion Chamber Deposit Research**

Combustion chamber deposits in both spark ignition and diesel engines have been investigated for most of this century. As early as 1925, Orelup and Lee described the effects of knock-limited engine performance due to deposits:

To avoid the knocking, the operator must run with the spark retarded, thus losing power. There is an increased fuel consumption and a tendency for the engine to overheat. The car is no longer able to climb steep hills in high gear and in general lacks that desirable activity known as 'pep.' (Orelup and Lee, 1925)

Since that time, despite both evolutionary and revolutionary changes in engine design and fuel composition, combustion chamber deposits and their associated effects have persisted as omnipresent features of internal combustion. Wide ranges of studies have been applied to this issue, from fleet performance tests of various cylinder head designs or fuel additives to detailed deposit growth rate studies in purpose-built deposition rigs. The chemical and physical properties of deposits have been thoroughly characterized, and their various impacts on engine performance, efficiency and emissions have been cataloged. Simultaneously, improvements in engine design and increases in fuel octane ratings (first via lead additives, and later through advances in fuel refining methods) have tamed combustion chamber deposits, reducing their variability and virtually eliminating their observable performance effects (i.e. loss of 'pep'). This chapter will summarize some of the major results of the work done over these seventy-five years, focusing on chemical and physical characterization, engine performance and emissions effects, and deposit formation mechanisms. In general, the results discussed in this chapter apply to relatively modern low oil consumption engines operating on unleaded fuels.

## **2.2 Composition of Combustion Chamber Deposits**

Deposits are formed largely from the fuel, with some minor contributions from the lubricant, as is demonstrated by the small levels of lubricant-derived metals in the final deposit structure (see Table 2.1). There are several characteristics that differentiate these deposits from

Element	Weight Percent	X-to-C Molar Ratio
C	60 - 70	1.00
H	3 - 6	0.60 - 1.00
O	16 - 25	0.20 - 0.30
N	1 - 2.5	0.01 - 0.03
Other (Zn, Ca, P)	0 - 2.5	< 0.02

**Table 2.1.** Elemental composition of combustion chamber deposits.  
(Nagao *et al.*, 1995; Kalghatgi, 1995).

weight, whereas intake system deposits have oxygen contents ranging from 10 to 15 weight percent (see Table 1).

### 2.3 Morphology and Physical Properties

The structure and physical properties of combustion chamber deposits vary widely with engine conditions, but do share some unifying properties. Deposits have been found in general to be composed of volatile carbonaceous materials similar to bituminous coal, containing amorphous and highly porous carbon (Ebert *et al.*, 1985). The structure consists of an oxygen-containing hydrocarbon backbone, along with more volatile, hydrogen-rich adsorbed species.

Deposits have been observed to exhibit layered structures, with lower volatility constituents at the outer levels; initial deposits have lower hydrogen-to-carbon ratios and less oxygen content than those that form at later times when part of the deposit layer has already developed (Gebhard *et al.*, 1985). Inorganic compounds, likely to be derived from the oil, are also found at higher concentrations in the outer layers of the deposit (Nakamura *et al.*, 1985).

In micrographic studies of deposit formation with toluene fuel, Cheng (1996) observed deposit structures consisting of a liquid-like first layer, with solid layers forming on top. The liquid layer was found to form very evenly on the engine wall surface.

The most critical physical properties of deposits with respect to their impact on the thermal environment of the cylinder are heat capacity and thermal conductivity. Thermal conductivity has been measured to range from 0.17 to 0.8 W/m/K, with heat capacities from 0.84 to 1.84 kJ/kg/K. (Harder and Anderson, 1988; Hopwood *et al.*, 1998).

those that form on the intake valves and ports. The most obvious of these is elemental composition; combustion chamber deposits contain 16 to 25 percent oxygen by



## 2.4 Effects of Combustion Chamber Deposits on Engine Performance and Emissions

The effects of combustion chamber deposits on engine performance have been studied extensively; they include octane requirement increase (ORI), decreased volumetric efficiency, increased thermal efficiency due to insulation of the cylinder, and physical interference with valve closing or with piston motion (the latter is known as combustion chamber deposit interference (CCDI) or "carbon rap").

Octane requirement increase for spark-ignition engines is the most well known effect of combustion chamber deposits. As deposits build up on combustion chamber surfaces, the minimum fuel octane number needed to avoid engine knock increases. In modern engines, this increase is approximately 4 to 5 octane numbers on average as the deposits build up to their equilibrium thickness (Kalghatgi, 1995). Several mechanisms that contribute to ORI have been identified. Two of these have to do with the thermal properties of the deposits. Firstly, their low thermal conductivity (0.17 - 0.8 W/mK) leads to higher wall temperatures at a given coolant temperature, and secondly, their high heat capacity (0.84 - 1.84 kJ/kgK) allows heat to be stored in the deposit layer during combustion and released back into the cylinder during the intake process. Both of these mechanisms will increase the fresh charge temperature in the cylinder, thus increasing the likelihood of autoignition. Additionally, it has been suggested that the deposit layer may either physically or chemically adsorb combustion initiators such as hydrocarbon radicals during the combustion stroke and later release these species to the fresh charge as the cylinder pressure decreases (Adamczyk and Kach, 1986). In contrast to the thermal effects, this chemical ignition is difficult to observe experimentally, due to the small species concentrations and rapid timescales involved.

Some of the most important impacts of combustion chamber deposits on engine performance from the standpoint of modern engine design are potential increases in engine-out emissions of pollutants such as unburned hydrocarbons and nitric oxides. The importance of these emission level changes lies not in their magnitudes, but in their unpredictability. This makes the task of engine control and exhaust cleanup more difficult. Also, since up to half of automotive pollutant emissions in some areas are due to "high emitters," that is, vehicles with

malfunctioning or disabled emissions control systems, which usually represent less than ten percent of the total vehicle population, it is important to eliminate as many sources of engine-out emissions as possible.

The one category of pollutant for which the effect of combustion chamber deposits is clear is the nitric oxides, or  $\text{NO}_x$ . Formation of  $\text{NO}_x$  during the engine cycle has been shown to have a strong dependence on mean gas temperature in the cylinder, increasing by over 44 percent with an increase in burned gas temperature from 2000 K to 2050 K (Studzinski *et al.*, 1993). Thus, the increase in gas temperatures due to the insulating and heat-storage effects of the deposits can be expected to increase engine-out  $\text{NO}_x$  emissions. Statistically significant increases in tailpipe  $\text{NO}_x$  emissions with increasing deposit thickness have been observed experimentally (Bitting *et al.*, 1994).

Emissions of unburned hydrocarbons and carbon monoxide have also been suggested to increase with deposit formation, but the experimental data is unclear for these species. Bitting *et al.* (1994) observed increases of both hydrocarbon and CO emissions in road tests, but found that the changes were not statistically significant. Harpster *et al.* (1995) reported an approximate increase of 25 percent in unburned hydrocarbon emissions for a deposited engine compared to the same engine before deposit formation, but the experimental measurements were only repeatable to within 15 percent of the mean. Kalghatgi (1997), in tests of three similar engines, found combustion chamber deposits to increase hydrocarbon emissions from two of the three while decreasing the emissions from the third. Adding to the uncertainty over the effect of deposits on unburned hydrocarbons is the fact that there are competing mechanisms by which the deposits could either increase or decrease the emission level. The increase in gas temperatures and reduction in crevice volumes should both serve to decrease hydrocarbon emissions, while adsorption and later release of hydrocarbon species by the deposit layer could lead to an increase in emissions.

Table 2.2 lists the effects of combustion chamber deposits on major pollutant emissions, along with the suggested mechanisms by which the deposits change emission levels of each species.

Species	Effect of Deposits	Certainty	Mechanism(s)
Unburned Hydrocarbons	Increase	Low	Absorption/Desorption by deposit layer (increase) Insulation/Heat storage (decrease) Crevice volume reduction (decrease)
Carbon Monoxide (CO)	Increase	Low	Poor mixture control
Nitric Oxides (NO <sub>x</sub> )	Major Increase	High	Insulation and heat storage in cylinder
Carbon Dioxide (CO <sub>2</sub> )	Decrease	High	Insulation leading to higher thermal efficiency

**Table 2.2.** Effects of combustion chamber deposits on emissions of criteria pollutants. (Bitting *et al.*, 1994; Kalghatgi, 1997; Studzinski *et al.*, 1993).

Combustion chamber deposits also impact the efficiency (or fuel economy) of engines.

The thermal effects of deposits mentioned above tend to increase engine flame speed and thermal efficiency, leading to greater power output for a given fuel consumption. This also manifests itself as a decrease in carbon dioxide emissions per mile (Bitting *et al.*, 1994; Studzinski *et al.*, 1993). However, this efficiency increase is deceptive, since if combustion chamber deposits were eliminated, engines could be designed with higher compression ratios for given knock ratings and NO<sub>x</sub> emission levels, resulting in a considerable efficiency gain over engines designed to account for the effects of combustion chamber deposits.

## 2.5 Effects of Engine and Fuel Parameters on Deposit Formation Rates

While the effects of combustion chamber deposits on engine operation are beginning to be characterized, our current understanding of the processes that lead from fuel and oil components to the observed deposit material is very much less developed. Table 2.3 summarizes the known effects of different engine and fuel parameters on the rate of deposit growth, the equilibrium deposit thickness, and the chemical structure of the deposits.

Three of the parameters included in Table 2.3, namely the fuel-air ratio, fuel component volatility, and fuel component structure, merit further attention, as they provide insight into the physical and chemical mechanisms of deposit formation.

Parameter	Effect of Increase in Parameter on:			Suggested Mechanisms	Reference(s)
	Equilibrium deposit mass	Deposit formation rate	Deposit Structure		
Speed / Load	Decrease	Decrease	No effect	Increased $T_s$ Increased removal	Kalghatgi, 1995
Coolant Temperature	Decrease	Decrease	Increased polarity	Condensation is reduced for a given species volatility	Cheng, 1994
Inlet temperature	No effect	No effect	No effect	Conditions far from wall are unimportant	Cheng and Kim, 1990
Fuel-Air Equivalence Ratio	More deposits for leaner mix	Maximum rate at $\Phi \approx 0.85$	Unknown	Oxidation is needed for deposition	Cheng and Kim, 1990
Surface Material (thermal conductivity)	No effect for high thermal conductivities	No effect for high thermal conductivities	No effect for high thermal conductivities	Heat transfer outweighs surface effects	Cheng and Kim, 1990
Fuel Volatility (boiling point)	Decrease	Decrease	Unknown	Condensation rate is determined by species boiling point	Price <i>et al.</i> , 1995
Fuel Structure (degree of unsaturation)	No effect	Aromatics > Olefins > Alkanes	Unknown	Oxygen addition decreases species volatility	Price <i>et al.</i> , 1995
Detergent Additives	Uncertain	Uncertain	Additive present in deposits	Unknown	Jackson and Pocinki, 1994 Kalghatgi, 1997

**Table 2.3.** Effects of various engine and fuel properties on the equilibrium mass, formation rate and chemical structure of combustion chamber deposits, along with suggested mechanisms for the observed effects.

As observed by Cheng and Kim (1990), the rate of deposit formation has a maximum at a fuel-air equivalence ratio of  $\phi \approx 0.85$ , decreasing consistently for both leaner and richer mixtures. The fact that the deposition rate is maximized with a lean mixture can be interpreted to mean that the formation of deposits requires some degree of oxidation in the gas phase. The declining rate of deposition for equivalence ratios less than the maximum could be caused by more complete

burning of fuel or by increased removal rates. These effects are discussed in more detail in the following chapter.

Another major factor determining deposition rate is the combination of wall (or coolant) temperature and fuel component boiling point. Shore and Ockert (1958) were first to observe that combustion chamber deposit formation correlated strongly with fuel component boiling points, and for aromatics, boiling point was the only factor affecting deposition amount. The positive correlation of deposition rates with fuel component boiling points at constant wall temperature in chemically similar series, and negative correlation of deposition rates overall with wall temperature, point to the importance of condensation as a step in deposit formation, as will be discussed in detail in the following chapter (Cheng, 1994; Price *et al.*, 1995). Price *et al.* (1995, 1997) have correlated the deposit-forming tendency of different chemical series with the number of oxidizable bonds available, again suggesting an important role for oxidation in producing deposit precursors.

Competing with the deposit formation processes are both chemical and physical means of deposit removal. The deposit layers may be eroded by chemical processes such as oxidation and gasification, mechanical abrasion and flaking due to shear forces, and evaporation of volatile species contained within the deposit.

## 2.6 Current Theories of Combustion Chamber Deposit Formation

Despite the significant amount of data available on the characteristics of combustion chamber deposits, their effects on performance, and rates of formation in engines, few mechanisms for deposit formation have been suggested. Cheng (1994, 1996) has suggested condensation of very low volatility species, produced from the fuel via limited partial oxidation or pyrolysis, as the physical mechanism by which deposit material is transferred from the gas phase to the combustion chamber surfaces. This mechanism accounts for the strong effect of surface temperature on deposit amount, as the required volatility for deposition increases exponentially with surface temperature. Price *et al.* (1995, 1997) developed a correlation for deposit-forming tendency across chemical series, based on the assumption that partial oxidation

of fuel components was the mechanism by which the low-volatility depositing species are formed from the fuel. Neither mechanism attempts to postulate the exact identity of the depositing species, nor detailed chemical mechanisms leading from the fuel to deposits.

## 2.7 References

- A.A. Adamczyk and R.A. Kach, "The Effect of Engine Deposit Layers on Hydrocarbon Emissions from Closed Vessel Combustion," *Combustion Science and Technology*, Vol. 47, 193 ff. (1986).
- W.H. Bitting, G.P. Firmstone, and C.T. Keller, "Effects of Combustion Chamber Deposits on Tailpipe Emissions," *Society of Automotive Engineers* 940345 (1994).
- S.S. Cheng and C. Kim, "Effect of Engine Operating Parameters on Engine Combustion Chamber Deposits," *Society of Automotive Engineers* 902108 (1990).
- S.S. Cheng, "A Physical Mechanism for Deposit Formation in a Combustion Chamber," *Society of Automotive Engineers* 941892 (1994).
- S.S. Cheng, "A Micrographic Study of Deposit Formation Processes in a Combustion Chamber," *Society of Automotive Engineers* 962008 (1996).
- L.B. Ebert, W.H. Davis, Jr., D.R. Mills and J.D. Dennerlein, "The Chemistry of Internal Combustion Engine Deposits," in L.B. Ebert, ed., Chemistry of Engine Combustion Chamber Deposits, Plenum Press, 71-144 (1985).
- L.A. Gebhard, R.S. Lunt and B.G. Silbernagel, "Electron Spin Resonance Studies of Internal Combustion Engine Deposits," in L.B. Ebert, ed., Chemistry of Engine Combustion Chamber Deposits, Plenum Press, 145-198 (1985).
- R.F. Harder and C.L. Anderson, "Investigation of Combustion Chamber Deposit Thermal Behavior Using Optical Radiation Measurements in a Fired Engine," *Combustion Science and Technology*, Vol. 60 p.423 (1988).
- M.O. Harpster, Jr., S.E. Matas, J.H. Fry, and T.A. Litzinger, "An Experimental Study of Fuel Composition and Combustion Chamber Deposit Effects on Emissions from a Spark Ignition Engine," *Society of Automotive Engineers* 950740 (1995).
- A.B. Hopwood, S.Chynoweth and G.T. Kalghatgi, "A Technique to Measure Thermal Diffusivity and Thickness of Combustion Chamber Deposits in-Situ," *Society of Automotive Engineers* 982590 (1998).

- M.M. Jackson and S.B. Pocinki, "Effects of Fuel and Additives on Combustion Chamber Deposits," *Society of Automotive Engineers* 941890 (1994).
- G.T. Kalghatgi, "Deposits in Gasoline Engines - A Literature Review," *Society of Automotive Engineers* 902105 (1990).
- G.T. Kalghatgi, "Combustion Chamber Deposits in Spark-Ignition Engines: A Literature Review," *Society of Automotive Engineers* 952443 (1995).
- G.T. Kalghatgi, "Combustion Chamber Deposits and Knock in a Spark-Ignition Engine - Some Additive and Fuel Effects," *Society of Automotive Engineers* 962009 (1996).
- G.T. Kalghatgi, "Effects of Combustion Chamber Deposits, Compression Ratio and Combustion Chamber Design on Power and Emissions in Spark-Ignition Engines," *Society of Automotive Engineers* 972886 (1997).
- Y. Nakamura, Y. Yonekawa and N. Okamoto, "The Effect of Combustion Chamber Deposits on Octane Requirement Increase and Fuel Economy," in L.B. Ebert, ed., Chemistry of Engine Combustion Chamber Deposits, Plenum Press, 199 - 212 (1985).
- M. Nagao, T. Kaneko, T. Omata, S. Iwamoto, H. Ohimori and S. Matsuno, "Mechanism of Combustion Chamber Deposit Interference and Effects of Gasoline Additives on CCD Formation," *Society of Automotive Engineers* 950741 (1995).
- J.W. Orelup and O.I. Lee, "Factors Influencing Carbon Formation in Automobile Engines," *Industrial and Engineering Chemistry*, Vol. 17, 731 (1925).
- R.J. Price, J.P.T. Wilkinson, D.A.J. Jones, and C. Morley, "A Laboratory Simulation and Mechanism for the Fuel Dependence of SI Combustion Chamber Deposit Formation," *Society of Automotive Engineers* 952445 (1995).
- R.J. Price, C.D. Spink, and C. Morley, "Prediction of Combustion Chamber Deposit Growth in SI Engines," *Society of Automotive Engineers* 972835 (1997).
- L.B. Shore and K.F. Ockert, "Combustion Chamber Deposits - A Radiotracer Study," *SAE Transactions*, Vol. 66, 285-294 (1958).
- W.M. Studzinsky, P.M. Liiva, P.J. Choate, W.P. Acker, T.Litzinger, S.Bower, M. Smooke and K. Brezinsky, "A Computational and Experimental Study of Combustion Chamber Deposit Effects on NO<sub>x</sub> Emissions," *Society of Automotive Engineers* 932815 (1993).





### 3.1 Mechanistic Inferences from Literature Data

While not providing a method for eliminating combustion chamber deposits, the body of research summarized in the previous chapter has provided a number of insights that identify some of the major contributing factors to deposit formation and begin to outline the interactions between them. Considering the experimental evidence that is available in the literature as a whole, we may build up a basic physical model of the fundamental processes that lead to formation of combustion chamber deposits.

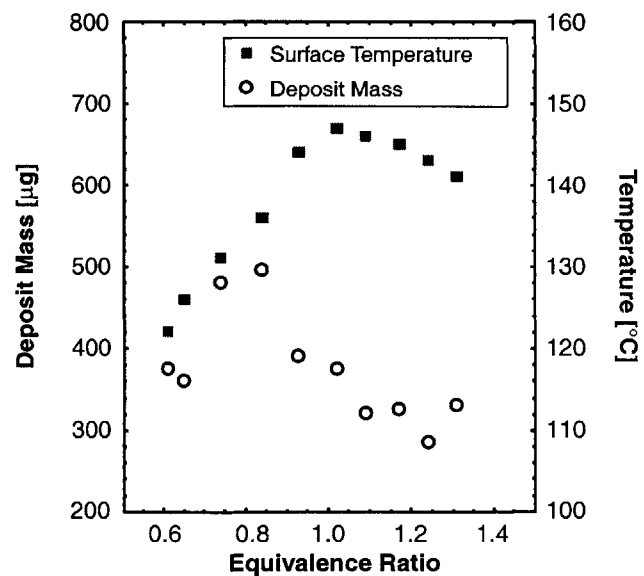
A number of inferences about the nature of the deposit formation process can be drawn from the varying types of investigations that have been performed to date. In the following discussion, we consider a spark-ignition gasoline engine that is operating at idealized conditions, *i.e.* without excessive oil consumption and with no liquid fuel layers on the combustion chamber walls. Firstly, it is likely that deposits in an engine operating under these “normal” conditions are formed largely from the fuel, rather than from lubricating oil layers. The elemental composition of the deposits shows very small amounts of oil-derived metals (Ebert *et al.*, 1985), and if an engine is run on propane fuel, deposits do not form and existing deposits may be removed, regardless of the essentially unchanged oil layer behavior (Siegl and Zinbo, 1985). It also can be concluded that the molecules that transfer from the gas phase to the deposit layer correspond to fuel-derived species, rather than species that are present in the fuel itself. This is supported by the observed dependence of deposition rate and amount on the degree of unsaturation (Price *et al.*, 1995), as well as by the direct observation of micro-droplet formation on wall surfaces where the temperature is significantly higher than the range of boiling points of fuel components (Cheng, 1996). In the following discussion, these fuel-derived species will be referred to as deposit precursor species.

The observed exponential trends in deposition rate with fuel component boiling points and with wall temperature for a given fuel suggest an important role for condensation and evaporation processes in the transfer of species from the gas phase to the deposit layer, since the

volatility of a condensed species, and hence its ability to remain on the wall or deposit layer surface, decreases exponentially as surface temperature increases. Condensation as a deposit forming mechanism also helps to explain the observed layered structure of deposits, with strata of decreasing volatility ranging from the wall surface to the top surface of the deposit (Gebhard *et al.*, 1985). Since the deposit acts as an insulator, the temperature of the surface in contact with the gas phase will increase as the deposit grows thicker. If species are being added to the deposit by condensation, lower and lower species volatilities will be required for deposition as the thickness increases, producing a structure like the one observed.

Another feature of the deposit formation mechanism is the role of oxygen. One of the major pieces of evidence that points to the importance of oxygen in the deposit formation process is the elemental composition of the deposits. A significant fraction of the deposit (16 to 25 percent by weight) consists of oxygen (Ebert *et al.*, 1995); this oxygen could be added in the gas phase through partial oxidation of the fuel molecules before deposition occurs, or alternatively through heterogeneous reactions between the gases near the wall and the existing deposit layer.

Some insights into the relative importance of these two potential oxygen addition mechanisms can be gained by considering the effects of fuel-air equivalence ratio on deposit formation rate. Figure 3.1 shows data from a study by Cheng and Kim of deposit formation over two-hour tests in an engine running at various equivalence ratios, along with the measured wall temperature at each condition (Cheng and Kim, 1990). Two major factors contribute to the observed shape of the deposition rate curve. The first is the effect of wall temperature; as discussed above, higher wall temperatures should



**Figure 3.1** Deposit mass and measured wall temperatures for two-hour engine tests at varying fuel-air equivalence ratios. (Cheng and Kim, 1990)

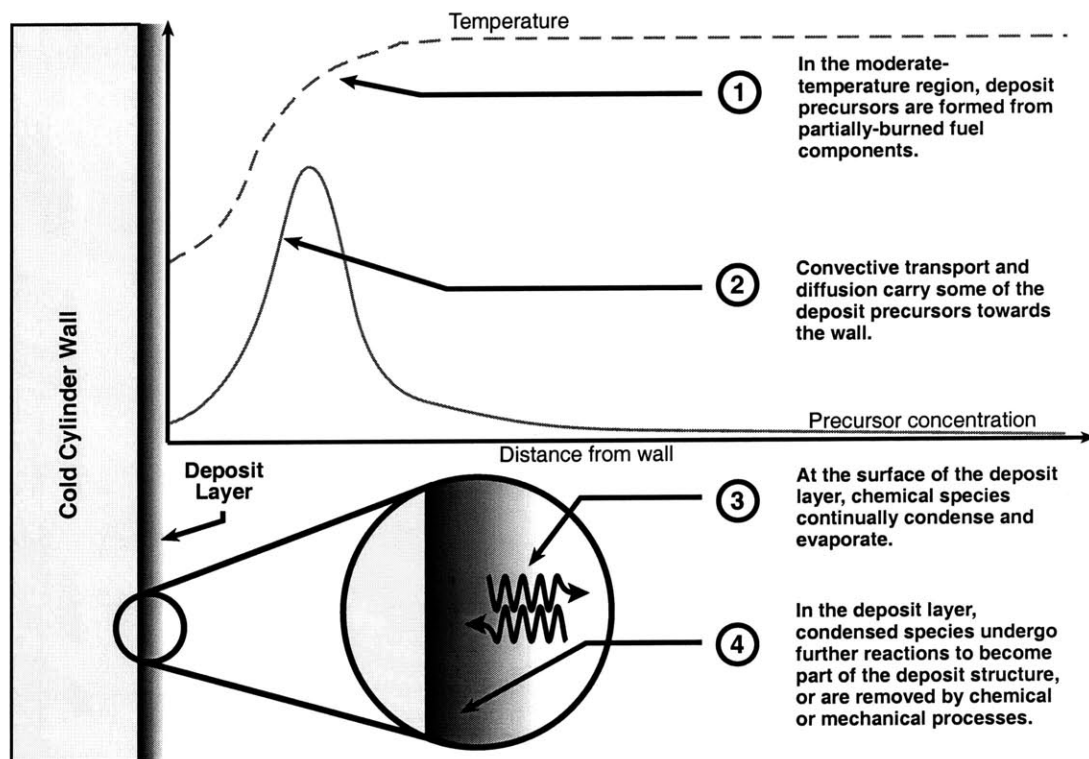
decrease deposition, and vice versa. The second effect is the gas-phase interactions that form the precursor species and transport them to the wall surface. The plot may be divided into three regions to illustrate the competitions between these effects. The region between  $\phi = 0.8$  and  $\phi = 1.0$  exhibits an inverse relationship between deposition rate and temperature, such as that observed at fixed stoichiometry. Outside of this range, at both richer and leaner equivalence ratios, the deposition decreases even though wall surface temperature is decreasing as well. If deposit precursors are being formed through fuel-air gas-phase reactions, this drop-off could be explained by slow formation rates due to insufficient concentrations of reactants (low fuel concentration on the lean side, and low oxygen concentration on the rich side). However, the fact that the peak deposition occurs at a lean equivalence ratio ( $\phi \approx 0.85$ ) suggests that excess oxygen concentrations promote the formation reactions for deposit precursors, which would be consistent with a partial oxidation process for precursor formation. However, heterogeneous reactions between gas-phase oxygen and species condensed in the deposit layer could show a similar trend.

Additional support for gas-phase oxygen addition is found in the correlation formulated by Price *et al.* relating fuel structure and deposition rate in a pulsed flame deposition experiment (Price *et al.*, 1995). The deposition rates produced by fuel species of different chemical families (alkanes, alkenes, aromatics) were found to correlate with “effective boiling points” derived by assuming that oxygen addition to unsaturated carbon-carbon bonds occurred before condensation at the wall surface.

Another aspect of deposition mechanisms that may be derived from previous work is that further chemical and physical interactions occur within the deposit layer to form a final deposit structure from the initial condensed species. The trend towards forming highly polymerized, polyaromatic structures has been observed in micrographic studies of early stages of deposit formation, as well by chemical analysis of deposits after varying engine run times (Cheng, 1996; Kalghatgi, 1995). It is also important to remember that both chemical and physical removal mechanisms (oxidation, evaporation, physical flaking) will be occurring constantly in competition with the deposit formation process.

### 3.2 Deposit Formation Mechanism Hypothesis

Given the above inferences from the literature in the field, a basic model of the formation process of combustion chamber deposits may be formulated. The suggested mechanism is as follows (see Figure 3.2): As the flame front nears the engine wall late in the cycle, it begins to lose heat to the cold surface, slowing the reaction rates and preventing the flame from travelling all the way to the wall. As a result, some of the fuel/air mixture in the flame quenching region does not experience temperatures high enough for complete oxidation to occur. The resulting incomplete combustion reactions can lead to the production of low volatility, partially oxidized hydrocarbons; these species have the potential to condense at the wall, and can be considered to be gas-phase deposit precursor species. As illustrated in Figure 3.2, the zone where deposit precursors are formed is not immediately adjacent to the wall surface, but a short distance away, where temperatures are high enough for some reaction to occur. Diffusive and convective fluxes carry the precursors away from the region where they are formed, both into the core gases, where they are likely to be oxidized to equilibrium combustion products, and also towards the wall,



**Figure 3.2** Hypothesized mechanism for combustion chamber deposit formation.

where they have a chance to condense.

If a sufficient amount of a given deposit precursor is formed by partial oxidation reactions and transported to the wall surface, the partial pressure of that species at the wall may exceed its vapor pressure at the wall temperature, thus permitting condensation to take place. Conversely, if a species is condensed on the wall or deposit layer and is not chemically bonded to the rest of the deposit, it may evaporate if its partial pressure in the gas phase is below the vapor pressure. This model presumes that the deposit phase behaves similarly to a liquid; this is supported, at least in the early stages of deposition, by observations of deposit structures that consist of nearly-spherical droplets on the order of 10  $\mu\text{m}$  in diameter, indicating a strong effect of surface tension (Cheng, 1996). Those species that can remain condensed on the wall through multiple engine cycles and flame quench events can eventually undergo further reactions to become part of the polymerized deposit structure. As the deposit continues to grow in this fashion, it acts as an insulating layer and raises the surface temperature seen by the gas phase molecules until the rate of condensation becomes too low to produce deposit growth that exceeds the rate of deposit removal. Note that other processes may contribute to deposition at the wall, such as adsorption and heterogeneous reaction. While these effects are not included in this model, based on the experimental evidence strongly suggesting condensation as a major deposition mechanism, there is no corresponding evidence to suggest that adsorption or reaction do not contribute to deposition.

This model asserts that combustion chamber deposit formation is dependent upon four processes: the formation of deposit precursors from fuel components and oxygen in the flame quench region, gas phase transport of these precursors, condensation and evaporation of the deposit precursors at the wall or deposit layer surface, and polymerization reactions within the deposit structure. The dynamic balances between these processes, along with the constant occurrence of deposit removal via chemical and physical mechanisms, will determine the rate and amount of deposition from a given fuel under a specified set of engine operating conditions.

### 3.3 Non-Dimensional Model and Characteristic Parameters

The formation and removal of combustion chamber deposits in a realistic system involves tens to hundreds of chemical species interacting in the flame quench layer near the wall of the engine under highly turbulent and rapidly changing flow conditions. Nevertheless, characteristic parameters derived from a much simpler system may still be useful to describe and understand the full process. This type of analysis can also help to clarify the relationships described in the previous section between the different physical processes that contribute to deposit formation, and give insight into which processes may dominate under different conditions.

If we consider a single reacting and diffusing species (e.g. a high molecular weight deposit precursor produced by partial oxidation of unburned fuel) in the quench layer near a cold engine wall where condensation and evaporation may take place, its behavior can be described approximately by the following equation (assuming negligible convective transport):

$$\frac{\partial P_i}{\partial t} = D_i \frac{\partial^2 P_i}{\partial x^2} - k_{r,i}(x,t)P_i + k_{f,i}(x,t) \quad (3.1)$$

where  $P_i$  is the partial pressure of species  $i$ ,  $D_i$  is the diffusion coefficient of species  $i$  into the surrounding mixture (here assumed to be independent of position),  $k_{f,i}$  and  $k_{r,i}$  are rate constants for formation and removal of the species, respectively, which could depend on both position and time, and  $x$  is the spatial coordinate perpendicular to the wall surface (the system is assumed to be one-dimensional). Reasonable boundary conditions for this equation are that all gradients go to zero at large distances from the wall (*i.e.* in the core burned gases), along with the following condensation / evaporation flux boundary condition at the wall, using the Clasius-Clapeyron relation for the species vapor pressure at temperature  $T$ :

$$D_i \frac{\partial P_i}{\partial x} \Big|_{x=0} = k_c (P_{v,i}(T) - P_i|_{x=0}) = k_c \left( P_{v,i}(T_o) e^{\frac{-\Delta H_v}{R} \left( \frac{1}{T} - \frac{1}{T_o} \right)} - P_i|_{x=0} \right) \quad (3.2)$$

where  $k_c$  is a rate constant for condensation (and evaporation),  $P_{v,i}(T_o)$  is the vapor pressure of species  $i$  at temperature  $T_o$ ,  $\Delta H_v/R$  is the heat of vaporization of the species in Kelvin (also at  $T_o$ ), and  $T$  is the temperature at the wall. A more thorough discussion of this boundary condition is

given in Chapter 4. Additional equations would be necessary to include reactions within the deposit layer and removal mechanisms other than evaporation, but these processes will not be included in this simple model.

Non-dimensionalization of the above equations, using the quench layer width  $L$  as a characteristic length, and the diffusion time across the quench layer,  $L^2/D_i$ , as a characteristic time, leads to the following equations in the dimensionless length  $\zeta$ , time  $\tau$ , and species concentration  $\theta$ :

$$\frac{\partial \theta}{\partial \tau} = \frac{\partial^2 \theta}{\partial \zeta^2} - Da_r \theta + Da_f \quad (3.3)$$

$$\left. \frac{\partial \theta}{\partial \zeta} \right|_{\zeta=0} = Bi \left( e^{\frac{-\Delta H_c}{R} \left( \frac{1}{T} - \frac{1}{T_o} \right)} - \theta \right)_{\zeta=0} \quad (3.4)$$

There are two important types of dimensionless numbers in the above equations: the Damkohler numbers,  $Da_r = k_{r,i}L^2/D_i$  and  $Da_f = k_{f,i}L^2/D_i$  are the ratios of the reaction rates to the diffusion rate, and the Biot number,  $Bi = k_cL/D_i$ , is the ratio of mass transfer by condensation and evaporation to mass transfer by diffusion at the wall. The magnitudes of these two numbers will determine the dominant process for deposit formation; for example, if  $Da_f$ ,  $Da_r$ , and  $Bi$  are much greater than one (i.e., diffusion is slower than reaction in the quench layer and condensation/evaporation is faster than diffusion at the wall), the deposit formation rate will be determined by the time it takes for the species to diffuse to the wall, while if  $Bi$  is small, deposit formation will be limited by the rate of condensation at the wall.

Knowing *a priori* that one of these characteristic numbers is large or small would allow simplified analysis of deposit formation, by indicating that one or more of the processes involved has a negligible effect. Using typical values for hydrocarbon fuels in an engine quench layer of  $L = 1$  mm,  $D_i = 1 - 2$  cm<sup>2</sup>/s, and  $k_i = 10 - 1000$  s<sup>-1</sup> (representative of partial oxidation rates), we can determine a likely range for the Damkohler number of  $0.05 < Da < 10$ , which indicates that the reaction and diffusion processes are closely balanced under engine conditions. The Biot number is more difficult to estimate, as the rate  $k_c$  is largely an empirical factor; the discussion in the following chapter will describe the effects of large and small values of  $Bi$ .

Based on this analysis, any of these three processes (reaction, diffusion/transport, or condensation and evaporation) could be rate determining under normal engine operating conditions. Although the equations needed to describe the multispecies case are much more complex, similar dimensionless numbers can be calculated for each species, and determining values of these numbers for real deposit precursors with varying engine conditions will allow identification of the important regimes for combustion chamber deposit formation.

### 3.4 Open Questions in Combustion Chamber Deposit Formation

The analysis above gives a reasonable picture for the formation mechanism of combustion chamber deposits, and serves to identify some of the competing processes that are involved in determining the rate of deposit formation. However, the majority of the mechanism described here is derived from indirect inferences from the available data, and a number of important issues have yet to be directly investigated.

The first question that should be raised about the mechanism depicted in Figure 3.2 is this: what is the chemical identity of the postulated “deposit precursors”? Price *et al.* (1995) assumed very highly oxygenated species with roughly the same number of carbons as the fuel species from which they were derived, and here we have suggested that the precursors are products of partial oxidation. However, actual direct identification of the species present in the flame quench zone could provide very useful insights into the formation mechanisms of the precursors, not to mention confirming their existence. Some basic questions about the structure of the precursors include the degree of oxidation (if any) they undergo in the gas phase, and whether they exhibit significant growth in molecular weight from the initial fuel components or are instead formed from smaller fragments of the fuel species. Having the precise identities of deposit precursor species could also allow the calculation or more accurate estimation of their formation and transport rates in the quench layer, which are key to the rate of deposition.

A related question is when oxygen is added to the deposit structure. Above, we have postulated that at least some fraction of the oxygen contained in the final deposit is delivered through oxygenated precursors that are formed in the gas phase. However, there is no direct



evidence for this from existing data, and it is certainly possible that oxygen addition occurs through heterogeneous reactions between the deposit layer and the hot combustion gases in contact with it.

Another assumption made in the model is that condensation is a major mechanism for delivering the precursors to the deposit layer. To support this assumption, we need to determine if, for real precursor species in an engine, condensation is sufficient to describe the deposition rates that are observed, or whether adsorption processes are required to provide the measured deposition rates.

A very important question from the viewpoint of controlling deposit formation is the following: which of the four processes noted in Figure 3.2 (reaction, diffusive and convective transport, condensation and evaporation, and reactions within the deposit layer) will be rate-limiting under specified engine operating conditions? As shown with the one-dimensional, single species model above, it is very difficult to make definitive statements about this balance from simple analyses; detailed study of the gas-phase processes is needed to clarify this area.

### 3.5 Objectives of this Study

The current work has been designed to bring more insight to these questions, from as fundamental a standpoint as is practically achievable. The main objectives are as follows:

- **Directly identify likely deposit precursor species in a flame - wall environment**

The preheat zone of a premixed flat flame, between the burner surface and the high temperature reaction zone, is used to create a chemical and thermal environment similar to those found in a flame quenching process. This model system provides the opportunity to make direct measurements of species concentrations and chemical structures, allowing identification of potential deposit precursors. The identities and observed concentration profiles of these precursors can help to create a more accurate picture of the gas-phase chemical processes that contribute to engine deposition.

- **Model the engine deposition process from a fundamental standpoint**

All the processes described in Figure 3.2 can be modeled and numerically simulated from a basic mechanistic standpoint. The key missing component is the identities and chemical formation mechanisms of the deposit precursors, which may be provided by the direct measurements taken as part of the first objective.

- **Clarify the interactions between chemical and physical processes that contribute to combustion chamber deposit formation**

The combination of the results produced from the first two objectives will provide a unique opportunity to compare the contributions of the many processes that are involved in combustion chamber deposit formation, under a range of conditions.

Almost all of the studies mentioned above have been "top-down" approaches to the problem, deducing the characteristics of deposit formation and removal mechanisms from engine data and observations of developed deposits; the objectives of this work represent a "bottom-up" viewpoint, beginning from the study of the basic mechanisms of deposit formation, and attempting to use the information gained to explain the macroscopic trends observed in engine tests.

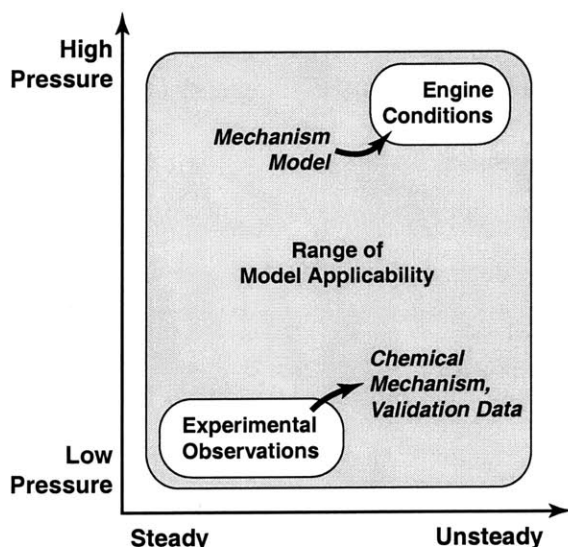
### **3.6 Joint Numerical – Experimental Methodology**

The objectives described above present significant technical challenges. The engine quench layer thickness is very small under normal conditions (on the order of 1 millimeter) and the flame quench event itself occurs on a timescale of just a few milliseconds. Due to these constraints, it is not possible to make the detailed chemical species concentration measurements that are needed for the identification of deposit precursors in an operating engine. It is also extremely difficult to draw useful mechanistic conclusions from experiments using gasoline as a fuel; even well-specified reference gasolines such as indolene contain hundreds of different hydrocarbon species, making chemical analysis of flame samples quite difficult. To produce interpretable results, we are limited to low-pressure, steady state burner flames, which have

expanded preheat zones and allow sufficient time for careful gas sampling, and to fuels with only a few components.

As a result of these experimental difficulties, this study has been formulated as a joint numerical-experimental approach, in order to allow experiments to be done under appropriate, interpretable conditions, and yet retain relevance to the engine conditions which are the main concern of this project. Detailed measurements of chemical species profiles are made via direct probe sampling from a low-pressure flat flame burner, with a temperature-controlled burner surface to control the flame heat loss to the surface and provide a site for deposition. In conjunction with the experiments, a numerical model has been constructed to simulate the flame quenching and deposition process, which can be applied both to the experimental system and to engine conditions, using detailed transport and chemistry.

A schematic diagram of the method is shown in Figure 3.3. The axes in the diagram represent the range of physical conditions that is spanned by this work; the x axis represents the time dynamics of the flame propagation and quenching, from steady state to rapid transients, and the y axis extends over a range of pressures from less than 100 millibar to over 10 atmospheres.



**Figure 3.3** Schematic diagram of study methodology, using a detailed chemistry numerical simulation to connect experimentally observed chemical mechanisms with deposition at engine operating conditions.

The engine system that we wish to describe falls in the upper right corner of the plot (high pressure and unsteady dynamics), while the accessible experimental conditions lie on the lower left (low pressure, steady state). In order to connect the two, the numerical model must be applicable to the entire range of conditions.

The main input to the model from the experimental data is the identity of deposit precursor species, along with potential chemical mechanisms for their formation from fuel components and air.

The species profiles and fluxes measured in the experimental apparatus, along with appropriate chemical mechanisms, may also be used to validate the model's performance in simulating flame dynamics at the experimental conditions. The mechanisms and precursor species identified in the experimental system may then be used in the numerical model at engine conditions to determine what affect they would have on deposition rates in a realistic system.

Both the experiments and the simulation will be based on propane fuel doped with small amounts (up to ten percent by carbon) of a heavy hydrocarbon that is likely to cause deposit formation. As propane is known not to cause deposition, it can act essentially as a "blank" fuel, while still providing realistic flame temperatures, heat fluxes and reaction rates. Using a small amount of dopant fuel, rather than a pure heavy hydrocarbon fuel, allows us to control the dopant fraction independently of the flame stoichiometry and gas flow velocities. It also provides a more accurate simulation of gasoline, in which the heavy species that are likely to contribute most strongly to deposition represent only a small fraction of the fuel. Toluene will be used as the dopant in all experiments done for this thesis; it was chosen both because it is known to be a strong contributor to deposition (Cheng, 1996), and because its single-ring structure makes it and its derivatives easy to separate from other hydrocarbons produced in the burner preheat zone from the propane fuel, thus simplifying the task of mechanistic interpretation.

A few important points should be noted about the benefits and difficulties inherent in this method. Firstly, the experimental component of the project is *not* intended to model engine deposition conditions; it is only intended as a means to identify likely deposit precursor species and chemical mechanisms for their formation from the dopant, which may then be used along with the numerical simulation to explore their effects at engine conditions. Thus, some significant differences between the experimental and engine systems can be tolerated, as long as they can be modeled accurately in the numerical simulation. There are two major physical differences to consider in this regard. The first is the gas flow through the burner surface, which represents the "wall" of the combustion chamber. This convective flow can be modeled quite well in the simulation, so its effects on the transport of deposit precursors should be interpretable. The differences in pressure, however, are not as straightforward to address. The rates and even overall

mechanistic pathways of combustion can be highly dependent upon pressure, and thus using rates and chemical reaction paths determined from low-pressure experimental data to model high-pressure systems can be quite difficult. The scope of this particular work does not extend to determining detailed elementary reaction mechanisms and rates from the experimental data, but the potentially significant effects of pressure differences should be kept in mind for any extrapolations to engine conditions.

We should also note that this study does not address in detail one important aspect of combustion chamber deposits; namely the deposit removal processes that will occur constantly in an engine environment. Since the experimental conditions are optimized for study of the gas-phase processes of deposit precursor formation and transport, the intrinsically heterogeneous interactions that will lead to deposit removal are not easily observed in the data. In the analysis to follow in the rest of the thesis, it will be noted where this omission could lead to significant error.

### **3.7 Intended Contributions to Combustion Chamber Deposit Research**

This work takes a fundamental approach to understanding the problem of combustion chamber deposits, something that has been done rarely in the past. The study focuses on the gas-phase processes and that are key to deposit formation, while most previous work has been concerned exclusively with the wall interactions and input fuel composition. Despite the basic nature of the study, we still hope to make useful contributions to the practical problem of combustion chamber deposits. Direct identification of deposit precursors, determination of rate-limiting processes for deposit formation as functions of engine and fuel properties, and quantification of the relationship between the known trends of deposition with engine wall temperatures and fuel component boiling points are all results that will be generally applicable to the understanding of deposition phenomena in combustion engines. However, perhaps one of the most important contributions of this project may be the evaluation of the utility of the project methodology itself. Combustion chamber deposit formation has long been considered a “difficult” problem in the automotive and fuels industries, largely because of the many competing processes that are involved and the difficulty of making measurements to elucidate the chemical

mechanisms of partial combustion of complex fuels in engine quench layers. If useful results may indeed be obtained from the laboratory study of individual fuel components in controlled flame experiments along with supporting numerical modeling, then this new avenue of approach to the deposit problem could lead to significant increases in understanding, and will indicate a number of clear paths to future research.

### 3.8 References

- S.S. Cheng and C. Kim, "Effect of Engine Operating Parameters on Engine Combustion Chamber Deposits," *Society of Automotive Engineers* 902108 (1990).
- S.S. Cheng, "A Micrographic Study of Deposit Formation Processes in a Combustion Chamber," *Society of Automotive Engineers* 962008 (1996).
- L.B. Ebert, W.H. Davis, Jr., D.R. Mills and J.D. Dennerlein, "The Chemistry of Internal Combustion Engine Deposits," in L.B. Ebert, ed., Chemistry of Engine Combustion Chamber Deposits, Plenum Press, 71 - 144 (1985).
- L.A. Gebhard, R.S. Lunt and B.G. Silbernagel, "Electron Spin Resonance Studies of Internal Combustion Engine Deposits," in L.B. Ebert, ed., Chemistry of Engine Combustion Chamber Deposits, Plenum Press, 145-198 (1985).
- G.T. Kalghatgi, "Combustion Chamber Deposits in Spark-Ignition Engines: A Literature Review," *Society of Automotive Engineers* 952443 (1995).
- R.J. Price, J.P.T. Wilkinson, D.A.J. Jones, and C. Morley, "A Laboratory Simulation and Mechanism for the Fuel Dependence of SI Combustion Chamber Deposit Formation," *Society of Automotive Engineers* 952445 (1995).
- W.O. Siegel and M. Zinbo, "On the Chemical Composition and Origin of Engine Deposits," in L.B. Ebert, ed., Chemistry of Engine Combustion Chamber Deposits, Plenum Press, 53 - 70 (1985).

#### 4.1 Numerical Analysis Goals

One of the central aims of this work is to examine the chemistry that leads to combustion chamber deposits in a detailed manner, while simultaneously ensuring that the research remains applicable to engine-relevant conditions. Since it is not possible to make sufficiently detailed measurements of chemical species concentrations in the flame quench layers found in an engine, the numerical model described in this chapter is used to provide a link between the available experimental conditions and the engine system.

The task of providing this connection between the experimental and engine regimes places a strict set of requirements on the numerical simulation. As described in the previous chapter, the model must be able to cover a wide range of physical conditions, extending from steady-state processes to rapid transients, and from low to high pressures. In order to provide insights into deposit formation, the model needs to include the competing processes of diffusive and convective transport, species production and consumption by chemical reactions, and boundary interactions such as deposition fluxes. To model the flat-flame burner experimental system as well as engine cycles, it is also necessary to allow for bulk gas flow through the boundaries. Since identification of the chemical composition and formation rates of potential deposit precursors is among the primary objectives of this study, the reaction chemistry should be modeled as accurately as possible; this involves integrating systems of up to hundreds of elementary reactions, with fifty to a hundred separate chemical species.

The simulation code must be capable of calculating all of the above processes through a complete flame propagation and quenching event, which requires resolving sharp gradients in the temperature and species concentrations which may travel over the entire computational domain. Given these requirements for accurately representing the physical system, the model must also satisfy the practical consideration that the computing time for a single simulation should be relatively small, so that a large number of different operating conditions can be explored.

Existing chemistry and transport modeling codes (Kee *et al.*, 1985; Westbrook and Pitz, 1995) were found to be insufficient to meet these goals, being limited either in the ability to model transient dynamics or in the detail of chemistry and transport models. A new computational tool, described in this chapter, was developed to meet all of these requirements simultaneously.

## 4.2 One-Dimensional Approximation

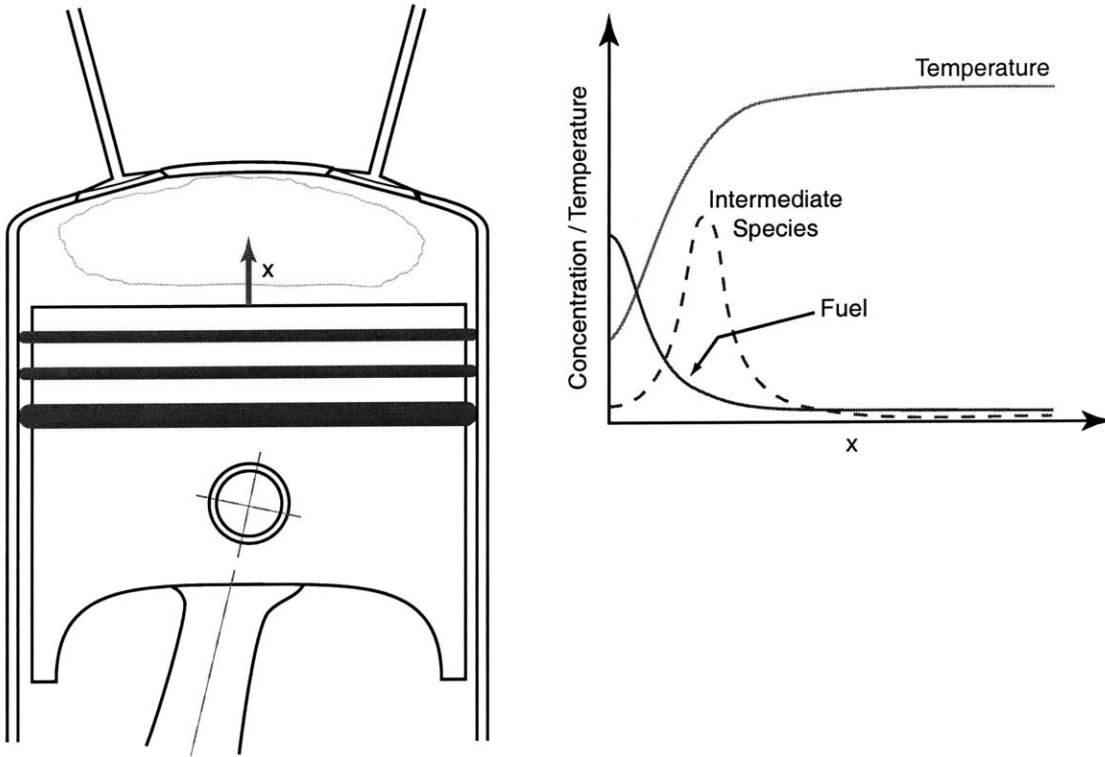
Numerical solution of systems of partial differential equations of the type that result from multidimensional reacting flow problems reduces to the process of inverting a large, sparse Jacobian matrix hundreds or thousands of times. The number of operations required for a single matrix inversion is roughly proportional to the number of filled elements in the matrix, which will in turn be proportional to the number of gridpoints in the spatial domain and to the square of the number of chemical species. For a fully three-dimensional problem (i.e. equal grid resolution required in every spatial dimension), this results in the relationship given in equation 4.1 for the computational time  $t_c$ , with  $p$  representing the number of gridpoints for each dimension,  $c$  the number of spatial dimensions in the problem, and  $N$  the number of species included.

$$t_c \propto p^c N^2 \quad (4.1)$$

Given the stiff nature of the differential equations produced by reacting flow problems, the proportionality constant for the above equation (i.e. the number of matrix inversions that must be performed for a given simulation) is likely to be quite large. For a three-dimensional system with 100 species and 100 gridpoints per dimension, equation 4.1 predicts a minimum of  $10^{10}$  operations per matrix inversion. In practice, this is well beyond the useful range of modern computers. Hence, the complexity of the system must be reduced in some way in order to make the computational problem tractable.

Since the physical event of flame quenching in the engine occurs in a very thin region near the head surfaces and piston top, while the flame front itself has a relatively large surface area perpendicular to its direction of propagation, it is reasonable to approximate the process as a one-dimensional system (note that this requires the assumption that cross convection effects are





**Figure 4.1.** Schematic representation of the one-dimensional modeling domain. The surface at the left boundary could represent the piston top or any of the other head surfaces where combustion deposits form, particularly in the end-gas region. The right boundary should extend sufficiently far past the flame front to ensure negligible gradients in temperature and species concentrations.

unimportant). When the flame front approaches closely enough to a surface to begin quenching (about one to two millimeters under engine conditions), the thermal and concentration gradients in the direction normal to the surface are extremely steep, and may be assumed to be significantly larger than any gradients in other directions. Thus, we choose as our computational domain a one-dimensional region with one boundary at the engine wall surface or piston top and the other in the core burned gases, significantly behind the flame front. This region generally corresponds to between one and five centimeters of physical distance. A schematic diagram of this domain is shown in Figure 4.1.

The use of a one-dimensional modeling domain reduces the complexity of the computational task considerably, without sacrificing detail in the modeling of the chemical reaction system. It also makes possible the use of adaptive spatial mesh redistribution, discussed later in this chapter, which further increases the effective spatial resolution of the numerical simulation while minimizing the number of gridpoints required. It is a particularly useful

approximation for this problem, not only because of its basis in the physical process being modeled, but also because it allows detail to be focused in the chemistry and boundary interactions, which are the key elements to be examined for this study.

### 4.3 Model Definitions and Assumptions

The model system thus consists of a one-dimensional domain, characterized by the mass fractions of all chemical species, temperature, and pressure at each point. Given an initial condition, the time evolution of species mass fractions and temperature is governed by chemical production and consumption rates, diffusion, and convective transport. Points on the boundary of the domain may also be affected by boundary fluxes of heat or species.

The Mach number of flows in the engine cylinder is low, so pressure is constant over the domain, and is imposed as an external parameter that is a function of time only. The Reynolds numbers of the flows involved in quenching flames, with temperature varying from 300 to 1800K, characteristic velocities similar to the flame speeds of 30 to 100 cm/s, and length scales on the order of millimeters, are on the order of 500 and below. Thus, we assume laminar transport during the flame quench process.

The chemical reactions that take place in the gas phase are modeled via the law of mass action, with rate constants  $k$  determined as functions of temperature  $T$  by Arrhenius equations of the form

$$k = AT^b e^{-E_a/RT} \quad (4.2)$$

where  $E_a$  is the reaction activation energy,  $R$  is the universal gas constant, and  $A$  and  $b$  are constant coefficients. Reaction mechanisms and rates are provided using CHEMKIN-II format mechanism files (Kee *et al.*, 1989).

Thermodynamic properties of the chemical species included in the model are calculated via polynomial fits in the NASA polynomial format, with coefficients from the CHEMKIN thermodynamic database, unless otherwise noted (Burcat, 1984; Kee *et al.*, 1990). Likewise, diffusion coefficients and thermal conductivities are calculated using the CHEMKIN format (Kee *et al.*, 1983). Popp *et al.* have shown Soret thermal diffusion to be less than 2 percent of the total

diffusion flux under flame quenching conditions for wall temperatures under 500 Kelvin, and the Dufour effect to be negligible at any wall temperature; both of these effects have been neglected in the current formulation (Popp *et al.*, 1996).

#### 4.4 Governing Equations and Model Formulation

Equations 4.3 through 4.6 describe the conservation and constitutive laws that govern the system. Profiles of  $N$  chemical species concentrations and temperature are defined in a Cartesian basis with  $x$  as the spatial coordinate. Conservation of mass, species, and energy determine the time rates of change of the species concentrations and temperature, while the ideal gas equation of state relates the temperature, pressure and density.

**Mass conservation:**

$$\frac{\partial \rho}{\partial t} + \frac{\partial}{\partial x}(\rho u) = 0 \quad (4.3)$$

**Species conservation:**

$$\rho \frac{\partial Y_i}{\partial t} = -\rho u \frac{\partial Y_i}{\partial x} + \frac{\partial}{\partial x} \left( \rho D_i \frac{\partial Y_i}{\partial x} \right) + \dot{w}_i \quad i = 1..N \quad (4.4)$$

**Energy conservation:**

$$\rho C_p \frac{\partial T}{\partial t} = -\rho C_p u \frac{\partial T}{\partial x} + \frac{\partial}{\partial x} \left( \lambda \frac{\partial T}{\partial x} \right) - \sum_{i=1}^N \dot{w}_i h_i \quad (4.5)$$

**Ideal gas equation of state:**

$$\rho = \frac{P}{RT} \quad (4.6)$$

In the above,  $\rho$  and  $u$  represent the gas density and velocity,  $Y_i$ ,  $D_i$ , and  $h_i$  represent the mass fraction, binary diffusion coefficient, and specific enthalpy of species  $i$ ,  $C_p$  and  $\lambda$  are the specific heat and thermal conductivity of the mixture, and  $R$  is the mixture gas constant. As noted above, low Mach number flow is assumed, so that the pressure is constant over the entire domain at each time  $t$ .

#### 4.5 Boundary Conditions and Deposition Model

Three types of boundary conditions are provided in the model; fixed value, zero flux / fixed gradient, and deposition. At the right boundary (the core gas region), vanishing gradients are imposed on all species concentrations and temperature. At the left boundary, the temperature is fixed, equal to the engine wall or burner surface temperature. The species concentration conditions at the left boundary are determined by the type of simulation; for wall quenching, zero flux conditions are specified at the wall surface, except for depositing species, whereas for burner flames, fixed flux fractions are imposed.

Depositing species present a special case; the boundary condition for these species is designed to provide for a range of deposition types, with a dependence on the species volatility:

$$F_i = -k_{dep}(P_i - P_i^*) \quad (4.7)$$

where  $F_i$  is the flux of species  $i$  at the left boundary (negative fluxes are towards the wall),  $k_{dep}$  is a rate coefficient (i.e. the condensation / evaporation rate),  $P_i$  is the partial pressure of species  $i$  at the left boundary, and  $P_i^*$  is the vapor pressure of species  $i$  at the wall temperature. Note that in the limit as  $k_{dep}$  goes to infinity, this condition reduces to  $P_i = P_i^*$ , and as  $k_{dep}$  goes to zero, the flux goes to zero. The dependence of  $P_i^*$  on temperature is given by the Clausius-Clapeyron relation:

$$P_i^*(T) = P_i^*(T_o) e^{\frac{-\Delta H_{v,i}}{R} \left( \frac{1}{T} - \frac{1}{T_o} \right)} \quad (4.8)$$

where  $\Delta H_{v,i}$  is the heat of vaporization of species  $i$ .

#### 4.6 Mass-Based Coordinate Transformation

The above equations, for a physical system containing  $N$  chemical species, reduce to a system of  $N+2$  linked partial differential equations in  $N+2$  independent variables ( $N$  species, temperature and gas velocity), with differential-algebraic boundary conditions. The numerical solution of these equations can be aided by the use of a mass-based coordinate system, which simplifies the equations to a more easily discretized form. We define a new spatial coordinate  $\zeta$  as shown in equation 4.9.

$$\zeta = \int_0^x \rho(x') dx' \quad (4.9)$$

In this coordinate system, the continuity requirement (equation 4.3) is satisfied by definition, and the species and energy conservation equations (equations 4.4 and 4.5 above) can be expressed as in equations 4.10 and 4.11:

$$\frac{\partial Y_i}{\partial \tau} = -\dot{m}_o \frac{\partial Y_i}{\partial \zeta} + \frac{\partial}{\partial \zeta} \left( \rho^2 D_i \frac{\partial Y_i}{\partial \zeta} \right) + \frac{\dot{w}_i}{\rho} \quad i = 1..N \quad (4.10)$$

$$\frac{\partial T}{\partial \tau} = -\dot{m}_o \frac{\partial T}{\partial \zeta} + \frac{1}{C_p} \frac{\partial}{\partial \zeta} \left( \rho \lambda \frac{\partial T}{\partial \zeta} \right) + \frac{1}{\rho C_p} \sum_{i=1}^N \dot{w}_i h_i \quad (4.11)$$

In the above equations,  $\zeta$  and  $\tau$  represent  $x$  and  $t$  in the transformed domain, and  $\dot{m}_o$  is the mass flow rate at  $\zeta = 0$ . Having eliminated the continuity equation and the gas velocity as an independent variable, we now have a system of  $N+1$  partial differential equations with boundary conditions in  $N+1$  independent variables ( $N$  species mass fractions and temperature), to be integrated in space and time given specified initial conditions.

#### 4.7 Adaptive Spatial Mesh Redistribution

Equations 4.10 and 4.11 must be solved numerically on a discrete grid. In the areas near the flame front, where concentration and temperature gradients are very steep, the grid spacing must be fine in order to resolve the important features of the flame. Since the flame front moves over the domain, we must either have fine grid spacing over the entire region of flame travel (which makes the calculation significantly more computationally expensive), or employ a method that allows the numerical grid to follow the flame front, concentrating grid points where they are needed and allowing wider grid spacing where gradients are low.

The adaptive spatial mesh technique used in this model does exactly that; in order to ensure that grid points are concentrated in regions where gradients need to be resolved, the algorithm distributes the available points based on a weighted average of the first and second derivatives of the species and temperature profiles. This is achieved by calculating a “mesh function”  $F_{mesh}$  based on the concentration and temperature profiles at any timestep (adapted from Larrotourou, 1993):

$$F_{mesh}(x) = a_i \frac{\int_0^x \left( \frac{\partial y_i}{\partial x} + K_c \right) dx'}{\int_0^L \left( \frac{\partial y_i}{\partial x} + K_c \right) dx'} + b_i \frac{\int_0^x \left( \frac{\partial^2 y_i}{\partial x^2} + K_c \right) dx'}{\int_0^L \left( \frac{\partial^2 y_i}{\partial x^2} + K_c \right) dx'} \quad (4.12)$$

where  $y_i$  represents species concentration or temperature,  $L$  is the length of the domain,  $a_i$  and  $b_i$  are the weighting coefficients for the first and second derivatives of series  $i$ , and  $K_c$  is a smoothing factor (as  $K_c$  is increased, the impact of the derivative values on  $F_{mesh}$  is diminished). The resulting function is used to distribute the grid points by requiring that the value of  $F_{mesh}$  should increase by the same amount (i.e.  $F_{mesh}(L)$  divided by the number of points) between each pair of grid points, subject to constraints on the minimum and maximum grid spacing. This ensures that in regions where gradients are significant (and hence  $F_{mesh}$  increases rapidly with  $x$ ) the grid points will be more closely spaced after the species and temperature profiles are interpolated onto the new mesh. Remapping of the mesh does not change the form of the numerical system, and hence may be done at any time during the calculation process, allowing the numerical grid to follow the gradients in the physical system efficiently.

#### 4.8 Discretization and Numerical Solution Techniques

To solve the above equations numerically, we must first express them in a discrete form. The method of lines is used to discretize equations 4.10 and 4.11. In this technique, the space derivatives are first replaced with finite differences (centered differencing is used in the main part of the domain, with upwind differencing at the boundaries). With  $M$  points used for the spatial differencing, this results in equation 4.13 for the time rate of change of the independent variable vector  $Y = [Y_{1,1}, Y_{N,1}, T_1, Y_{1,2}, Y_{N,2}, T_2, \dots, Y_{1,M}, Y_{N,M}, T_M]$  at any time  $\tau$ .

$$\frac{\partial Y}{\partial \tau} = f(Y, \tau) \approx J(Y, \tau) \cdot Y \quad (4.13)$$

where  $J(Y, \tau)$  is the Jacobian matrix of the linearized system.

The resulting sparse system of stiff coupled ordinary differential equations is integrated using the backwards differentiation method, as implemented in LSODES (Radhakrishnan and Hindmarsh, 1993). The integrator is coupled with the adaptive mesh algorithm described in the

previous section, such that each Jacobian recalculation is performed with an optimized mesh distribution.

#### 4.9 Code Structure and Organization

The code is implemented in C++, using a modular structure. The main components are the data module, which handles the processing of input and output, storage and manipulation of the species and temperature profiles, and generation of optimized spatial mesh distributions, the chemistry and transport modules, which provide reaction rates, heat release and thermodynamic and transport properties given a set of species concentrations, temperature and pressure, and the integrator module, which integrates the species profiles over time. The data module, in conjunction with the chemistry and transport modules, can calculate the time rates of change of species concentrations and temperature given a set of concentration and temperature profiles. The integrator module, based on LSODES, is used to perform the time integration of the system of differential equations. It is initialized by the data module with a starting set of species concentrations, a temperature profile, and a pressure history. It interacts with the data module during integration by requesting the time rates of change for the current set of profiles or by requesting an update of the spatial mesh. All effects of the spatial discretization are handled within the data module, while the integrator module uses implicit methods to perform adaptive discrete time steps. The end result is a series of spatial profiles, for all chemical species and temperature, that show the evolution of the system with time. A diagram of the structure and operation of the code is given in Figure 4.2.

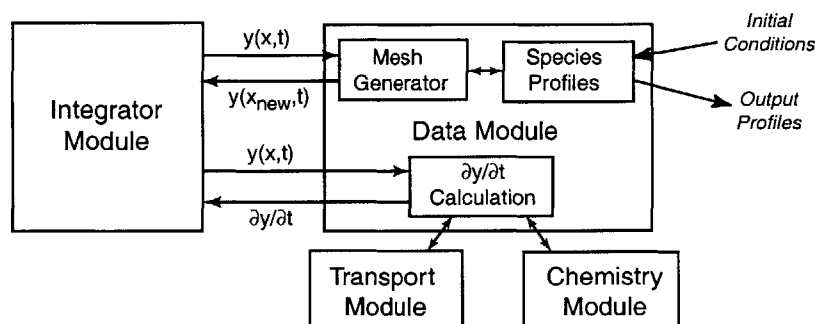


Figure 4.2. Structure and data flow in the numerical simulation code.

#### 4.10 References

- A. Burcat, "Thermochemical Data for Combustion Calculations," in W.C. Gardiner, ed., Combustion Chemistry, Springer-Verlag (1984).
- R.J. Kee, J. Warnatz, and J.A. Miller, "A FORTRAN Computer Program Package for the Evaluation of Gas-Phase Viscosities, Conductivities, and Diffusion Coefficients," *Sandia National Laboratories Report SAND83-8209* (1983).
- R.J. Kee, J.F. Grcar, M.D. Smooke, and J.A. Miller, "A FORTRAN Program for Modeling Steady Laminar One-Dimensional Premixed Flames," *Sandia National Laboratories Report SAND85-8240* (1985).
- R.J. Kee, F.M. Rupley, and J.A. Miller, "CHEMKIN-II: A FORTRAN Chemical Kinetics Package for the Analysis of Gas Phase Chemical Kinetics," *Sandia National Laboratories Report SAND89-8009* (1989).
- R.J. Kee, F.M. Rupley, and J.A. Miller, "The CHEMKIN Thermodynamic Data Base," *Sandia National Laboratories Report SAND87-8215B* (1990).
- B. Larrotourou, "Adaptive Numerical Simulation of Premixed Flame Propagation," in Taylor and Francis, eds., Numerical Modeling in Combustion, PPP (1993).
- P. Popp, M. Baum, M. Hilka and T.J. Poinot, "A Numerical Study of Laminar Flame Wall Interaction with Detailed Chemistry," in Direct Numerical Simulation For Turbulent Reacting Flows, Éditions Technip, (1996).
- K. Radhakrishnan and A.C. Hindmarsh, "Description and Use of LSODE, the Livermore Solver for Ordinary Differential Equations," *Lawrence Livermore National Laboratory Report UCRL-ID-113855* (1993).
- C.K. Westbrook and W.J. Pitz, "HCT: A General Computer Program for Calculating Time-Dependent Phenomena Involving One-Dimensional Hydrodynamics, Transport, and Detailed Chemical Kinetics," *Lawrence Livermore National Laboratory Report UCRL-52504* (1995).



### 5.1 Objectives of the Modeling Study

A number of insights into the deposition process can be gained through the use of the numerical model described in the preceding chapter *without* complex deposition chemistry. This chapter describes an exercise in simulating deposition from quenching ethylene-toluene flames under atmospheric conditions, with single-reaction precursor formation chemistry. There are a number of goals for this set of simulations: to validate the performance of the numerical model in predicting deposition rates and phenomena, to examine the interactions between precursor transport in the gas phase and condensation-evaporation processes at the wall surface, and to form a general picture of the most basic effects of precursor formation chemistry on deposition rates. In addition to these objectives, simulating a range of precursor volatilities and wall temperatures will allow us to determine if the model can reproduce observed experimental trends with fuel chemical structure, fuel component boiling points, and engine surface temperatures.

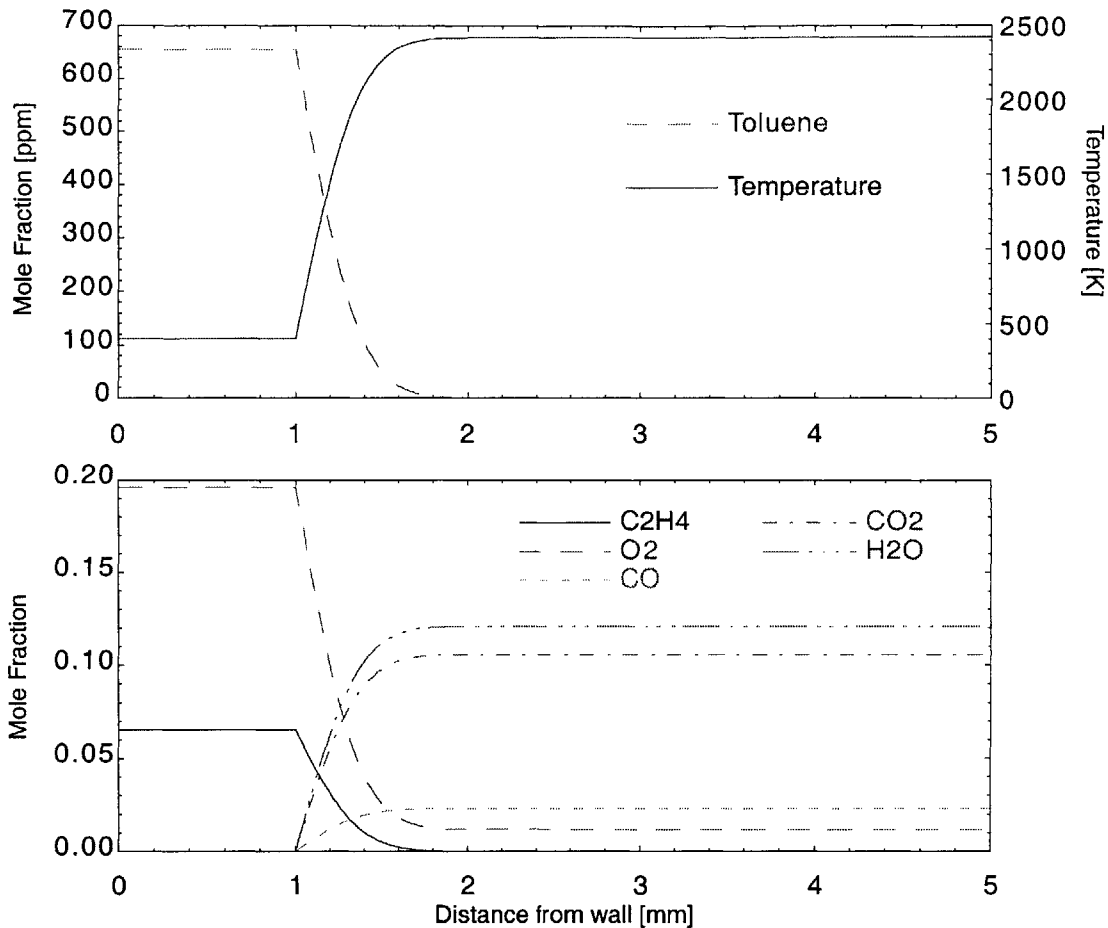
### 5.2 Simulation of Atmospheric Pressure Flame Quenching with Deposition

The model system chosen for this set of simulations is very straightforward; it consists of an atmospheric pressure flame propagating normal to a cooled wall surface and quenching as it reaches the surface. The unburned gas mixture consists of ethylene and toluene in air. Deposit formation is simulated with a simplified chemical mechanism that produces a hypothetical deposit precursor species from toluene, which may be transferred to the deposit layer at the wall; the mechanism is discussed in detail below. Different deposit precursors are modeled by assigning different physical properties to the hypothetical species produced from the toluene fuel. This system represents one of the simplest possible quenching flame deposition situations, and is also readily comparable to a set of experiments performed by Price *et al.* in an atmospheric pressure pulsed-flame deposition apparatus, using propane mixed with single-component liquid fuels (Price *et al.*, 1995). These experiments were chosen as a basis for comparison because they provide direct measurements of deposit growth rate as a function of fuel type, which may be

easily simulated via the numerical model. Ethylene, rather than propane, is used as the base fuel in the simulations since it can be modeled with a significantly smaller oxidation mechanism than propane, yet provides similar thermal environments and radical pools; this is sufficient for the level of detail considered here, and greatly decreases simulation time. Thus, this exercise provides an opportunity to test the performance of the model directly against existing literature data over a range of conditions, with no need to account for complex fuel compositions or the difficulties inherent in comparisons to engine test data. The purpose of the comparison is not to model the experimental results exactly, as there are too many parameters to consider even in this simplified system; rather, we will attempt to compare deposition rate on an order-of-magnitude level as a function of fuel and deposit precursor properties.

The inputs to the model are the pressure history (constant with time at one atmosphere), initial conditions for concentration and temperature profiles, and boundary condition definitions. A typical set of initial condition profiles is shown in Figure 5.1. The unburned fuel composition is stoichiometric with respect to the ethylene fuel; no oxidation chemistry is included for the toluene, so it has minimal effect on the flame propagation. The region of sharp temperature rise is the initial position of the flame front. To the left of the front, all chemical species are at their unburned concentrations and the temperature is equal to the wall temperature; to the right are equilibrium (post-combustion) species concentrations and temperature for adiabatic combustion. The flame front itself is given an initial width of about one millimeter and an error function profile; the initial shape of the front is unimportant, as it will relax to a correct profile as the solution progresses.

The left boundary in the figure, at  $x = 0$ , represents the engine wall (or surface of a pre-existing deposit layer), while the right boundary is in the bulk gases behind the flame front. Zero-gradient conditions are applied to all species and temperature at the right boundary. A fixed temperature boundary condition is used at the wall;  $T_w$  is varied over different simulation runs but is constant with time in each individual run.



**Figure 5.1.** Typical initial condition species and temperature profiles for the ethylene/toluene/air flame quenching simulations. Nitrogen and several minor species are not shown. The “precursor” species refers to a hypothetical deposit precursor whose physical properties may be varied to model a range of different input fuels.

For the deposit precursor species at the left boundary; a condensation / evaporation boundary condition is used (see Equation 4.6). We assume the condensation / evaporation rate to be extremely large, leading to the limiting case of a vapor-liquid equilibrium condition, in which the species partial pressure at the wall is fixed at its saturated vapor pressure at the wall temperature. This assumption is strictly accurate only if the deposit is modeled as a single-component liquid layer. However, since the goal of this analysis is to compare trends and order-of-magnitude rates, the functional relation of the boundary condition to the species volatility is much more important than the coefficient. Evaporation of species into the gas phase is permitted at any time, which assumes a sufficiently large amount of condensed species in the deposit layer;

it was found that evaporation fluxes were small in the simulations, so this assumption should not be a significant source of error.

For the ethylene oxidation chemistry, the mechanism of Griffiths, *et al.* is used, without modification (Griffiths *et al.*, 1995). A listing of the species and reactions included in the mechanism is found in Appendix I. Thermodynamic properties of the species are taken from the reference database of Kee *et al.*, and equilibrium concentrations for the burned gases are calculated using the CHEMKIN-II version of the STANJAN equilibrium code (Kee *et al.*, 1989; Reynolds, 1986; Kee *et al.*, 1990).

### 5.3 Single Step Precursor Formation Chemistry Approximation

The precursor formation chemistry model used in these simulations is meant to provide realistic rates of formation of a deposit precursor species from a heavy hydrocarbon fuel, without the complexity of an elementary step chemical reaction mechanism. Hence, a single-step reaction is used, with toluene as the initial fuel component, with the rate dependent only on temperature:



The precursor species that is formed by this reaction is assumed to have identical physical and thermodynamic properties to toluene, with the exception of volatility, as discussed below. The rate constant  $k_{pre}$  is chosen to be representative of partial oxidation of toluene; its variation with temperature is given by the following expression (Seuwen and Warneck, 1996; Emdee *et al.*, 1992):

$$k_{pre} = 10^{12} e^{\frac{-25100}{T}} \quad (5.2)$$

In order to use this system to model the effects of different fuel and deposit precursor chemical structures, the volatility of the deposit precursor species was varied by adjusting its vapor pressure at the wall temperature, while all other properties were kept constant. The vapor pressures used ranged from 0.0001 to 0.05 atmospheres at 300 K wall temperature, corresponding to precursor boiling points from 550 K to 390 K, respectively.

The deposit precursor boiling points chosen for this series of simulations begin at the high end of gasoline component boiling points (for example, the boiling point of toluene is 383

K) and range to significantly higher values. This reflects the assumption that the fuel components themselves are too volatile to deposit at the engine wall temperatures; these calculations will test that assumption.

This chemistry model is extremely simplified, and as such cannot capture a number of important effects, such as the role of oxygen in the precursor formation process, or the competition between precursor formation and oxidation in the gas phase. However, it is useful for exploring broad ranges of input conditions, as well as for examining some basic interactions between, chemistry, transport and deposition.

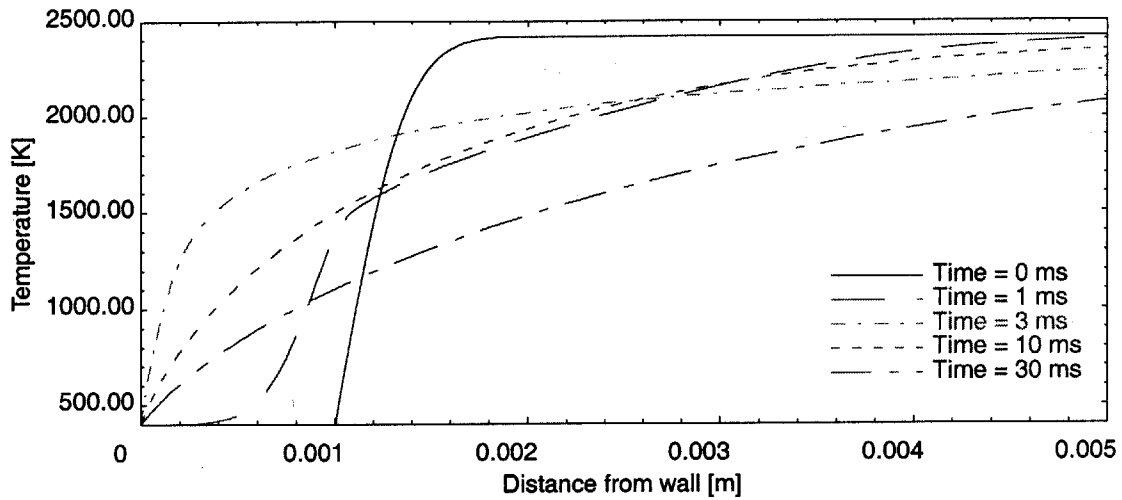
#### 5.4 Deposition from Single Flame Quench Events

The above model was used to simulate flame quench events over a range of conditions, with varying toluene mole fractions in the input fuel, deposit precursor volatilities, and wall temperatures. The test matrix is listed in Table 5.1. The same form of initial condition, as shown in Figure 5.1, was used for all runs. The numerical simulation was run through the flame propagation and quenching process, which lasted approximately 30 milliseconds in all cases.

Variable	Range
Toluene Input Concentration	1 - 5 molar percent of total fuel
Precursor Vapor Pressure (Boiling Point)	0.0001 - 0.05 atm (550 - 390 K)
Wall Temperature	300 - 500 K

**Table 5.1.** Range of parameters used in the ethylene/toluene/air flame quenching simulations.

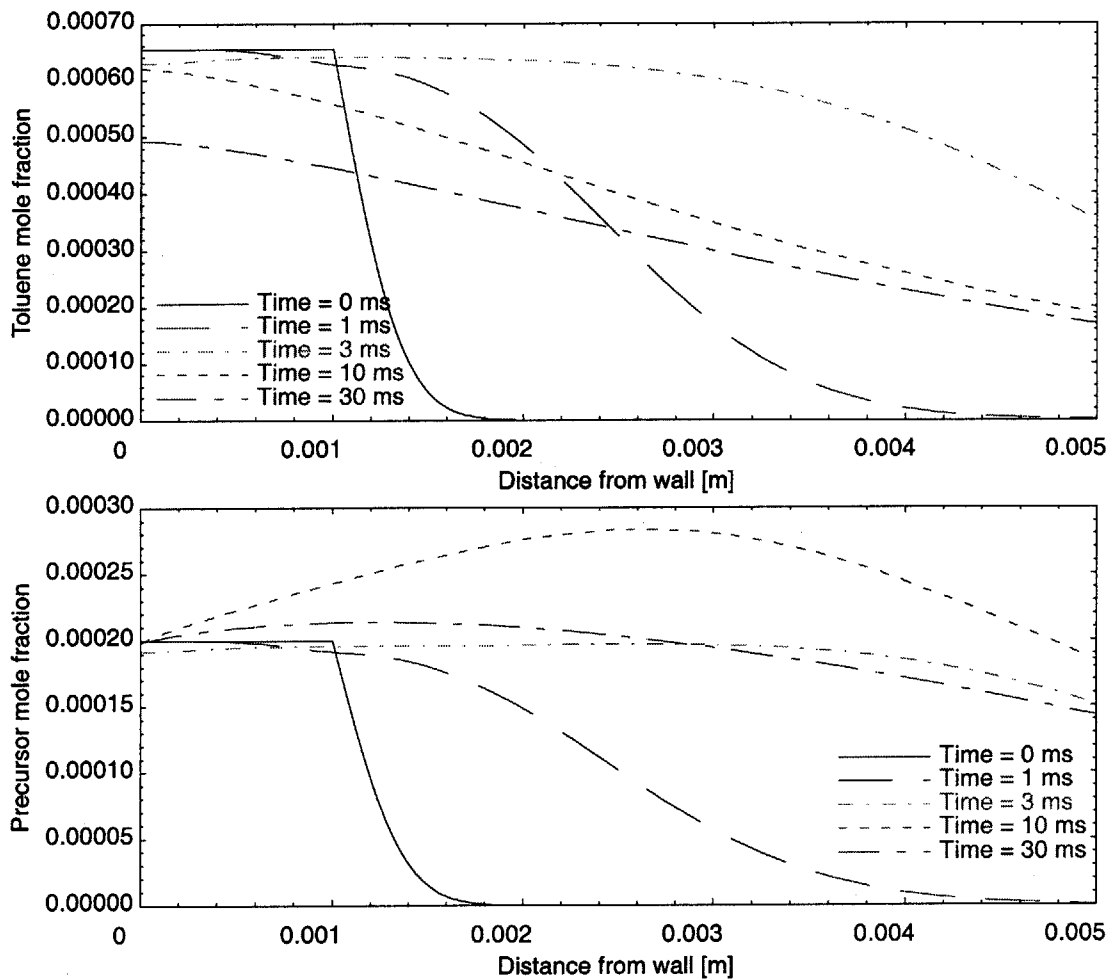
Figures 5.2 through 5.4 show several features of a typical simulation result. In the first three figures, the propagation of temperature and several species profiles with time is shown, for a case with a wall temperature of 400 K, fuel composition of 99 percent ethylene, 1 percent toluene, and a precursor vapor pressure of 0.0002 atm (approximately 500 K boiling point). These plots illustrate the interactions between the flame propagation and quenching and the formation and transport of the deposit precursor species.



**Figure 5.2.** Time evolution of temperature profiles in a quenching ethylene/toluene/air flame.

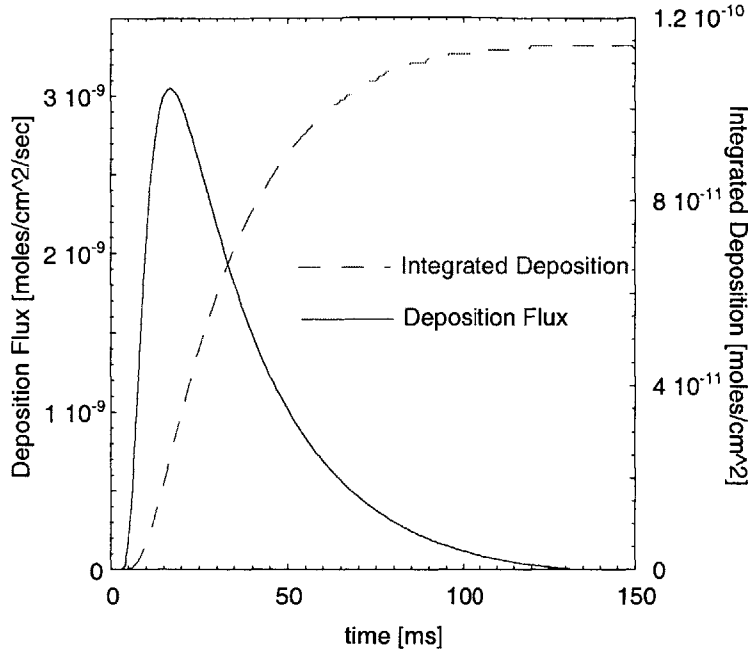
The flame propagation and quenching can be seen from the temperature profile in Figure 5.2. The flame front reaches its closest approach to the wall at 3 milliseconds after the start of the simulation; at that point, the heat losses to the wall slow the reactions to the point that the flame cannot propagate any further. The rates of reaction in the region near the wall continue to decay for the rest of the simulated quench event.

Figure 5.3 shows the evolution of the toluene and deposit precursor concentrations during the flame quenching. As the flame moves into the unburned gases, toluene is converted to the deposit precursor species near the flame front. This results in a buildup of the precursor species propagating ahead of the flame front, both through chemical production and diffusion. Once a sufficient amount of the precursor reaches the wall (i.e. greater than the saturated vapor pressure), deposition begins, and will continue until the precursor concentration at the wall once again drops below the deposition limit. In this model, which does not consider further oxidation of the precursor, the processes affecting the precursor concentration after the flame quenches are deposition to the wall surface, diffusion both towards and away from the wall, and convection towards the burned gases.



**Figure 5.3.** Concentration profiles of toluene and the deposit precursor species at several times during the flame quench event (see temperature profile in Figure 5.2.).

The interactions between these various processes result in a profile of deposition flux at the wall versus time such as the one shown in Figure 5.4. The initial rapid rise in deposition occurs as the flame front reaches the wall and begins to quench; the rest of the profile is determined by the competing effects of deposition, convection and diffusion. Note that the maximum deposition flux occurs after the flame has begun to quench; the precursor production reaction and diffusion towards the wall still have significant effects for several milliseconds after the beginning of quenching. The integrated deposition flux is also shown in Figure 5.4. This gives the total amount of deposit per unit area produced during the flame quench event.



**Figure 5.4.** Deposition rate and integrated total deposition at the wall surface during the flame quenching process shown in Figures 5.2 and 5.3.

The type of simulation described in Figures 5.1 through 5.4 was carried out for a range of precursor boiling points, initial toluene mole fractions, and wall temperatures, as listed in Table 5.1. In each case, the deposition flux and integrated total deposition were calculated. The effects of the main simulation variables on the deposition amount can be seen easily through the use of two normalizations. The first is to express the integrated deposit mass per unit area as a fraction of the input mass of toluene per unit area; thus, the deposit mass fraction  $Y_{dep}$  is given by:

$$Y_{dep} = \frac{\int_0^T F_{dep} dt \Big|_{x=0}}{\int_0^L X_{tol} \frac{P}{RT} dx \Big|_t} \quad (5.3)$$

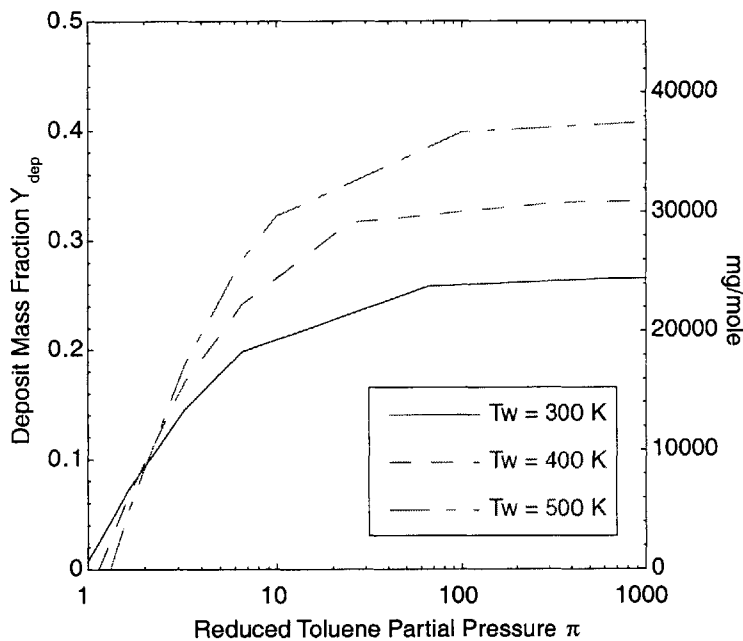
We can also normalize the input amount of toluene with respect to the precursor volatility; if we consider that in order to produce deposition, the precursor partial pressure must exceed its saturation vapor pressure at the wall temperature, and that the precursor must be formed from the input toluene, we find that the toluene partial pressure in the unburned gas mixture must equal or exceed the precursor saturation vapor pressure in order to produce deposition. Based on this reasoning, we define a reduced partial pressure of toluene  $\Pi_{tol}$  as:



$$\Pi_{tol} = \frac{P_{toluene}}{P_{precursor}^*} \quad (5.4)$$

If this value is less than one, deposition cannot occur in the simulated flame quenching process. However, a value of  $\Pi_{tol}$  greater than one does not guarantee deposition will occur; the production rate of precursor from the toluene might be insufficient, or diffusion or convection could transport the precursor away from the wall surface too quickly.

Plotting the simulation results in the form of the deposit mass fraction as a function of reduced partial pressure of toluene results in all the cases falling onto a set of curves that vary only with wall surface temperature, as shown in Figure 5.5. This plot has several interesting features. The first is that each of the three curves reaches a plateau value as the reduced partial pressure is increased. This plateau corresponds to the condition at which the deposition rate is controlled solely by the rate of diffusion of deposit precursor to the wall. The diffusion-limited regime also explains the fact that the plateau value increases with increasing wall temperature. The use of the reduced toluene vapor pressure on the x axis incorporates the effect of wall



**Figure 5.5.** Deposit mass fraction versus reduced partial pressure of toluene for the simulations described in Table 5.1. Primary y axis is in units of deposit mass fraction (see equation 5.3); secondary y axis is converted to units of mg/mole for comparison with the data of Price, *et al.*

temperature on the deposit precursor saturation vapor pressure. Thus, the effects of wall temperature on the deposit mass fraction curves are not related to the precursor volatility; they are due instead to the effects of the unburned gas temperature (which is equal to the wall temperature) on rates of diffusion and precursor formation. Higher unburned gas temperatures

will increase both the initial production of precursor molecules and the diffusion rates of the precursor to the wall; hence, higher temperatures lead to higher deposit fluxes in the diffusion-limited regime.

### 5.5. Comparison with Literature Data

The compiled simulation results in Figure 5.5 also provide a useful basis for comparison to the pulsed deposition rig data of Price *et al.* introduced earlier in this chapter. The main features of the numerical results that can be related to the experimental data are the following: the deposit mass fraction reaches a plateau value at sufficiently high input concentrations of deposit-forming fuel components or sufficiently low deposit precursor volatilities, and the value of the limiting deposit mass fraction is between 0.25 and 0.4.

The constant deposit mass fraction is clearly observed in the data of Price *et al.* While varying the input amounts of several alkylbenzene compounds used as dopants in a propane-air flame (ethylbenzene, toluene, isopropylbenzene, n-butylbenzene and n-amylnbenzene), they observed a linear relation between dopant delivery rate and deposit amount during fixed-duration tests. This type of relation would hold in the diffusion-limited plateau regime of the simulation data.

The slopes of these linear deposit - dopant flow rate relations are analogous to the deposit mass fraction used in Figure 5.5. For alkylbenzene compounds, Price *et al.* found deposit fractions ranging from 200 to 1000 milligrams of deposit per mole of fuel, while for double-ring aromatics and higher the deposit fractions were between 5000 and 70000 mg/mole. The second axis in Figure 5.5 is labeled in units of milligrams per mole; the plateau values of 25000 to 35000 mg per mole do fall into the range of observed values.

### 5.6. Conclusions

Despite the extremely simplified chemical mechanism employed, the model discussed in this chapter provides interesting results regarding the interactions of chemistry, transport and deposition during the flame quenching process. The time-resolved simulation gives a clear picture

of the gas phase events leading to eventual deposition at the wall surface. The prediction of a constant mass fraction deposition, achieved in a diffusion-limited regime, is in agreement with literature data, and the predicted amount of deposition is of the correct order of magnitude. The agreement of these results with the experimental evidence also suggests that the simple condensation model used for deposition at the wall surface can produce realistic deposition behavior over a range of conditions.

## 5.7 References

- J.L. Emdee, K. Brezinsky, and I. Glassman, "A Kinetic Model for the Oxidation of Toluene Near 1200 K," *Journal of Physical Chemistry* Vol. 96, 2151-2161 (1992).
- J.F. Griffiths, K.J. Hughes, M. Schreiber and C. Poppe, "A Unified Approach to the Reduced Kinetic Modeling of Alkane Combustion," *Combustion and Flame*, Vol. 99, 533-540 (1995).
- R.J. Kee, F.M. Rupley, J.A. Miller, "CHEMKIN-II: A FORTRAN Chemical Kinetics Package for the Analysis of Gas Phase Chemical Kinetics," Sandia National Laboratories Report SAND89-8009 (1989).
- R.J. Kee, F.M. Rupley, and J.A. Miller, "The CHEMKIN Thermodynamic Data Base," Sandia National Laboratories Report SAND87-8215B (1990).
- R.J. Price, J.P.T. Wilkinson, D.A.J. Jones, and C. Morley, "A Laboratory Simulation and Mechanism for the Fuel Dependence of SI Combustion Chamber Deposit Formation," *Society of Automotive Engineers* 952445 (1995).
- W.J. Reynolds, "The Element Potential Method for Chemical Equilibrium Analysis: Implementation in the Interactive Program STANJAN," Department of Mechanical Engineering, Stanford University (1986).
- R. Seuwen and P. Warneck, "Oxidation of Toluene in NO<sub>x</sub> Free Air: Product Distribution and Mechanism," *International Journal of Chemical Kinetics*, Vol. 28, 315-332 (1996).



## Chapter 6

### *Flat Flame Burner Apparatus and Diagnostics*

#### 6.1 Experimental Objectives

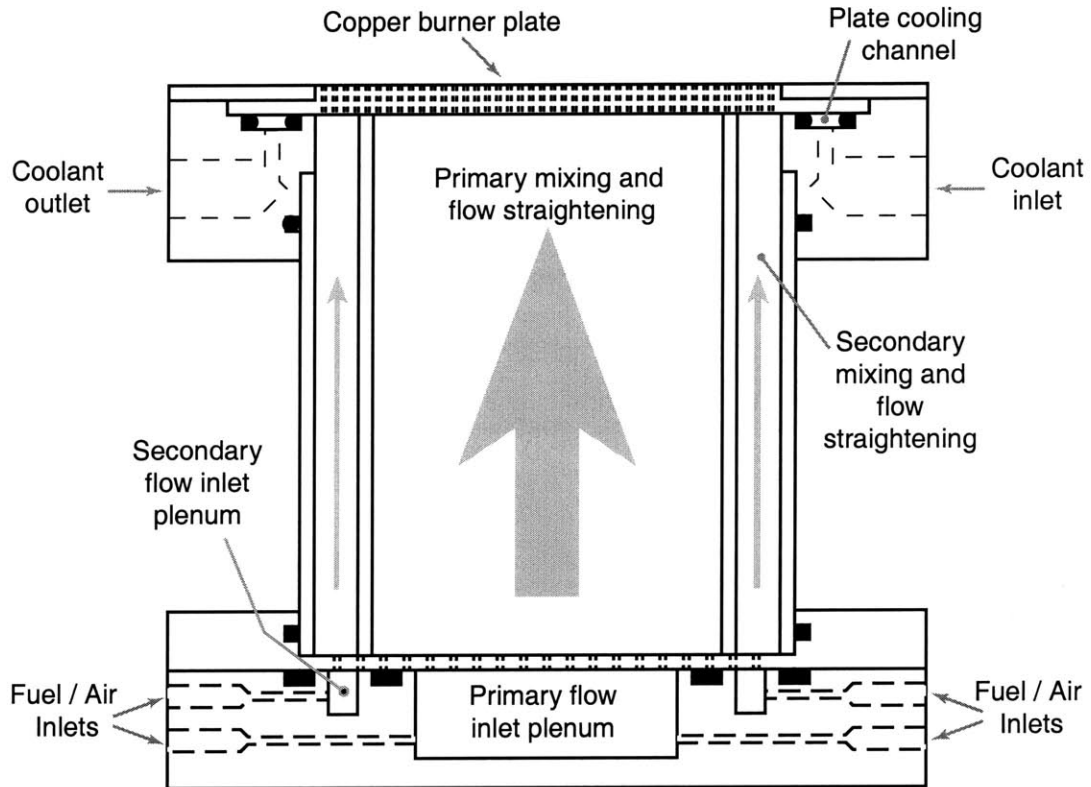
The low pressure flat flame burner system described in this chapter is designed to provide a highly controlled system for the production of steady-state, quasi-one-dimensional (cylindrically symmetric) quenching flames, specifically with propane doped with vaporized toluene as the fuel. The flames should be structured and controlled so as to allow high-resolution sampling in the flame quench layer. This requires the ability to specify system pressure, fuel and air flow rates, burner surface temperature and other variables. This chapter describes the apparatus and diagnostics used to produce, control and characterize the flame and its overall properties; the following chapter will describe the sampling and analytical chemistry components of the system.

#### 6.2 Flat Flame Burner System

A diagram of the flat flame burner is shown in Figure 6.1. The cylindrical burner consists of a flow distribution system in the bottom section, mixing and flow straightening sections in the center, and a copper burner plate with a water cooling jacket at the top. The burner plate is detailed in Figure 6.2. The choice of a drilled plate rather than a porous or sintered plate was made for two reasons; firstly, to provide increased thermal conductivity and hence better control over the burner surface temperature, and secondly to provide a surface for deposition that will not increase the plate's resistance to flow. While significant levels of deposition are not expected from the flames used for this study (due to the low concentrations of toluene in the fuel), deposition has been observed in similar systems using benzene-air flames to a degree that can clog sintered plates and even block drilled-hole plates (Bittner, 1985).

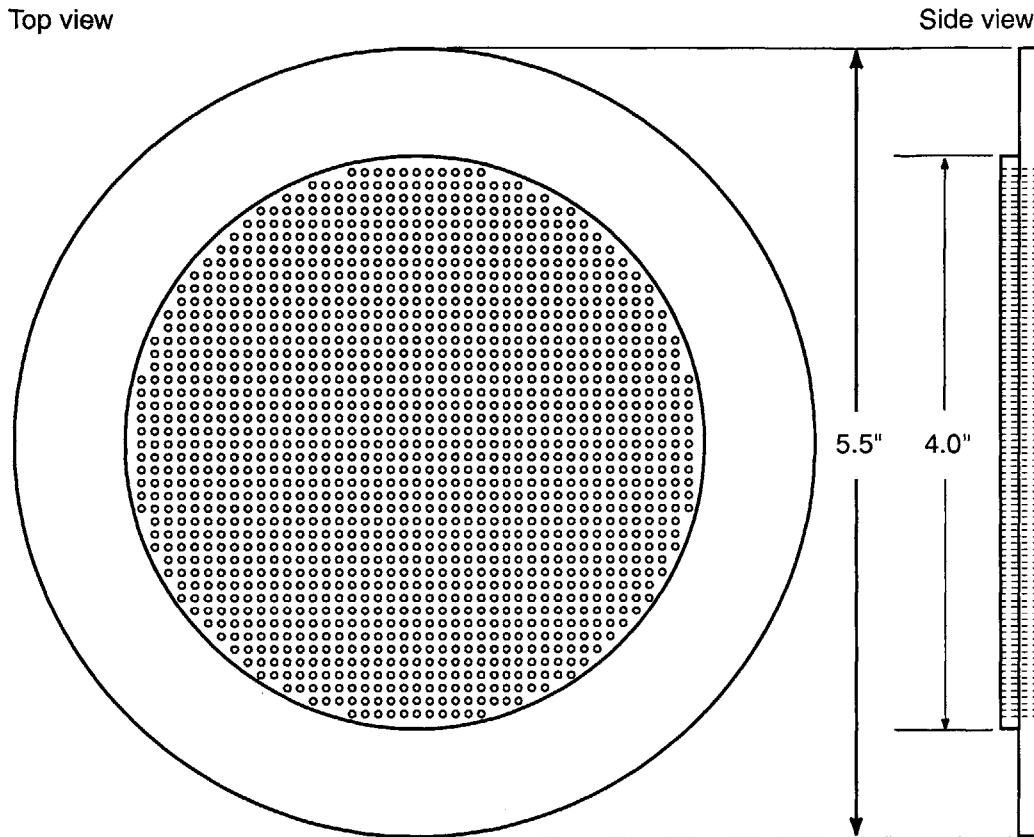
The section of the plate that is drilled for gas flow is four inches in diameter; holes are  $3/64$  inches in diameter and are spaced in a centered grid with 0.09 inch grid spacing. The total of 1481 holes represent twenty percent of the area of the central plate section. The outer annulus on the plate is used for cooling; water flows through a channel below the outer rim of the plate, in

direct contact with the lower surface. The plate surface temperature is controlled via the flow rate of the coolant water. Plate temperature is measured using three type K thermocouples mounted below the central section at approximately zero, one and three centimeters radially from the plate center.



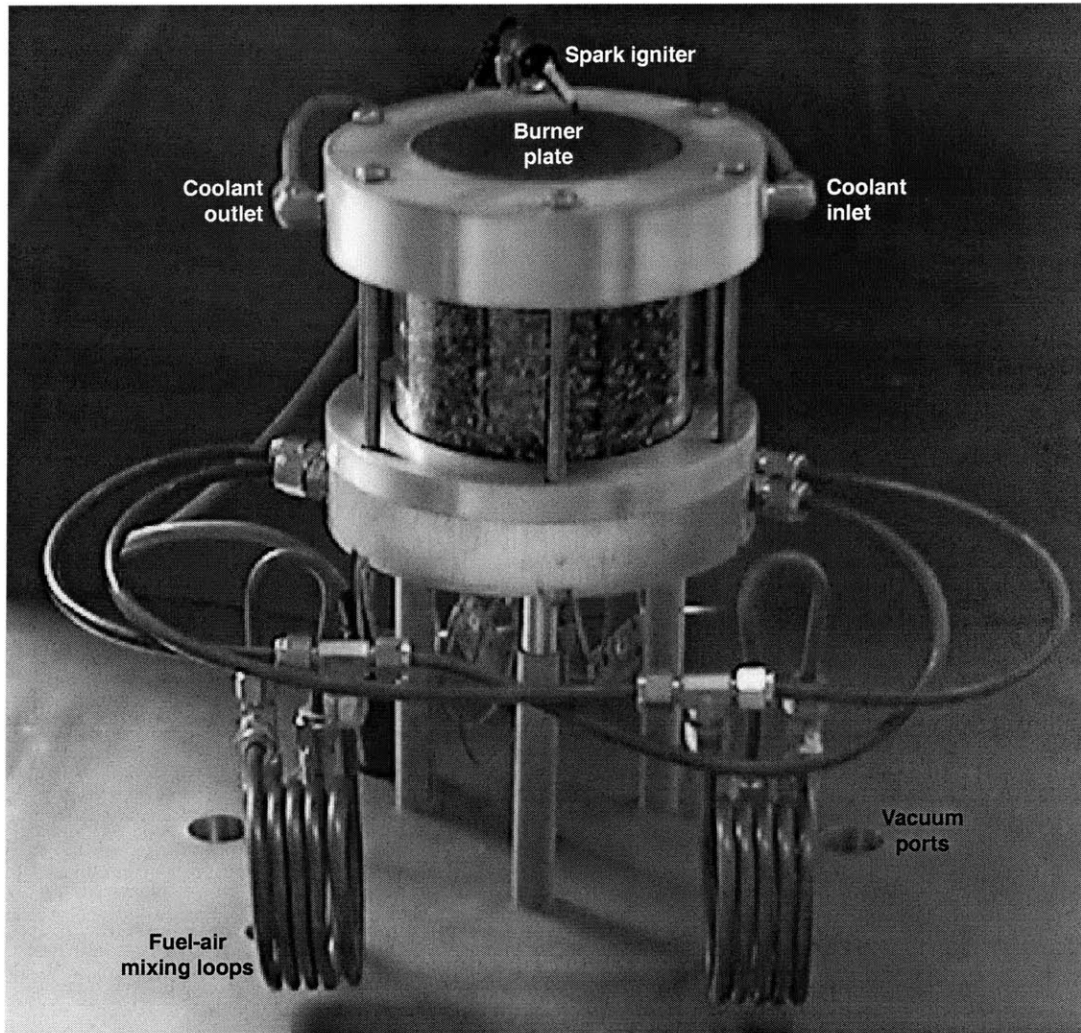
**Figure 6.1** Schematic diagram of the flat flame burner apparatus.

The gas flows are divided into two areas: a central cylinder approximately 8 centimeters in diameter surrounded by an annular region with an outer diameter of approximately 10 centimeters and width of 1.5 centimeters. Pure fuel, air, or premixed fuel and air can be delivered to the two flow channels via two symmetric pairs of inlets on the lower plenum; one set leads to a central cylindrical mixing chamber, while the other enters into a surrounding annular mixing chamber. The inlets are positioned off-center in order to create swirling flows in the mixing sections. Each of the flows passes through the lower drilled plate and must flow through a further mixing and flow straightening section; filled with stainless steel wool mesh, before exiting the burner through the drilled plate.



**Figure 6.2.** Copper burner plate (3:4 scale). Total plate thickness is  $1/4''$ . The central region of the plate is drilled with 1481 holes,  $3/64''$  in diameter, in a centered grid with center-to-center spacing of  $0.09''$ .

The division of the flow serves several purposes. To ignite the premixed flame, pure propane fuel is supplied to the outer ring, with no flow in the center, the propane is ignited via an electrical arc, producing an annular diffusion flame. Premixed fuel and air may then be supplied to the central flow region, which will be ignited immediately upon exiting the plate surface by the diffusion flame surrounding it. With the central premixed flame burning, a shield flow of air or nitrogen may be passed through the outer ring; this provides a more stable temperature boundary condition on the edges of the premixed flame, which in general will allow the premixed flame to be flat over a larger radius than otherwise. The ring section can also be used to produce an annular premixed flame; in this configuration, the inner flame edges will be stabilized at the height of the outer flame, which extends the lean and rich blow-out limits on the inner flame stoichiometry.



**Figure 6.3.** The flat flame burner mounted on the vacuum chamber baseplate.

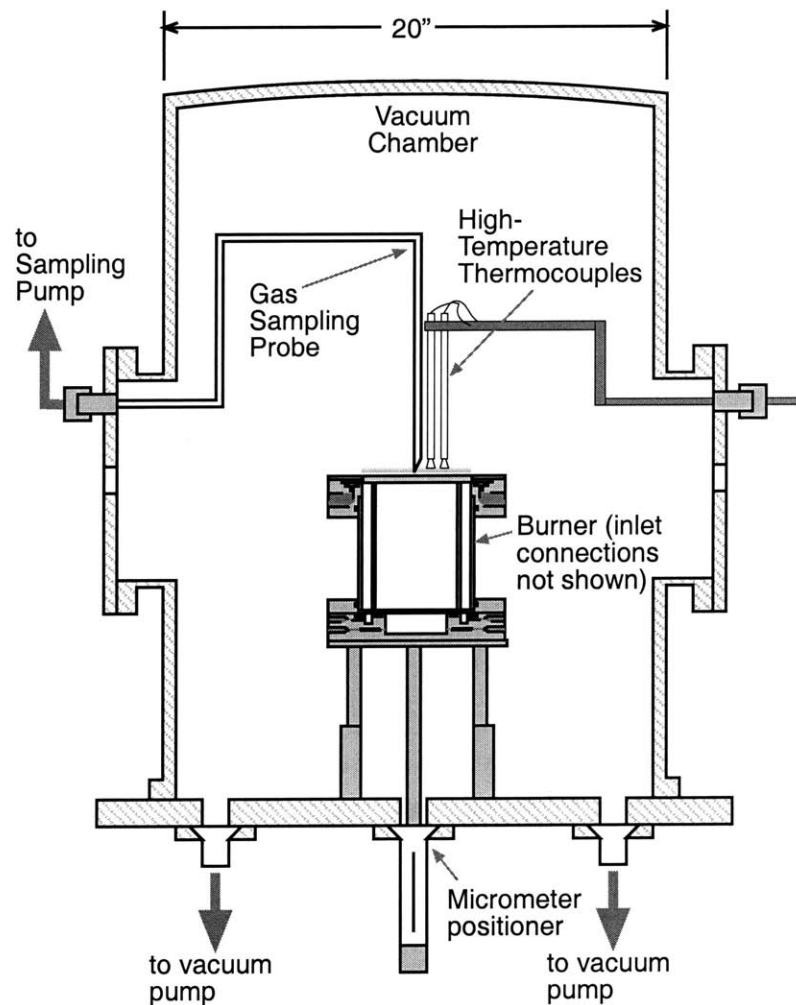
An image of the burner assembled to the baseplate of the vacuum chamber is shown in Figure 6.3. Fuel and air for both outer and inner burner flow sections are brought into the chamber from separate inlets with flame arrestors, are premixed in one-meter mixing loops, and are then sent into the swirl inlet ports. The burner is mounted on a three point spring-loaded suspension which is integrated with an axial micrometer positioner, allowing movement of the entire burner apparatus in the radial direction, with resolution better than 0.1 millimeters and repeatability to within 0.2 mm. The plate coolant system and arc igniter are also indicated in the figure.



### 6.3 Vacuum System and Pressure Control

In order to provide a large enough flame standoff distances to allow for sampling of species profiles, the burner must be operated at pressures less than 250 millibar. The vacuum chamber and diagnostic feedthroughs are illustrated in Figure 6.4. The stainless steel chamber is 20 inches in diameter and approximately 34 inches high, with an internal volume of 170 liters; it seals via its own weight with a captive o-ring. Two ten-inch flanges are mounted across from each other, centered at twelve inches high, which contain the feedthroughs for the gas temperature measurement and sampling apparatus (discussed later in this chapter and in Chapter 7). At ninety degrees to the side flanges, and at the same height, is a 4 inch window that is used to observe the flame and capture images.

The main pump apparatus is based on a Varian two-stage rotary vane pump with a maximum pumping speed of 1100 liters per minute and ultimate pressure of approximately 1 millibar. The chamber is connected to the pump through symmetrical ports to the sides of the burner (shown in Figures 6.3 and 6.4). A wire screen condensation trap is used on the pump inlet in order to remove highly condensable species from the gas stream, and a



**Figure 6.4.** Vacuum chamber and diagnostic feedthrough systems. Viewing port not shown (located at 90° around the chamber circumference from the feedthrough flanges, and at the same height).

condensate collector is placed at the pump outlet to prevent water from the pumped combustion products from reentering the pump. The pump is operated at elevated temperatures (approximately 150 °C) to avoid condensation of product water in the pump oil.

The chamber pressure is regulated by an active control system. It is important to provide very stable pressure conditions, as any significant change in the operating pressure will alter the standoff distance of the flame and introduce errors into the profile measurements. The chamber pressure is measured by a Setra Systems model 205 transducer mounted in the baseplate, with a range of 0 - 2 bar and error of  $\pm 0.5$  millibar. This signal is used as the input to a PID control circuit. The control actuator is a Tylan mass flow control valve (FC-261) connected in parallel with a bypass valve at the pump inlet. The degree to which the bypass valve is opened determines the available range of controlled pressures. At any given bypass setting, pressure can be controlled to within  $\pm 1$  millibar variation over a total range of approximately 70 millibar. Using the entire range of bypass levels, the controllable pressure range is 70 to 500 millibar (the lower limit is due to the limited conductance of the control and bypass valves, whereas the upper limit is due to the maximum achievable resistance of the control valve). Without the active control system, changes in ambient and pump temperatures can cause pressure drift of tens of millibar over a few minutes.

#### **6.4 Flow and Temperature Measurements and Control**

The main propane and air flows are metered by mass flow controllers (Tylan model FC-260), providing flow rates up to 10 standard liters per minute of air and 0.4 standard liters per minute of propane. The secondary propane and air (or inert gas) flows are controlled via rotameters paired with needle valves, providing similar flow rates.

The cooling water flow to the burner is also measured by rotameter; typical coolant flow rates are from 1 to 5 liters per minute. Coolant temperature is measured via thermocouples both before entering and after exiting the vacuum chamber; the temperature rise and flow rate can be used to estimate the heat loss from the flame to the burner plate.

### 6.5 Dopant Vaporization and Injection System

Metering, vaporization and injection of the heavy hydrocarbon dopant fuel (toluene in these experiments) is accomplished via the system shown in Figure 6.5. It consists of a liquid fuel storage tank pressurized to approximately 2 atmospheres with nitrogen, a high-resolution rotameter, and a vaporizer apparatus. In the vaporizer, the liquid fuel is delivered into a fiberglass mesh which is heated via heating tape to approximately 150 °C. The main air flow passes through the mesh, and carries the dopant with it into the burner as vapor. The system is designed to supply up to ten percent of the total fuel carbon via vaporized toluene, which corresponds to 0.6 milligrams per second of toluene at the maximum propane flow of 13 milligrams per second. In this range of flow rates, the partial pressure of dopant in the air stream is significantly below its vapor pressure; the highest concentrations of toluene used corresponded to a mole fraction of 0.002 in the air stream, whereas the vapor pressure of toluene at room temperature is approximately 0.01 atmospheres. The concentrations of dopant in the air stream are also significantly lower than the combustion limits.

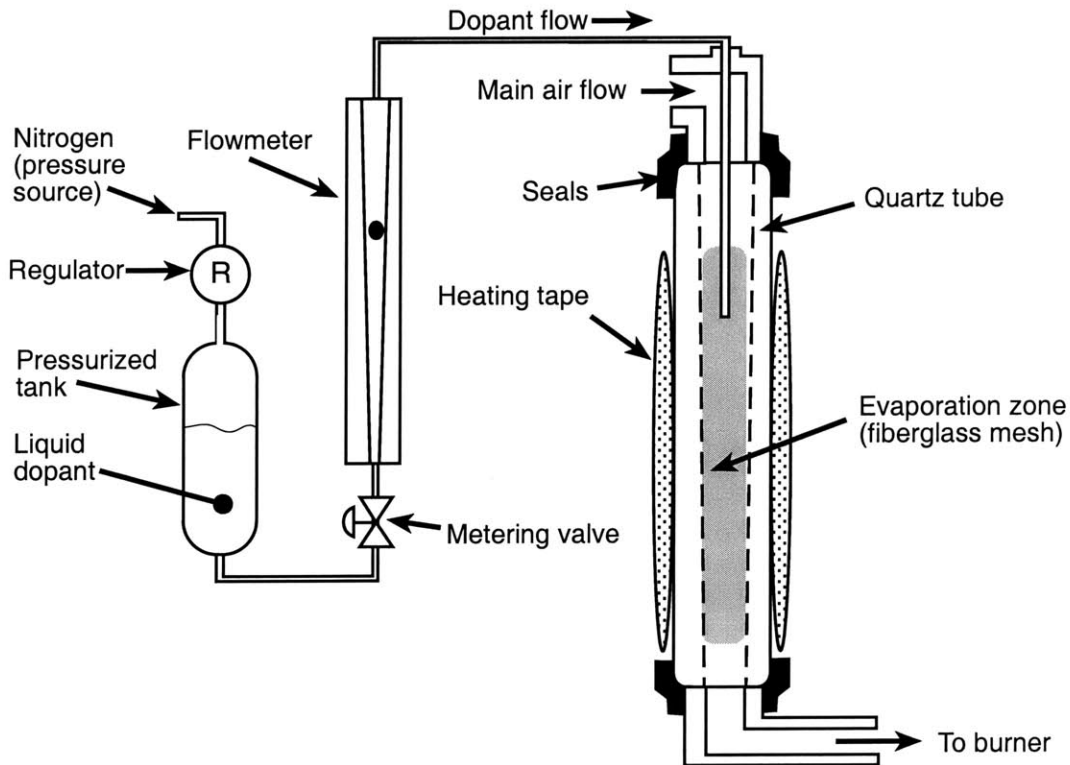


Figure 6.5 Dopant vaporization and delivery system.

## 6.6 Flame Temperature Measurements and Radiation Corrections

The temperature profiles of the experimental flames are measured via a dual-thermocouple probe, to allow correction for radiative heat loss from the thermocouples. The measurements are made via two coated Pt/Pt-13%Rh thermocouples (Type R) with wire diameters of 0.076 and 0.051 mm. The mean gas temperature  $T_g$  is related to the thermocouple temperatures  $T_1$  and  $T_2$  by Equation 6.1 (Heitor and Moreira, 1993):

$$T_g = \frac{C_1 T_1 - C_2 T_2}{C_1 - C_2} \quad C_i = \frac{\text{Nu}_i k}{\sigma d_i (T_i^4 - T_\infty^4)} \quad (6.1)$$

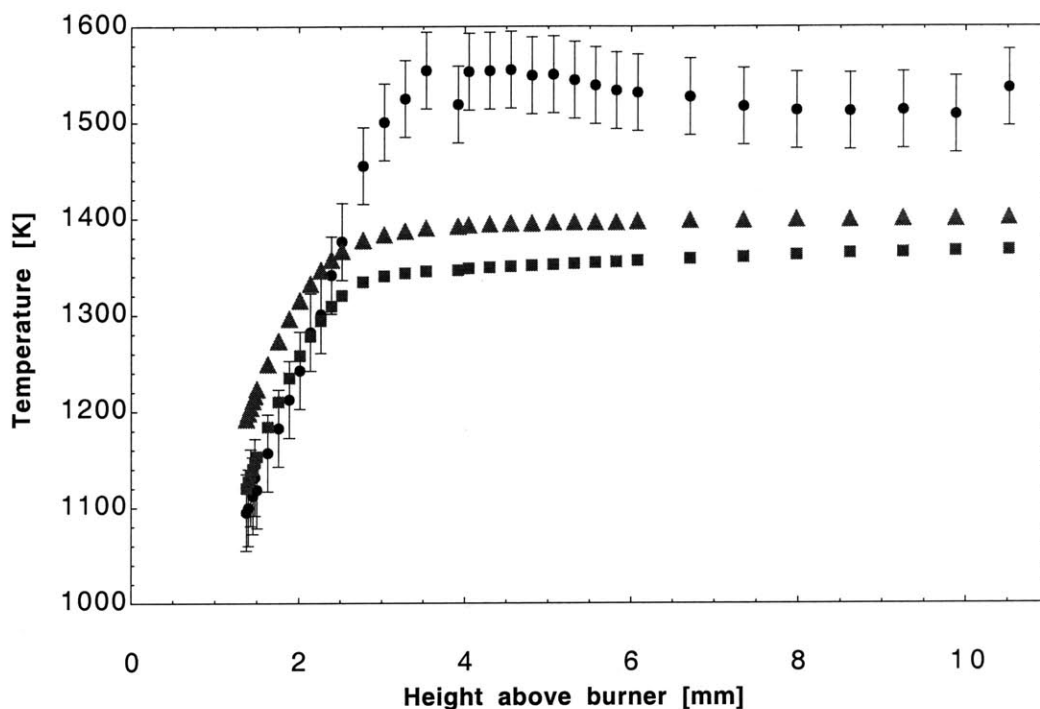
where  $k$  is the thermal conductivity of the gas,  $\sigma$  is the Stefan-Boltzmann constant,  $T_\infty$  is the temperature of the radiative environment, and  $\text{Nu}_i$  is the Nusselt number defined for the diameter of thermocouple  $i$ , determined by the correlation in equation 6.2,

$$\text{Nu}_D = 0.43 \text{Pr}^{0.38} + 0.5 \text{Re}_D^{0.5} \text{Pr}^{0.38} \quad (6.2)$$

where the wire diameter  $d_i$  is used as the length scale  $D$  for the Reynolds number. Equation 6.1 is solved iteratively, using the mean temperature of the two thermocouples as an initial guess.

The temperature probe, indicated in Figure 6.4, is designed to suspend the two thermocouples at equal heights in the vacuum chamber, at a separation of 2 centimeters in the radial direction. As the burner is moved, the thermocouples can record temperatures at different axial distances above the burner surface. The thermocouples themselves are mounted on 0.010" support wires in a triangular geometry with the bead in the middle of the horizontal triangle leg, so that conduction losses to the leads are minimized. The support wires are threaded through ceramic mounts which are connected to the probe mounting.

The largest source of error in the temperature measurement is the slight difference in height of the two thermocouple beads. In use, the lead wires shift slightly due to heating from the flame, causing unavoidable offsets of approximately 0.5 mm. This degree of offset can cause an error of approximately 50 Kelvin in the sharpest temperature gradients observed in the flames, where the measurement is most sensitive to offset. A sample plot of corrected temperature measurements in a propane-air flame, along with the thermocouple measurements, is given in Figure 6.6.

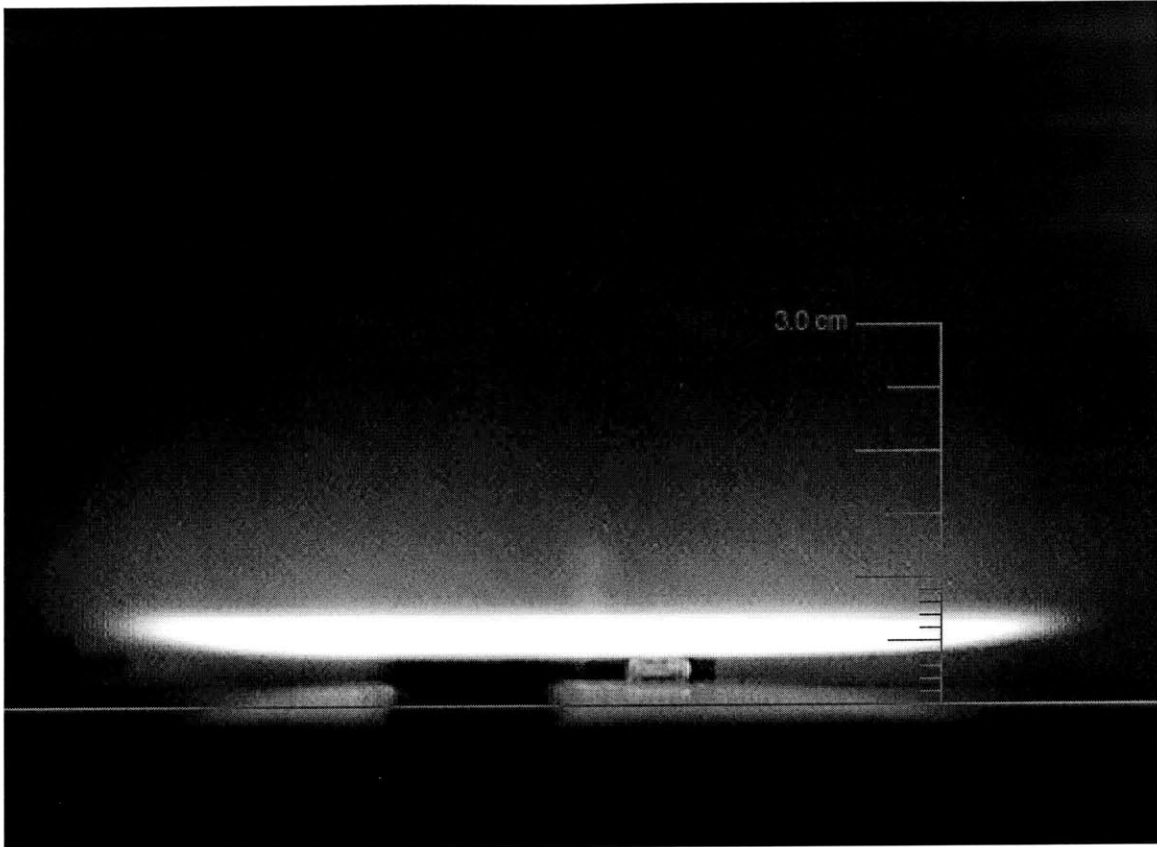


**Figure 6.6.** Uncorrected and corrected temperature profiles from a propane air flame, at  $\phi = 1.0$ ,  $p = 165$  millibar, and unburned gas velocity of 15 cm/s.

### 6.7 Observed Flame Properties and Operational Limits

Testing of the burner apparatus and exploration of its range of operation was performed using undoped propane-air flames. The burner has been operated with propane-air equivalence ratios of 0.4 to 2.5 (without use of the stabilizing ring flame), and pressures from 25 millibar to atmospheric (70 to 300 millibar with active pressure control). Burner surface temperature can be varied from 50 °C to 140 °C through control of the coolant water flow rate.

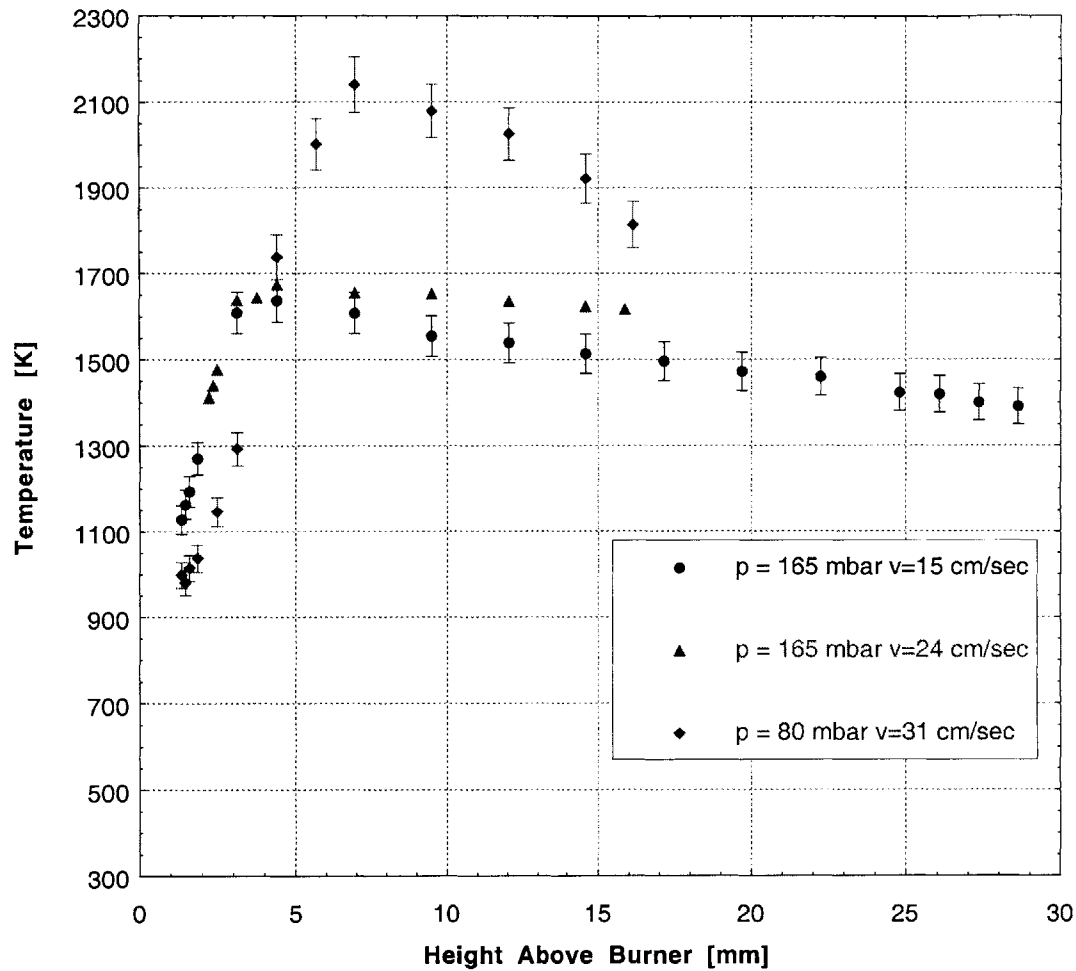
An image of a typical flame is included in Figure 6.7. The flames are observed to be very uniform in the radial direction, over the full range of normal operating conditions. No disturbances to the flame due to the drilled plate burner geometry are observed at pressures less than 500 millibar. In general, the flames consist of a blue-white narrow luminous zone followed by a much longer secondary blue-purple region, suggesting slow conversion of CO to CO<sub>2</sub> in the secondary zone.



**Figure 6.7.** Typical propane-air flame, at an equivalence ratio of 1.0, operating pressure of 70 millibar, and surface temperature of 60 °C. Horizontal line corresponds to burner surface at the flame center; large scale divisions correspond to 1 cm.

The gas flow rates available in the system allow flames to be produced with unburned gas velocities from 15 to 50 cm/s at normal operating pressures of 50 to 200 millibar. At lower flow rates, standoff distance is reduced and the flames are significantly quenched, losing up to 25% of their heat output to the plate, as measured by temperature rise of the coolant. At the highest achievable velocities, the flame quench rate is very low, and negligible coolant temperature rise is observed.

Temperature profiles for some typical propane-air flames are shown in Figure 6.8, at a range of pressures and unburned gas velocities. All the flames were stoichiometric; the differences in peak temperature are largely due to heat loss to the burner surface. The decreasing temperatures after the peak values are indicative of heat loss to the gases surrounding the flame.



**Figure 6.8.** Measured radiation-corrected temperature profiles for several stoichiometric propane-air flames, at differing chamber pressures and unburned gas velocities.

## 6.8. References

J.D. Bittner, S.M. Faist, J.B. Howard and J.P. Longwell, "Deposit Formation by Diffusion of Flame Intermediates to a Cold Surface," in L.B. Ebert, ed., Chemistry of Engine Combustion Chamber Deposits, Plenum Press, 227 - 243 (1985).

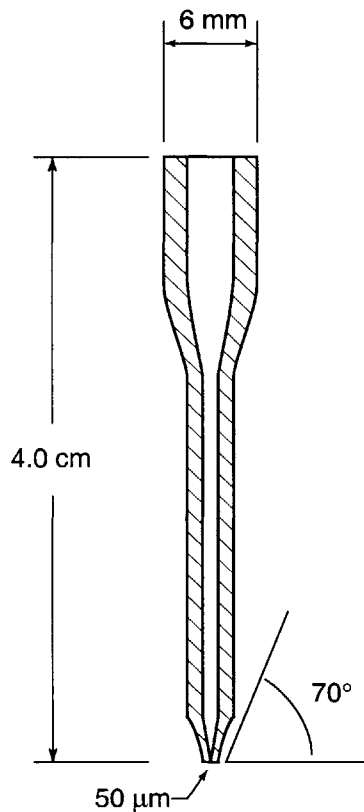
M.V. Heitor and A.L.N. Moreira, "Thermocouples and Sample Probes for Combustion Studies," *Progress in Energy and Combustion Science*, Vol. 19, 259-278 (1993).





**7.1 Gas Sampling Apparatus and Probe Sampling Considerations**

The gas sampling and analysis system is the key element for measuring the chemical species profiles in the flame quench layer, and is also one of the most important potential sources of error in the experiment. Direct sampling is used, in order to enable the use of high-resolution gas chromatography for measurement of the low-concentration deposit precursors, although sample probes invariably cause some degree of disturbance to the flame. The probe and sample train, described below, are designed to sample and quench gases from the flame with minimal disturbance to the flame structure, and to provide species identification and concentration measurements for major species such as propane, water, carbon monoxide and carbon dioxide (percent level concentrations), as well as for minor species such as toluene partial oxidation projects (ppm level concentrations).



**Figure 7.1** Quartz microprobe used for gas sampling. Probe diameter at the tip is less than 1 mm.

**7.2 Microprobe Sampling Apparatus**

Figure 7.1 shows the dimensions of the quartz microprobe. The 50 μm orifice produces choked flow into the sampler, providing constant sample mass flow rate independent of probe back pressure. The presence of the probe naturally causes some disturbance to the flame structure. The volume disturbed by the probe is roughly defined by a diameter  $D_T$ , given by

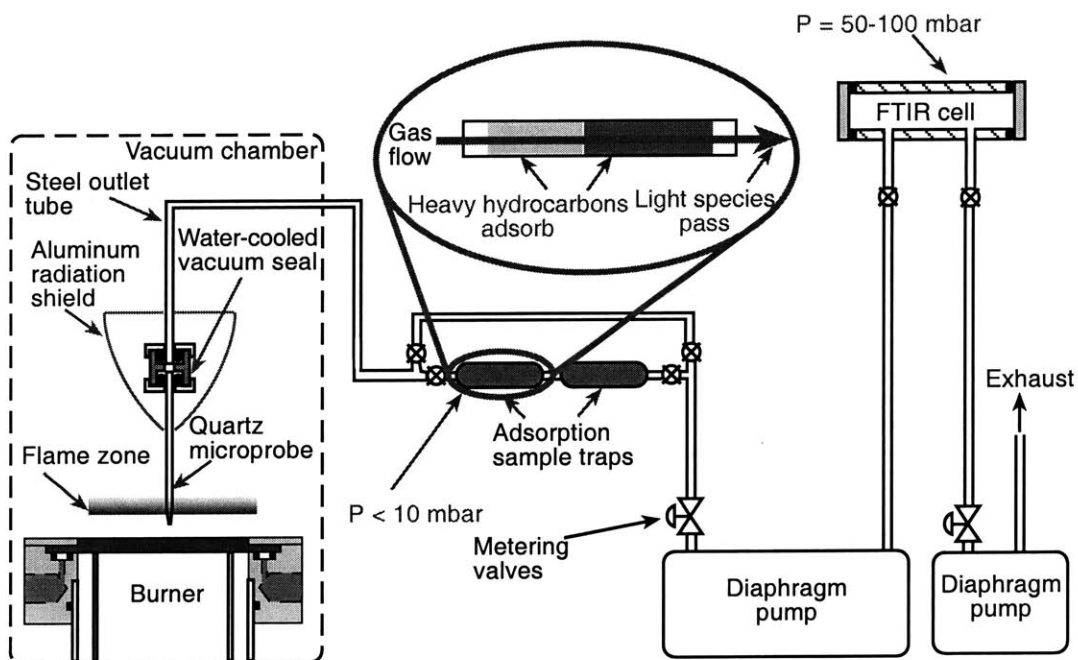
$$D_T = \sqrt{\frac{\pi \dot{m}}{4 \rho u}} \quad (7.1)$$

where  $\dot{m}$  is the mass flow rate through the probe, and  $\rho$  and  $u$  are the density and velocity of the gas stream at the measuring point (Heitor and Moreira, 1993). In this apparatus  $D_T$  is approximately 30 μm under most

conditions, which should cause minimal disturbance to the flame.

Figure 7.2 gives a schematic of the sampler as used in the vacuum chamber and the associated instrumentation. The microprobe is connected to a stainless steel outlet tube via a water-cooled fitting, through which the sampled gases are pumped out of the chamber by a multi-stage oil-free diaphragm pump. The pump allows for up to four different pressure regions in the sample train, thus allowing for multiple analytical stages. As shown in Figure 7.2, the sample may either be pumped directly into a Fourier-transform infrared spectroscopy (FTIR) cell for online analysis, or passed through a pair of hydrocarbon adsorption traps for storage and later gas chromatography / mass spectroscopy (GC/MS) analysis. Each of the analytical systems will be described in detail below. The sample pressure is maintained at less than 10 millibar at the probe inlet, between 50 and 100 millibar in the infrared gas cell, and between 10 and 20 millibar in the adsorption traps.

The two major considerations for sampler performance are the quench rate at the probe tip and the time required to take a sample. The mass flow rate through the probe is important to both these parameters. Since the flow at the probe tip is choked, the mass flow rate through the sample train is determined by the pressure and temperature in the burner chamber at the sampling



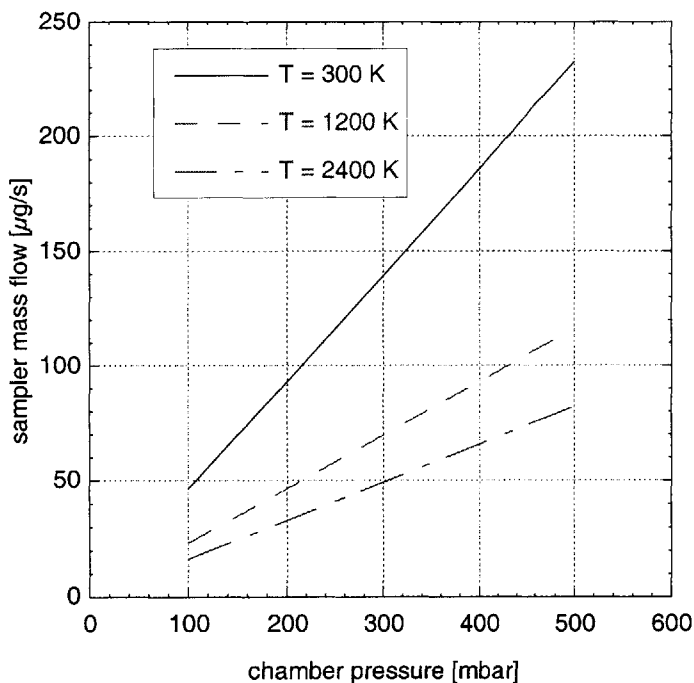
**Figure 7.2** Schematic diagram of the quartz microprobe sampler system and associated sample train with infrared spectroscopy cell and hydrocarbon adsorption traps for gas chromatography sample storage.

point. A plot of sample mass flow versus chamber pressure for several temperatures is shown in Figure 7.3.

The quench rate is controlled primarily by the probe backpressure, which determines the amount of expansion cooling the gas undergoes upon entering the probe. The factor by which an Arrhenius-type reaction rate is reduced by quenching is given by:

$$\frac{k_q}{k} \approx e^{\left(\frac{T_a}{T} - \frac{T_a}{T_q}\right)} \quad (7.1)$$

where  $k$  and  $T$  are the pre-quenching reaction rate and sample temperature,  $k_q$  and  $T_q$  are the quenched rate and temperature, and  $T_a$  is the activation energy of the reaction expressed in

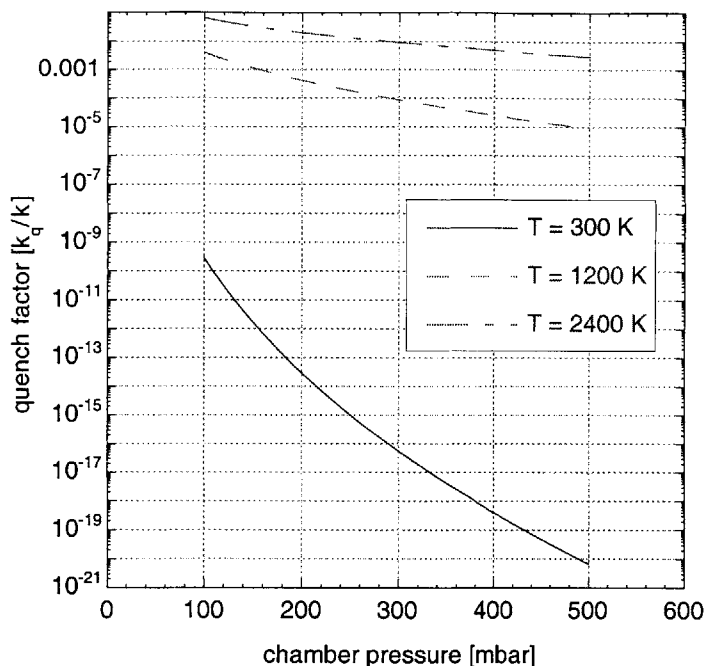


**Figure 7.3** Mass flow through the sampling system as a function of pressure and temperature at the probe tip.

with chamber pressure for the same sample temperatures used in Figure 7.3, assuming a reaction activation energy of 5000 K. This activation energy (approximately 40 kJ/mol) is much lower than most flame reaction activation energies, with the exception of radical reactions. Those reactions with higher activation energies will be quenched exponentially faster.

Kelvin. This quenching will occur over the time that the gas is expanding in the sampler tip, which is on the order of milliseconds under the conditions shown in Figure 7.2. Like the mass flow rate, the quenching factor is also dependent on pressure and temperature at the sampling point.

Figure 7.4 shows the variation of quenching



**Figure 7.4** Reaction quenching as a function of pressure and temperature at the probe tip.

the sampling time for infrared spectroscopy is approximately 5 to 15 minutes, and the required sampling time for gas chromatography is five to twenty minutes, depending on temperature conditions at the sampling point and concentrations of the species to be measured.

### 7.3 FT-IR Analysis of Major Species Concentrations

Major species concentration measurements are made via Fourier transform infrared spectroscopy (see Figure 4.2 above). The apparatus consists of a Nicolet Magna-IR 550 spectrometer, using a liquid nitrogen cooled MCT-A photodetector. The sample gases are pumped directly through a single-pass cylindrical cell, 10 centimeters in length and 2 centimeters in diameter, with calcium fluoride windows, which is mounted between two stages of the sampling pump. Sample cell pressure is measured via a Omega Engineering PX177 pressure transducer. The spectrometer records the infrared absorption spectrum of the sample, over a frequency range from 800  $\text{cm}^{-1}$  to 7000  $\text{cm}^{-1}$ . Each species in the sample (apart from the homonuclear diatomics  $\text{H}_2$ ,  $\text{O}_2$  and  $\text{N}_2$ ) absorbs the infrared light in a distinct pattern, allowing both identification and quantification for species with large enough concentrations in the sample.

The sample collection time can be estimated as the total amount of mass in the sample train divided by the mass flow rate through the probe tip. Hence, to minimize sampling times, it is necessary to keep the gas pressures in the various sections of the sample train as low as is practical.

Given the pressures indicated in Figure 7.2 and a chamber pressure of 150-200 millibar,

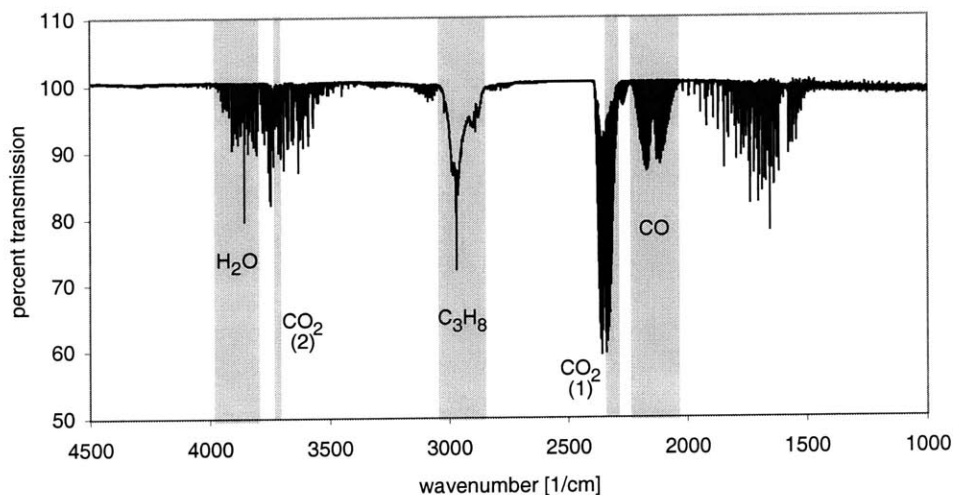
The lower detection limit of the system corresponds to roughly one to two millibar partial pressure of a species.

To construct a calibration curve for each species, the sample cell was filled to a known pressure with a gas mixture containing a known concentration of the species and a spectrum was recorded. This process was then repeated for a number of different total pressures, resulting in a range of partial pressures for each calibrated molecule. Water was calibrated via a different method; the sample cell was filled with ambient air of known relative humidity to provide a reference partial pressure. This results in a somewhat lower calibration accuracy for water than for the other measured species.

The second step of FT-IR calibration involves the selection of an appropriate spectral range or ranges to calibrate for each species. The two criteria used to select a spectral range are:

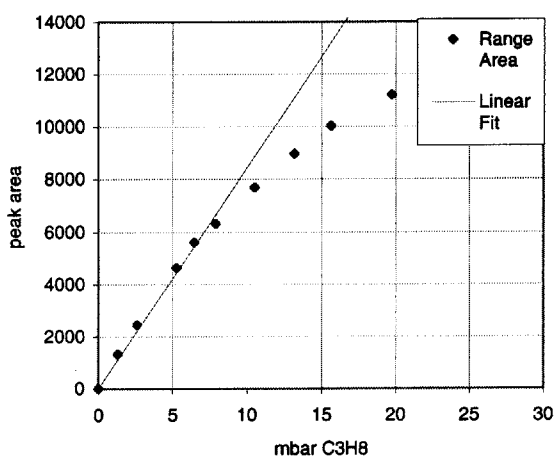
- 1 The region should be free from interfering absorptions due to other compounds that are likely to be present in the flame
- 2 The peak area should have a linear relation to the species partial pressure over the range of interest (i.e. no saturation). For species that have a wide range of concentration values in the flame, more than one spectral region may be necessary to obtain accurate concentration values under all conditions.

A typical infrared spectrum of a flame gas sample is shown in Figure 7.5, with the selected

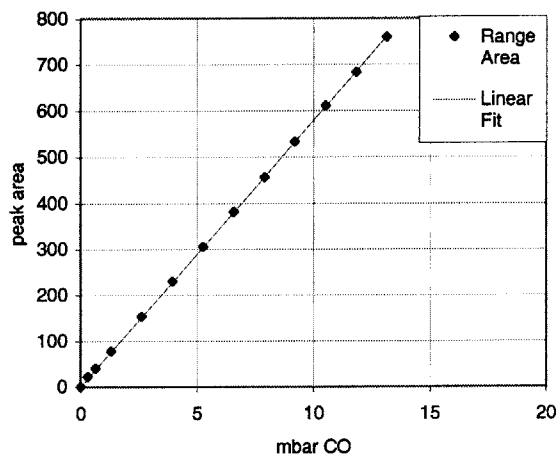


**Figure 7.5.** A typical FTIR spectrum of a sample taken from the flame zone, showing the calibration regions for major species.

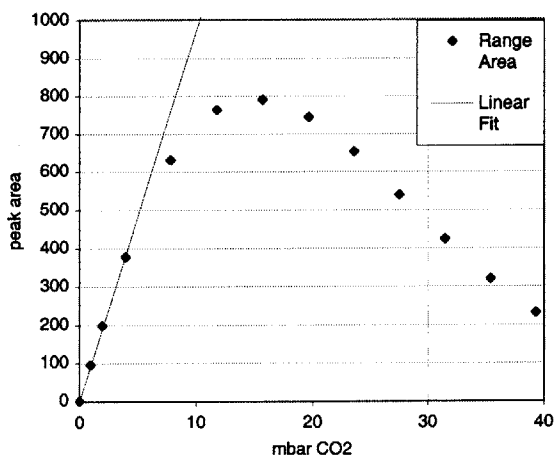
calibration spectral ranges for various species indicated. Two ranges are shown for  $\text{CO}_2$ , since the  $2322\text{-}2348\text{ cm}^{-1}$  range begins to saturate as  $\text{CO}_2$  partial pressure in the sample cell increases above 6 mbar; hence the  $3695\text{-}3700\text{ cm}^{-1}$  range, which is too weak to be used at lower  $P_{\text{CO}_2}$  values, is used for higher concentrations (see Figures 7.8 and 7.9). Calibration curves for the major species  $\text{C}_3\text{H}_8$ ,  $\text{CO}$ , and  $\text{CO}_2$  are shown in Figures 7.6 to 7.9.



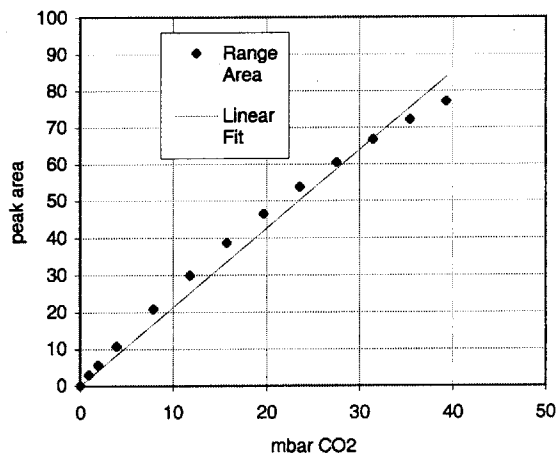
**Figure 7.6.** Calibration curve and linear fit for propane in the  $2809\text{-}3040\text{ cm}^{-1}$  range



**Figure 7.7.** Calibration curve and linear fit for carbon monoxide in the  $2071\text{-}2141\text{ cm}^{-1}$  range



**Figure 7.8.** Calibration curve and linear fit for carbon dioxide in the  $2322\text{-}2348\text{ cm}^{-1}$  range



**Figure 7.9.** Calibration curve and linear fit for carbon dioxide in the  $3695\text{-}3700\text{ cm}^{-1}$  range

The major chemical species that are not measured with this system are oxygen, nitrogen and hydrogen. However, their concentrations can be estimated at each measured point via mass (or atom) conservation relations. Mole fractions of the three species are given by the following:

$$X_{O_2} = \frac{5}{3\phi} \left( \sum_i v_{C,i} X_i + \sum_j v_{C,j} X_j \right) - \frac{1}{2} \left( \sum_i v_{O,i} X_i + \sum_j v_{O,j} X_j \right) \quad (7.2)$$

$$X_{H_2} = \frac{4}{3} \left( \sum_i v_{C,i} X_i + \sum_j v_{C,j} X_j \right) - \frac{1}{2} \left( \sum_i v_{H,i} X_i + \sum_j v_{H,j} X_j \right) \quad (7.3)$$

$$X_{N_2} = \frac{6.27}{\phi} \left( \sum_i v_{C,i} X_i + \sum_j v_{C,j} X_j \right) - \frac{1}{2} \sum_j v_{N,j} X_j \quad (7.4)$$

where  $v_{A,n}$  is the number of atoms of element  $A$  in species  $n$ ,  $X_i$  are the mole fractions of the measured species, and  $X_j$  are the mole fractions of all unmeasured species *except*  $O_2$ ,  $N_2$ , and  $H_2$ . For use of these mass balances to be practical, all the sums over the unmeasured species must be negligible compared to the sums over measured species (see the error analysis below for more on this assumption). In addition, this analysis presumes that the effects of differential diffusion are negligible; errors due to this assumption would be most noticeable in the calculated hydrogen concentration values, due to its high diffusivity (Pope *et al.*, 1999).

The mole fractions of the measured species are calculated from the FTIR spectrum taken at any given point by the following method. The integrated area of the spectrum in each of the calibrated ranges is calculated. To determine the partial pressure of a particular species, linear interpolation along the calibration curve is used if the area falls within the calibrated range. If the area is lower than any calibration point, a least-squares fit to the lowest few points on the calibration curve with the intercept constrained to zero is used to determine the corresponding partial pressure. The mole fraction of the species is then determined by the species partial pressure divided by the total pressure in the FTIR cell at the time of measurement.

#### 7.4 Thermal Absorption / Desorption Sampling and GC/MS Analysis for Minor Species Identification and Quantification

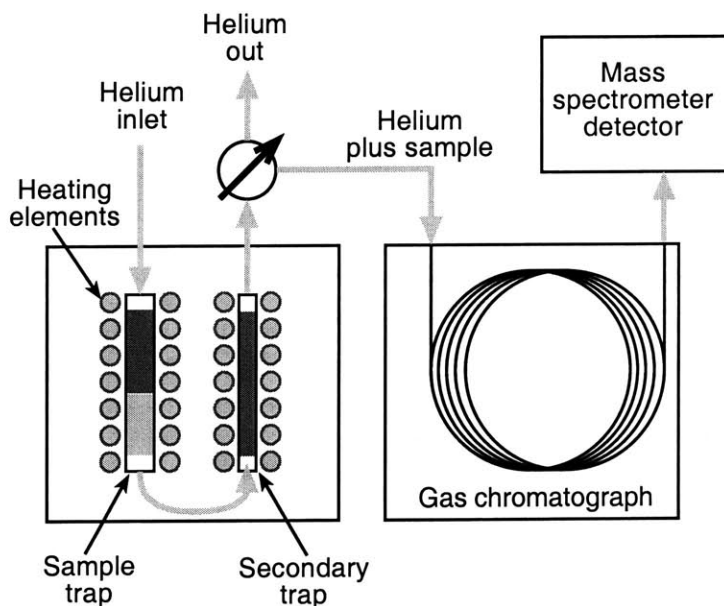
The above method is suited only for measurement of major species concentrations; to determine the concentration profiles of the minor species in the flame such as toluene and its derivatives, a gas chromatography - mass spectroscopy method is used.

Samples for GC/MS analysis are collected using hydrocarbon absorption traps, as shown in Figure 7.2. The traps consist of stainless steel tubes packed with a absorbing matrix similar to

that found in a gas chromatography column. The particular absorber used for this work (Tenax™ TA) was chosen for strong absorption of hydrocarbon species with three or more carbons, and for low sensitivity to water. The gas flow from the sampling probe is directed through the trap for approximately five minutes to collect a single sample at levels adequate to detect species at concentrations greater than 10 ppm; additional sampling time will allow for resolution of species at lower concentrations, at the risk of saturating the higher concentration species. Two traps are used in series; if the first trap becomes saturated, the escaping hydrocarbons will be captured by the second trap. Only cases in which no saturation is observed are used for concentration measurements of a given species.

The GC/MS analysis apparatus is shown in Figure 7.10. A thermal desorber with a secondary trap (Perkin-Elmer ATD400) is used to inject the sample onto the GC column. The secondary trap is contained in a Peltier effect heating element, which allows a two-stage injection process. In the first stage, the primary (sample) trap is heated to approximately 350°C, while a helium flow is directed through the primary trap to the secondary trap, which is maintained at 10°C. This continues for approximately five minutes, so that all the sample from the primary trap is transferred to the

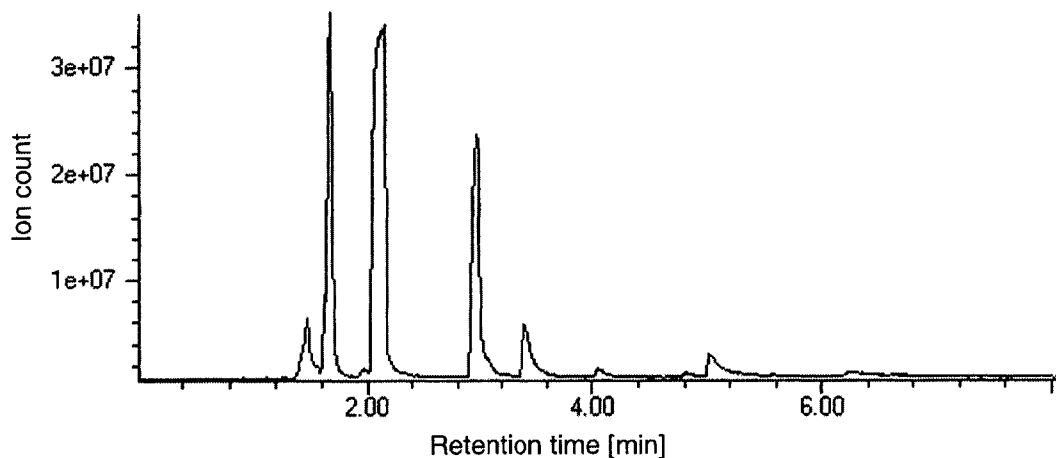
secondary trap. After sufficient time for desorption, the secondary trap is connected to the GC inlet and rapidly heated to 400°C. This process releases the sample hydrocarbons onto the GC column in a short pulse, which produces sharper, more easily identifiable peaks in the chromatogram.



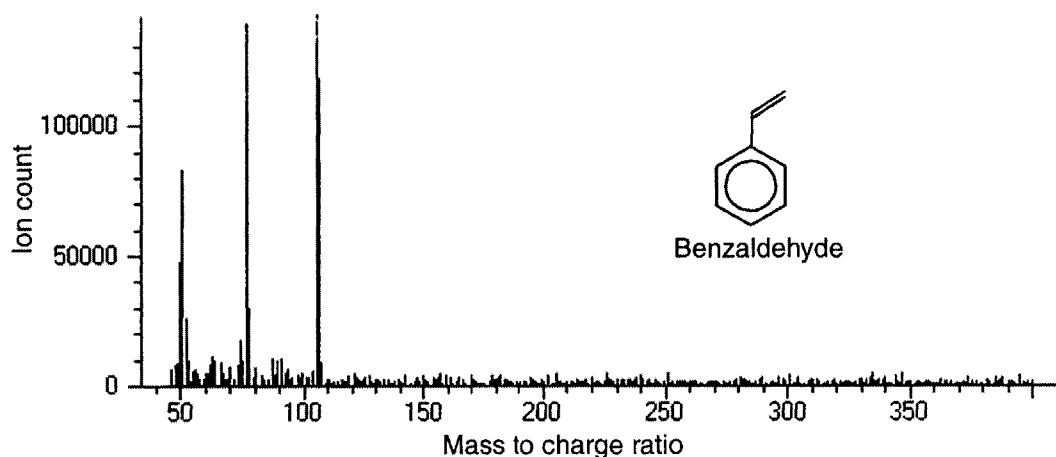
**Figure 7.10** Schematic diagram of the thermal desorber and gas chromatograph system with mass spectrometer detector. The sample is first transferred from the (heated) sample trap to the (cooled) secondary trap; the secondary trap is then connected to the gas chromatograph and rapidly heated, injecting the sample onto the column.



The gas chromatograph used is an HP 5980 GC with a DB-1 column, 30 meters in length and 0.5 mm in diameter. A mass spectrometer acts as the detector. The column retains and separates the various species in the sample, and the mass spectrum of each eluted peak can be used to identify the compound, via matching with a library of reference mass spectra. A typical chromatogram and mass spectrum from a toluene-doped propane flame are shown in Figures 7.11 and 7.12.



**Figure 7.11** Typical chromatogram from a flame with fuel composition of 95% propane, 5% toluene (molar basis). Oven temperature is maintained at 50 °C for the first ten minutes, and then ramped up at 8 °C per minute to 300 °C.



**Figure 7.12** Sample mass spectrum from the chromatogram shown in Figure 7.11. Spectrum corresponds to a retention time of 5.2 minutes; the species is identified as benzaldehyde ( $C_6H_5CHO$ , structure shown above).

Quantification of the species observed in the chromatograms is based on the integrated area of the peaks. The total mass of sample passed through each absorption trap is used to normalize the chromatograms with respect to each other, and the known toluene inlet concentration is used to relate the normalized areas to gas-phase species concentrations in the flame.

### 7.5 Error Analysis of Species Concentration Measurements

There are a number of uncertainties in the measurements that go into producing a set of flame concentration profiles. This section outlines the sensitivity of each of the output values (i.e. the mole fraction profile of each species and the overall equivalence ratio) to each of the sources of uncertainty in the measurements, and shows how these relate to errors in the final flame profile.

Table 7.1 lists the errors associated with each instrument, their sources and relative magnitudes. The error in the minor species measurements depends almost entirely on the sample mass flow rate; hence the overall error in these measurements is approximately  $\pm 5$  percent.

Instrument	Error Sources	Error Magnitude
Sample Mass Flow	Pressure, temperature measurements at probe inlet	$\pm 5\%$ of calculated mass flow rate (note: smaller at lower sample temperatures)
Mass flow meters	Nonlinearity, zero drift	$\pm 0.5\%$ of full scale reading
Pressure transducers / transmitters	Nonlinearity, hysteresis, zero drift, calibration errors	$\pm 0.5\%$ of full scale reading (approximately 5 millibar)
Thermocouples	Reference point drift, meter inaccuracy	$\pm 0.1$ K
FTIR spectrometer	Poorly resolved peaks, saturation, calibration errors	Negligible (except H <sub>2</sub> O calibration: $\pm 5$ to 10%)
GC / MS system	Poor separation of peaks, flow measurement errors	Negligible

**Table 7.1.** Gas sampling and analysis error sources and magnitudes

The major species measurements have significantly more sources of error, especially those that are based on mass balances. Given the information in Table 7.1, the spectrometer error itself will be neglected in this analysis, since the error introduced by measurement of the pressure in the sample cell will be much more significant. It should be noted that 5 millibar is the *maximum* error of the pressure readings, since zero drift can be essentially eliminated via frequent recalibration of the sensors.

The relations between these error sources and the “measured values” of species mole fractions and equivalence ratio are given by the equations below:

$$\frac{\varepsilon(X_i)}{X_i} \approx \frac{\varepsilon(P)}{P} \quad (7.5)$$

$$\frac{\varepsilon(\phi)}{\phi} \approx \left(1 + \frac{\varepsilon(P)}{P}\right)^2 \left(1 + \frac{\varepsilon(\dot{V}_f)}{\dot{V}_f}\right) \left(1 + \frac{\varepsilon(\dot{V}_a)}{\dot{V}_a}\right) - 1 \approx 2 \frac{\varepsilon(P)}{P} + \frac{\varepsilon(\dot{V}_f)}{\dot{V}_f} + \frac{\varepsilon(\dot{V}_a)}{\dot{V}_a} \quad (7.6)$$

where  $\varepsilon(A)$  represents the error in measurement of value  $A$ .

To determine the error in all of the output values, including those mole fractions that are found by mass balances, we need to include the uncertainties introduced by unmeasured species and by the error in equivalence ratio. The relation of the errors in the complete set of output mole fractions to all of these error sources is shown in the following matrix (unmeasured nitrogen containing species have been neglected):

$$\begin{bmatrix} \varepsilon(X_i) \\ \varepsilon(X_{N_2}) \\ \varepsilon(X_{H_2}) \\ \varepsilon(X_{O_2}) \end{bmatrix} = \begin{bmatrix} \frac{6.27}{\phi} v_{C,i} & 0 & \frac{6.27}{\phi} & 0 & 0 \\ \frac{4}{3} v_{C,i} - \frac{1}{2} v_{H,i} & -6.27 \sum_i v_{C,i} X_i & \frac{4}{3} & -\frac{1}{2} & 0 \\ \frac{5}{3\phi} v_{C,i} - \frac{1}{2} v_{O,i} & 0 & \frac{5}{3\phi} & 0 & -\frac{1}{2} \\ -\frac{5}{3} \sum_i v_{C,i} X_i & 0 & \frac{5}{3\phi} & 0 & -\frac{1}{2} \end{bmatrix} \begin{bmatrix} \varepsilon(X_i) \\ \varepsilon(\phi) \\ \sum_j v_{C,j} X_j \\ \sum_j v_{H,j} X_j \\ \sum_j v_{O,j} X_j \end{bmatrix} \quad (7.7)$$

In the above,  $\varepsilon(A)$  is assumed to be small relative to the value of  $A$ , to allow for linearization.

Several insights into the relative importance of different error sources can be gained by examination of this matrix. It is interesting to note that while error in the propane measurement makes a significant contribution to errors in the calculated values of  $O_2$  and  $N_2$ , it has almost *no* impact on the error in  $H_2$  (since  $4/3*(3) - 1/2*(8) = 0$ ). Also, as should be expected, unmeasured carbon has a large effect on the mass balance concentrations; thus species such as aromatics with

high carbon content can contribute significantly to errors even if their mole fractions are relatively small. In order to find the most important error contributions under normal conditions, we can assume that  $\phi \approx 1$  and  $\sum_i v_{C,i} X_i \approx 0.12$ , which are appropriate values for a near-stoichiometric flame. Using these numbers, and the stoichiometry of the four measured species ( $C_3H_8$ , CO, CO<sub>2</sub>, and H<sub>2</sub>O), we find that the contribution of equivalence ratio errors is much the least significant of any of the error sources, while errors that relate to measurement of total carbon are most important. Water turns out to have the least impact of all the measured species on the mass balance results, which compensates to some degree for its greater calibration uncertainty.

## 7.6 References

- M.V. Heitor and A.L.N. Moreira, "Thermocouples and Sample Probes for Combustion Studies," *Progress in Energy and Combustion Science*, Vol. 19, 259 - 278 (1993).
- C.J. Pope, R.A. Shandross, and J.B. Howard, "Variation of Equivalence Ratio and Element Ratios with Distance from Burner in Premixed One-Dimensional Flames," *Combustion and Flame*, Vol. 116, 605 - 614 (1999).

### 8.1 Objectives of Validation Experiments

The set of experiments described below was performed in order to validate the performance of the flat flame burner and diagnostic systems described in Chapters 6 and 7. Undoped propane-air flames were observed at several equivalence ratios; these flames are fairly well understood and may be modeled with existing chemical mechanisms, and hence provide a useful means of benchmarking the sampling and analysis system.

Several aspects of the experimental apparatus were examined via the collection and analysis of these flame profiles. The spatial resolution and reaction quenching of the sample probe can be qualitatively demonstrated by the resolution of sharp concentration peaks in the flame, which will tend to be broadened if the probe samples from too large a volume of gas in the flame or if reactions can continue inside the probe. The axial positioner repeatability and radial uniformity of the flame can be tested by taking samples in random order and by comparing samples taken with the probe located at different radial positions. Adsorption or “memory” effects in the sample system are of critical importance, particularly for the low concentration, low volatility deposit precursor species we wish to observe; this issue is also addressed with these experiments. The performance of the gas sampling and analysis system is also discussed in this chapter in more quantitative terms, via comparison of the experimental measurements to calculated results using established propane oxidation models.

### 8.2 Experimental Method

Three propane-air flames were examined, at equivalence ratios of  $\phi = 0.9$ ,  $\phi = 1.0$  and  $\phi = 1.2$ . The flow rate and pressure characteristics of these flames are listed in Table 8.1. The burner surface temperature in all three cases was maintained at  $70 \pm 5$  °C. The flames were operated with no gas flow through the outer ring section of the burner, since the presence or absence of this flow was not observed to have any impact on the central region of the flames where samples were collected.

Equivalence Ratio	Pressure [mbar]	Fuel Flow Rate [mg/sec]	Air Flow Rate [mg/sec]	Unburned Gas Velocity [cm/sec]
$0.90 \pm 0.01$	$165 \pm 5$	$8.9 \pm 0.1$	$154 \pm 2$	$15.0 \pm 0.2$
$1.00 \pm 0.01$	$165 \pm 5$	$9.9 \pm 0.1$	$154 \pm 2$	$15.1 \pm 0.2$
$1.20 \pm 0.01$	$165 \pm 5$	$11.9 \pm 0.1$	$154 \pm 2$	$15.2 \pm 0.2$

**Table 8.1.** Flame characteristics for propane-air flame validation experiments.

FT-IR sampling was performed with all three flames, to observe profiles of major species in the axial direction. For the  $\phi = 1.0$  flame, the gas samples were taken in a random axial order. The samples for this flame were taken in two sessions, over two days. For the second data set, the sampling probe was offset by approximately 1.5 mm radially from its original position, in order to check for radial nonuniformities in the flame. The infrared samples were taken at pressures of 70 to 80 millibar in the sample cell. The cell was evacuated to a pressure of less than 1 millibar and a background absorption reference spectrum was recorded before each sample was collected. The time required to build up sufficient pressures of sample gas in the cell varied from ten to fifteen minutes, depending on the gas temperature at the probe tip.

Adsorption trap samples were also taken for the  $\phi = 1.2$  flame, from very near the burner surface to slightly past the region of peak luminosity. Samples were collected by directing the sample gas flow through a set of traps for twenty minutes. Several tests were performed to examine for potential retention of species via adsorption within the sampling train, which are discussed in detail in the following section.

Temperatures were measured for all three flames after the gas samples were taken, using the dual-thermocouple method discussed in Chapter 6. The temperature measurements were also recorded in random axial ordering.

### 8.3 Minor Species Storage Effects in the Sampling System

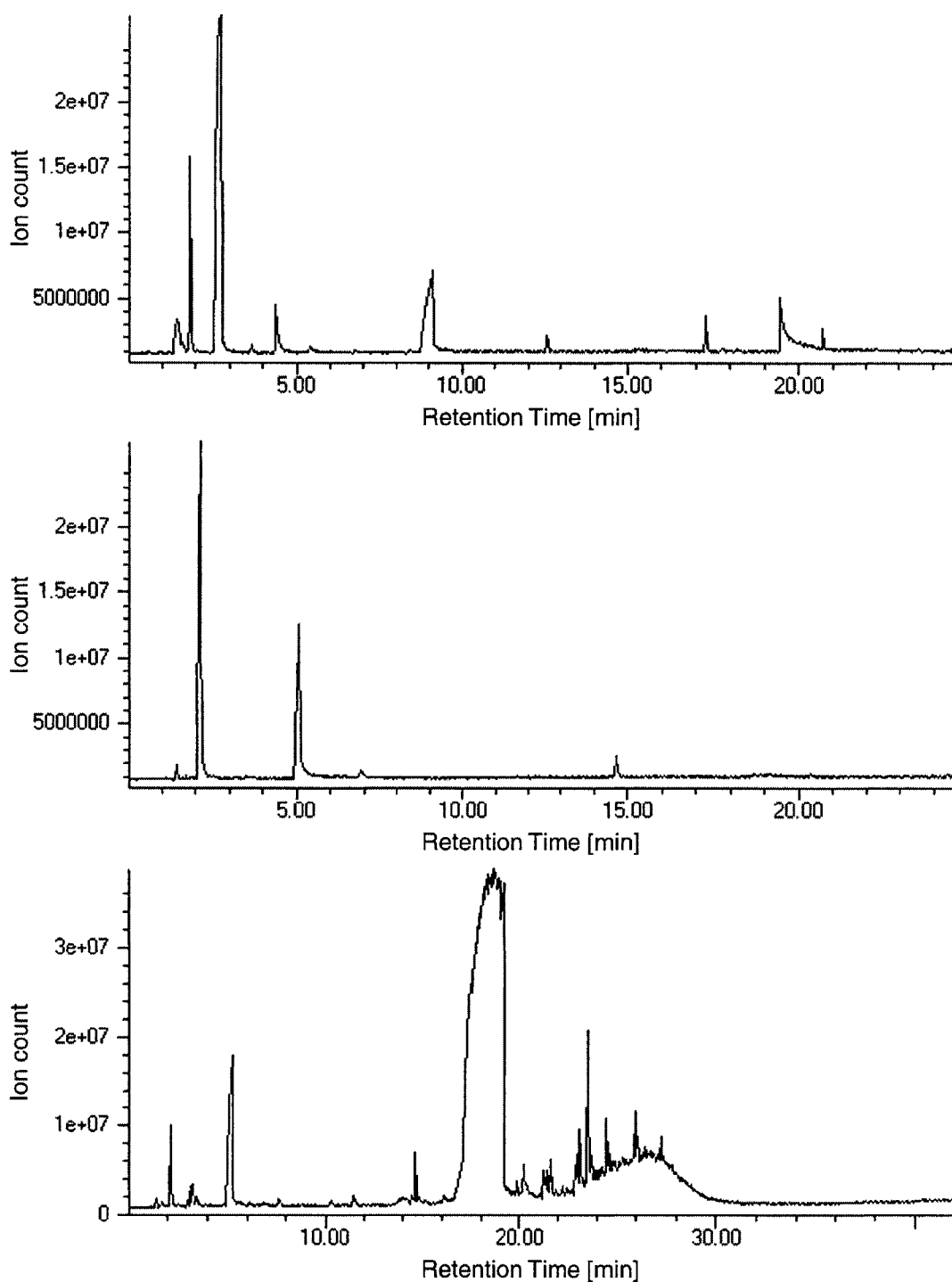
As mentioned above, it is especially important to eliminate any adsorption or storage of species in the sampling system, since any crossover from one sample to the next will cause errors in the measured concentration profiles. This was not a concern for the FT-IR samples, as the

sample cell was evacuated before each sample, and the recorded background spectra showed no absorption from hydrocarbons (carbon dioxide and water were present only at ambient background levels). However, the GC/MS analysis system is designed to observe small concentrations of heavy hydrocarbons, and can easily be affected by very small amounts of hydrocarbon adsorption or absorption in the sample train.

To observe the sample retention effect, the following procedure was used: adsorption trap samples were taken from the pre-flame zone of a propane-air flame at  $\phi = 1.25$ , with a total sampling time of approximately one hour, in order to flow a significant amount of heavier hydrocarbons through the collection system. Immediately after this, the flame equivalence ratio was adjusted to  $\phi = 0.9$ , and samples were taken downstream of the flame, where hydrocarbon concentrations should be minimized. A third set of samples was then taken with fresh air (no fuel) flowing through the burner.

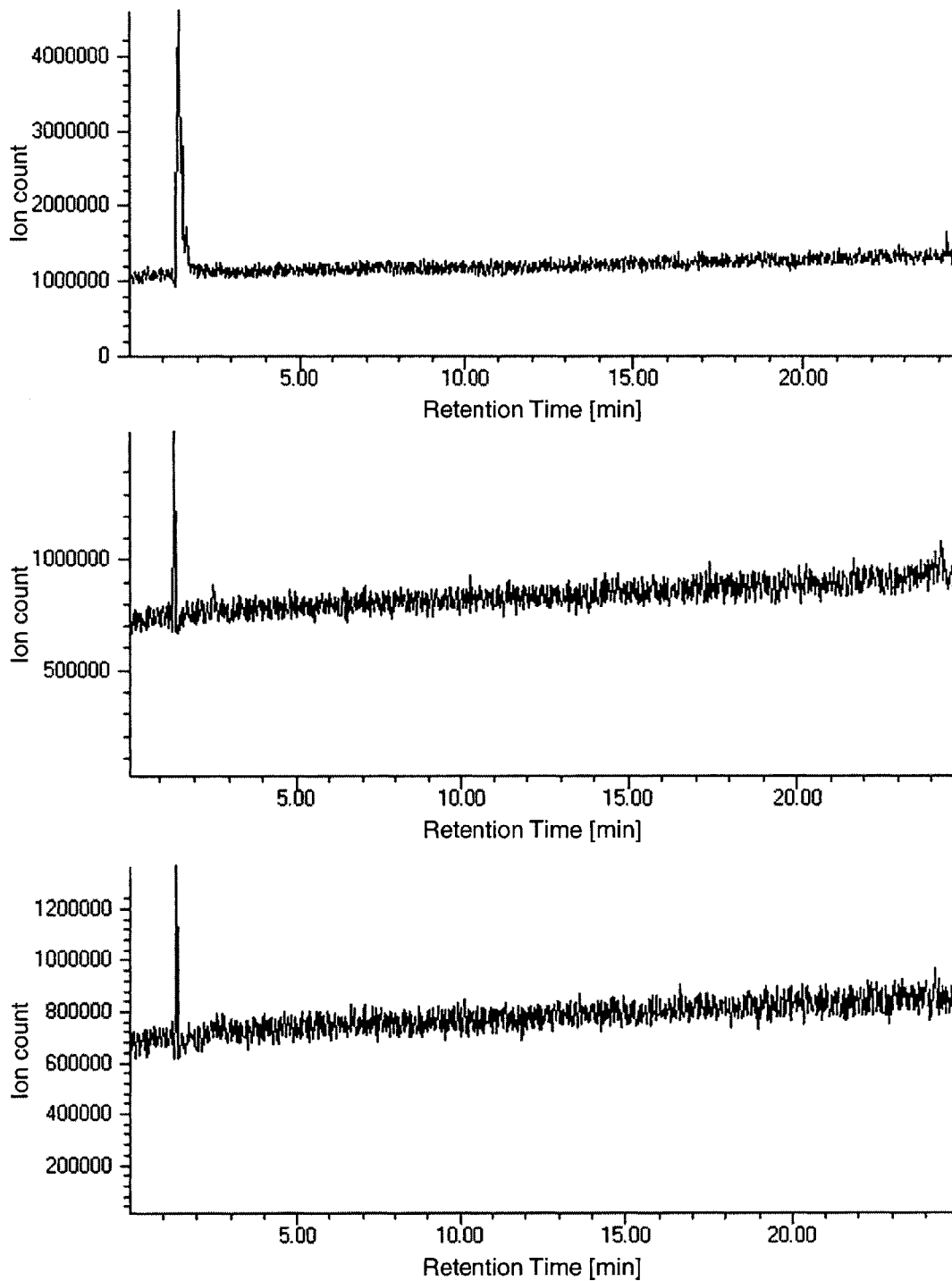
In the initial configuration of the sample train, in which the adsorption traps were placed after the infrared cell, significant holdover of hydrocarbons was observed, as seen in the chromatograms shown in Figure 8.1. The observed hydrocarbon peaks did not decrease significantly with time, even when flushing fresh air through the sample system repeatedly.

In order to eliminate this effect, the adsorption traps were moved upstream of the diaphragm pump. A similar set of tests, shown in Figure 8.2, gave no evidence of hydrocarbon retention in the sample train for this configuration. This is the configuration that was used for all GC/MS samples presented in this and the following chapters. For all flames in which adsorption trap samples were taken, a fresh air sample was collected after the flame samples to confirm that no hydrocarbon storage had taken place.



**Figure 8.1.** Evidence of hydrocarbon retention in the GC/MS sampling system (initial configuration). The first chromatogram is of samples taken in the pre-flame zone of a rich flame ( $\phi = 1.25$ ); the second is from the product region of a lean flame ( $\phi = 0.9$ ), taken after the first sample; the third is a sample of air only, taken immediately following the second sample. Each peak in the chromatograms represents a hydrocarbon species. The significantly larger peaks in the third chromatogram are due to a much larger mass flow rate of air through the sample traps.





**Figure 8.2.** Elimination of hydrocarbon retention in the GC/MS sampling system. These chromatograms are from the same set of tests as Figure 8.1; the sampling configuration was altered to place the adsorption traps upstream of the sampling pump. The differences suggest that almost all the peaks in the chromatograms shown in Figure 8.1 were due to species adsorbed within the sample pump system from previous samples.

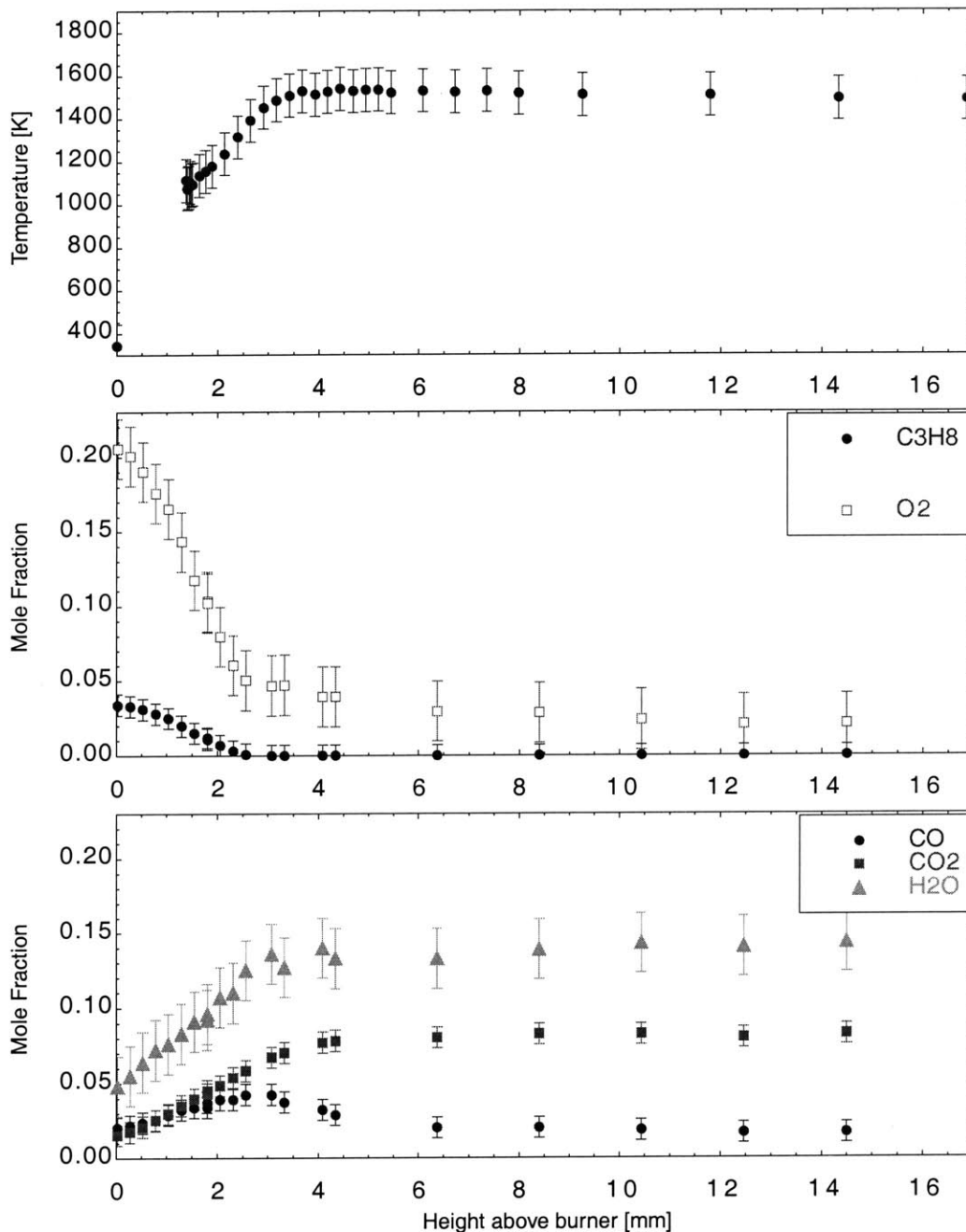
#### 8.4 Observed Species and Temperature Profiles in Propane-Air Flames

Figures 8.3 through 8.5 show the observed major species mole fraction and temperature profiles for the flames at  $\phi = 0.9$ ,  $\phi = 1.0$ , and  $\phi = 1.2$ , respectively. Mole fractions of  $O_2$  and  $H_2$ , as obtained by mass balances, are also included in these figures. The mass balance concentrations are indicated by open symbols; direct measurements are shown with filled symbols.

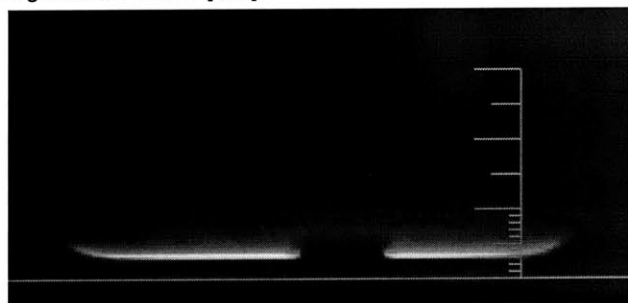
Figure 8.6 shows the results of the GC/MS sampling on the  $\phi = 1.2$  flame. Only two peaks were observed in the chromatograms; the first was the merged peaks due to small partially unsaturated hydrocarbons ( $C_4$  through  $C_6$ ), and the second corresponded to benzene. The unresolved hydrocarbon peak could be separated via the use of a dual-column method; this was not possible on the available equipment, which was optimized for aromatics and heavier hydrocarbons. Resolution and identification of these species could be achieved in future work with the appropriate modifications to the chromatography system. The concentration profiles measured via these peaks in the flame quench zone are shown in the figure.

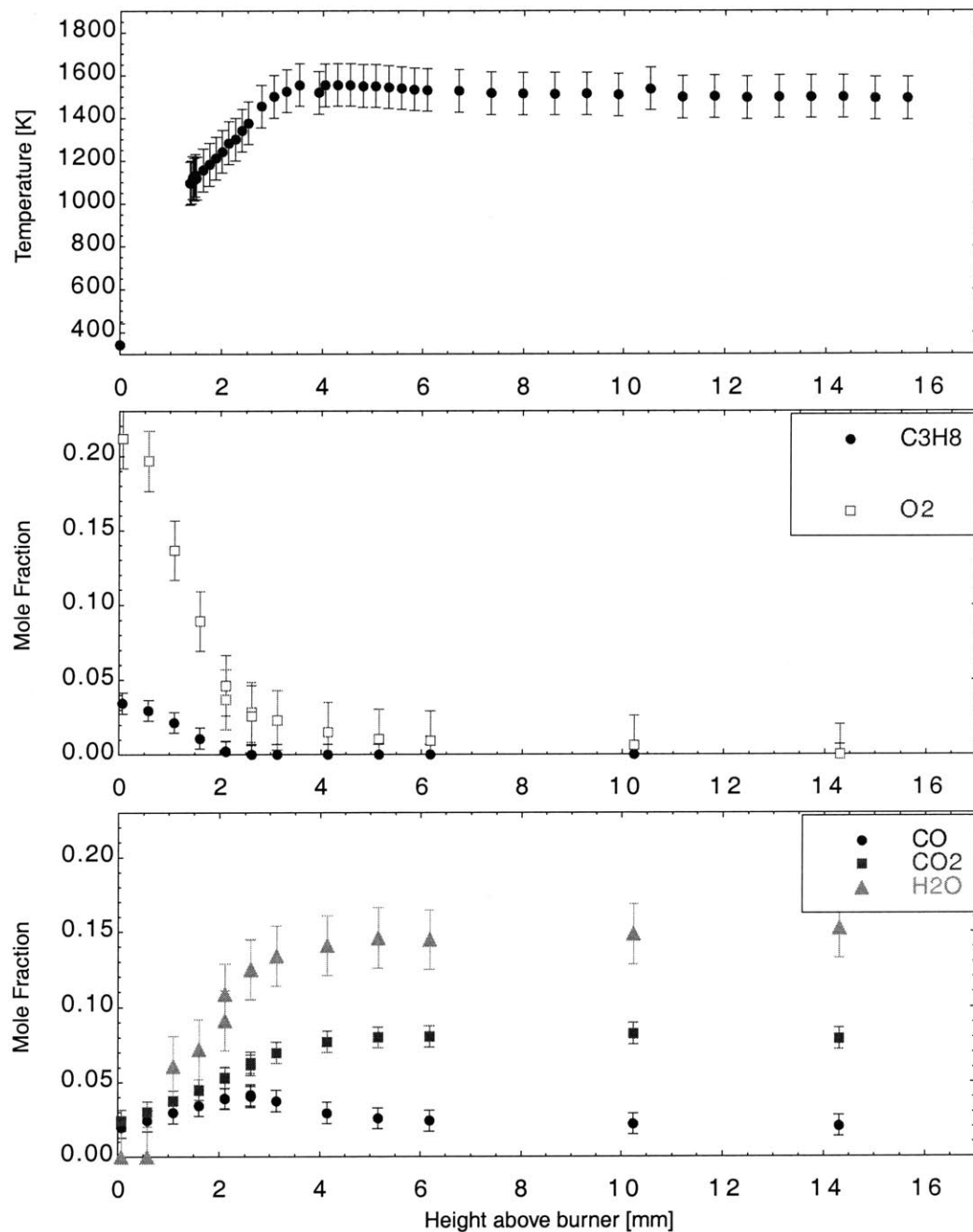
Several of the sampling issues discussed above can be addressed by inspection of these profiles. The random sampling order is not evident in the plots, which show relatively smooth profiles with minimal scatter. This illustrates both that there is no retention of species in the sample cell (which was also directly confirmed by the background spectra), and also that the positioner repeatability is adequate. The repeatability of the axial positioning is particularly demonstrated in Figure 8.3, which shows the  $\phi = 1.0$  flame that was recorded over two days. There is no noticeable offset between the two sets of points. Also, no effect of the different radial positioning of the sample probe in the two runs is observed.

The spatial resolution and quenching of the sampler are evidenced by its ability to resolve sharp peaks in the concentration profiles, as shown by flame intermediate species such as carbon monoxide (Figures 8.3 through 8.5) and benzene (Figure 8.6). The observation of benzene in the

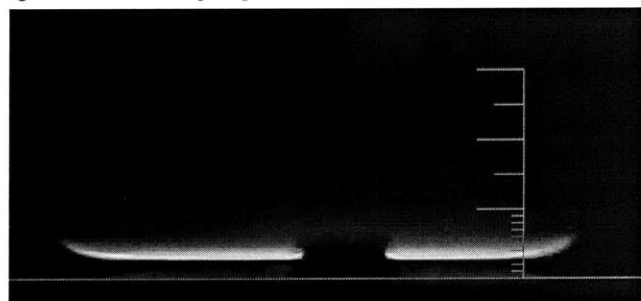


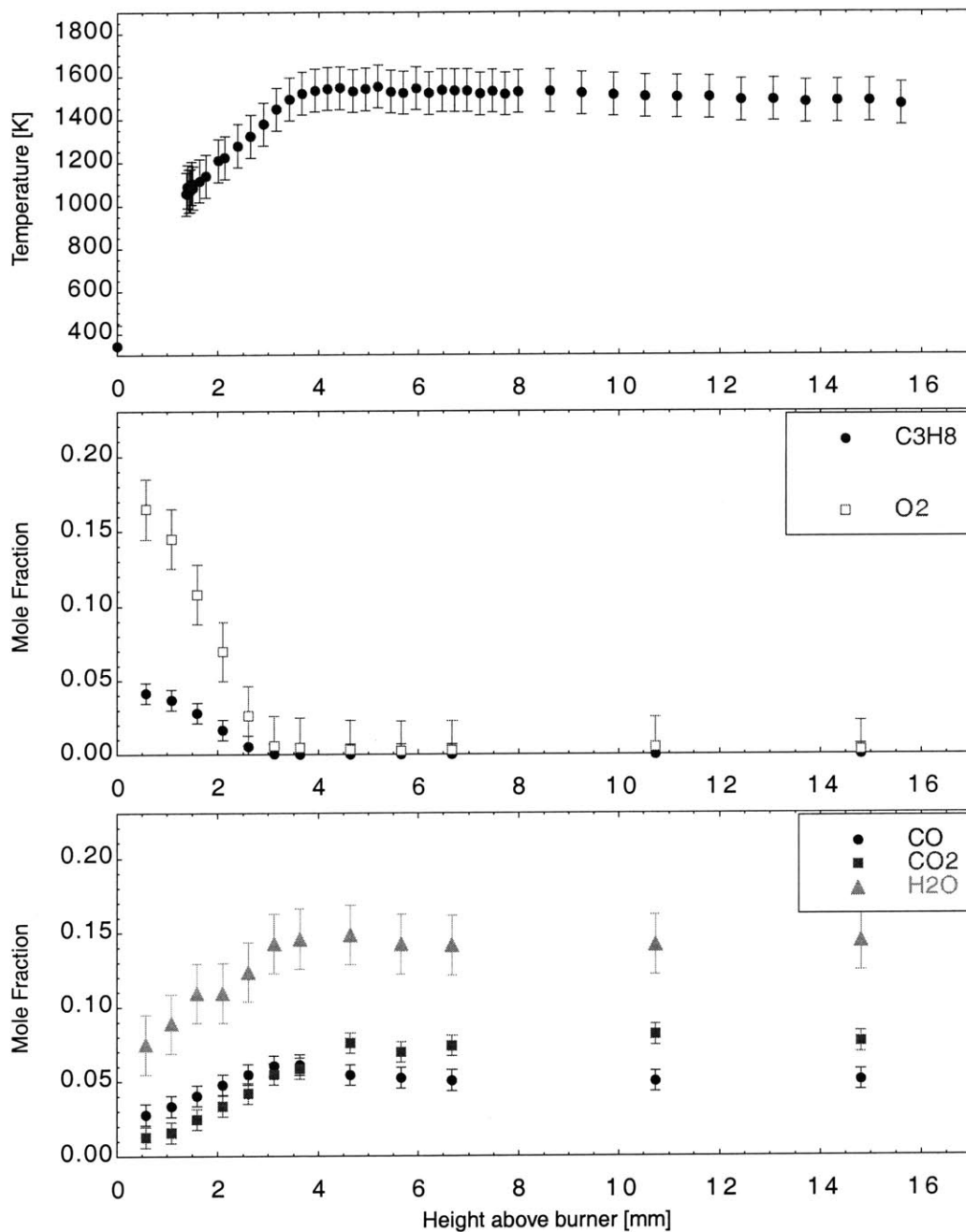
**Figure 8.3** Temperature and species profiles from a propane-air flame at  $\phi = 0.90$ . Filled symbols in the plots represent directly measured quantities; open symbols represent concentrations calculated via mass balance. The flame is shown in the image to the right. The horizontal line marks the burner surface at the flame center; each large scale division corresponds to 1 cm. Shadow at flame center is a bolt between flame and camera.





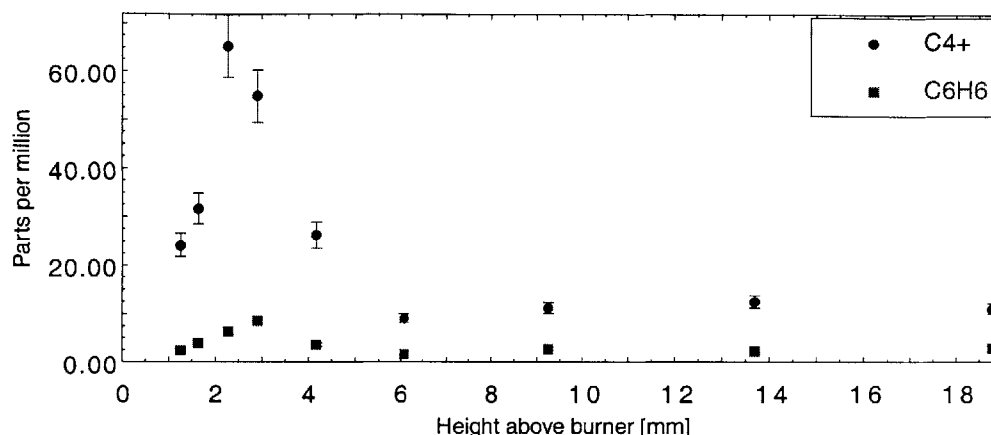
**Figure 8.4** Temperature and species profiles from a propane-air flame at  $\phi = 1.00$ . Filled symbols in the plots represent directly measured quantities; open symbols represent concentrations calculated via mass balance. The flame is shown in the image to the right. The horizontal line marks the burner surface at the flame center; each large scale division corresponds to 1 cm. Shadow at flame center is a bolt between flame and camera.





**Figure 8.5** Temperature and species profiles from a propane-air flame at  $\phi = 1.20$ . Filled symbols in the plots represent directly measured quantities; open symbols represent concentrations calculated via mass balance. The flame is shown in the image to the right. The horizontal line marks the burner surface at the flame center; each large scale division corresponds to 1 cm. Shadow at flame center is a bolt between flame and camera.





**Figure 8.6.** Minor species concentrations measured via GC/MS for the flame shown in Figure 8.5. The C4+ series represents the total concentration of smaller partially unsaturated hydrocarbons (C4 - C6) that are not resolved fully in the chromatogram.

$\phi = 1.2$  flame shows that the absorption trap - GC/MS system is able to resolve species profiles at very small concentrations, which is key to the identification of deposit precursor species.

### 8.5 Numerical Modeling of Burner Flames

Comparison of the data discussed above with detailed chemistry direct numerical simulations of these flames can provide another means of assessing the capabilities of the sampling and analysis system. By modeling the system with an existing validated propane oxidation mechanism, we may compare observed versus “true” peak widths and concentration values. In making such comparisons, however, it is important to keep in mind that while agreement between model and experiment tends to validate both results, it does not represent conclusive evidence that either is a completely accurate representation of the physical system.

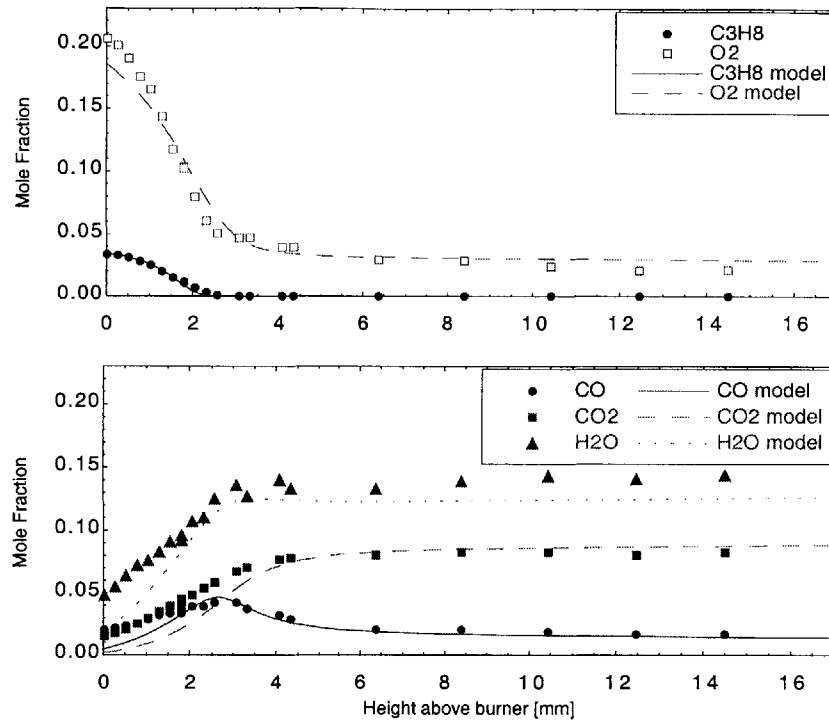
The burner flames were modeled using the Sandia PREMIX steady-state flame simulation code (Kee *et al.*, 1985). This method was chosen in order to test the experimental data against a widely used and verified numerical model. To account for heat loss from the flame gases to their surroundings, measured temperature profiles from the experiments were imposed on the numerical solutions. The other inputs to the simulation were the inlet mole fractions of propane, oxygen, and nitrogen, the total mass flow rate through the burner, and the operating pressure. Constant temperature and reactant mass fluxes are imposed as boundary conditions at

the burner surface (left boundary), and zero gradient boundary conditions are applied at the end of the flame domain (right boundary). Equilibrium species concentrations, determined by the input composition and the right boundary temperature and pressure, were used as an initial guess for the final gas compositions, but these concentrations were not enforced in the solutions.

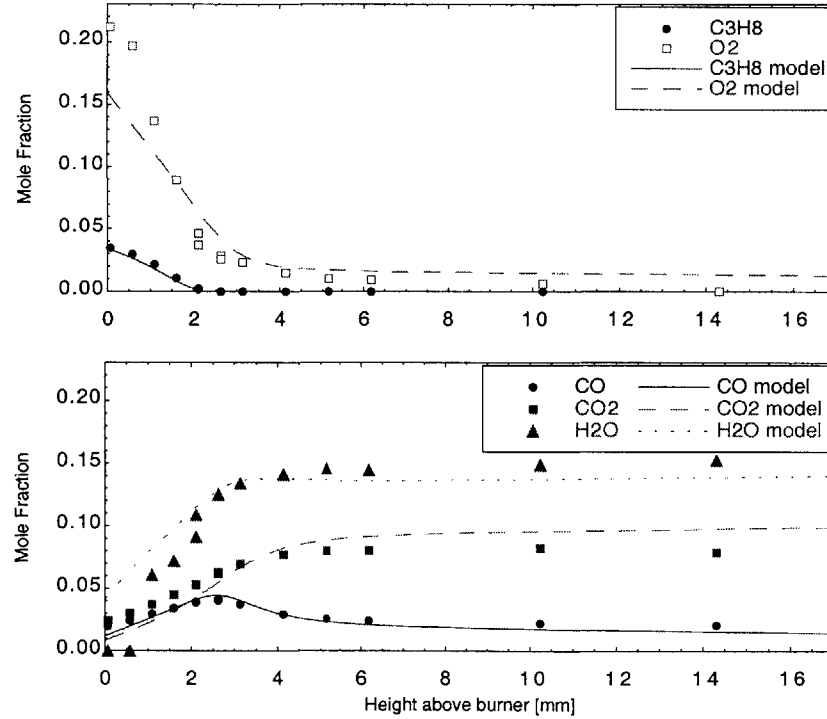
The chemical kinetic mechanism used to model the oxidation of propane was that of Dagaut, *et al.* (Dagaut, Cathonnet and Boettner, 1992; Dagaut, Cathonnet and Boettner, 1991). This oxidation model was chosen because it had been validated under various conditions, using both jet stirred reactor and shock tube data; one should also note that the model is not calibrated for burner-probe systems, so it should not compensate for the types of errors usually associated with this sort of apparatus (*e.g.* concentration profile offsets). The thermodynamic properties used were obtained from the CHEMKIN thermodynamic database (Kee, Rupley and Miller, 1990). A listing of the species, reactions, and kinetic rate constants used for this mechanism is included in Appendix II.

## 8.6 Numerical - Experimental Comparison

Figures 8.7 through 8.9 show comparisons of the experimentally determined species profiles with the numerical simulation results for each of the three flame conditions. The agreement between the experimental data and the model is in general quite good, especially in regard to the width of peaks and gradients in the concentration profiles. The propane profile is well resolved in all three cases, and the carbon monoxide peaks also match fairly well. The differences between the experimental profiles and the model results that are seen do not form a regular pattern over all three cases (for example, consistent lowering and broadening of peaks in the experiment relative to the model), which indicates that the errors are not systematic. Given

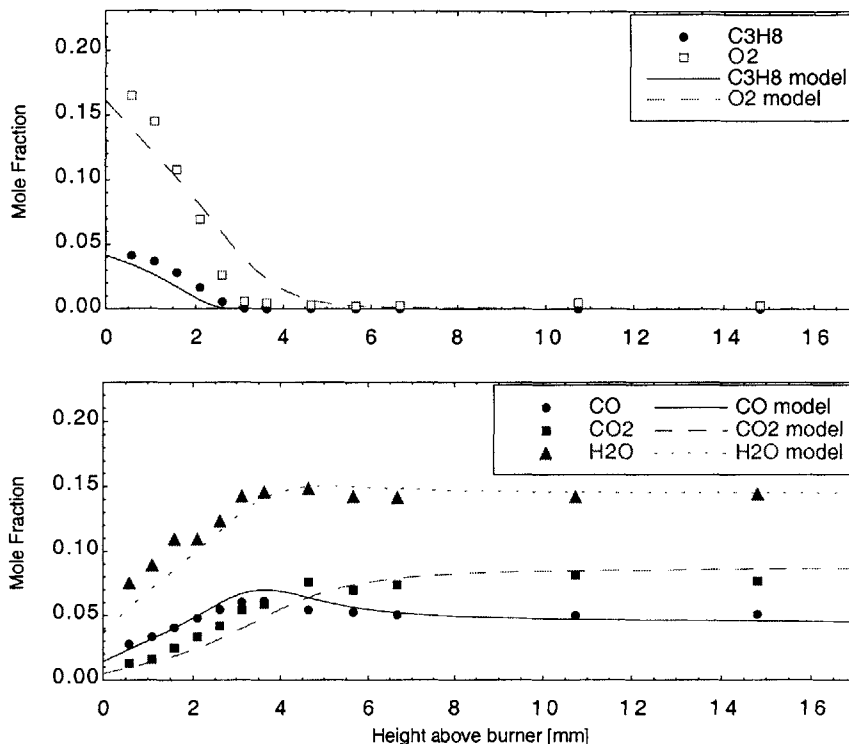


**Figure 8.7** Comparison of experimental results and direct numerical simulation of a propane-air flame at  $\phi = 0.9$ . The rest of the data for this flame is found in Figure 8.3.



**Figure 8.8** Comparison of experimental results and direct numerical simulation of a propane-air flame at  $\phi = 1.0$ . The rest of the data for this flame is found in Figure 8.4.





**Figure 8.9** Comparison of experimental results and direct numerical simulation of a propane-air flame at  $\phi = 1.2$ . The rest of the data for this flame is found in Figure 8.5.

these results, it appears that the sampler performance is sufficient to observe species concentration profiles at these resolutions.

The discrepancies that do exist between the experimentally observed profiles and the numerical results could be caused by several factors in addition to the experimental error sources noted in Chapter 7 and potential inaccuracies in the reaction mechanism or rate constants. One of the most important error sources to consider here is the temperature measurement. Since the numerical calculation depends on experimentally measured temperatures, and the reaction rates are extremely sensitive to temperature, small temperature errors can lead to significant concentration offsets. However, this effect should lead to predictable changes in the model results, since the species profiles are linked by reaction rates and mass balances; for example, high CO concentrations in the model relative to the experiment should be accompanied by low CO<sub>2</sub> concentrations, if the main error source is the temperature measurement. Another factor to consider is pressure effects in the chemical reaction mechanism. The mechanism used for these

calculations is verified at atmospheric pressures and above; the pressure corrections used for reactions that depend on third bodies (notably CO to CO<sub>2</sub> conversion) may not make correct predictions at the pressures used in these experiments. The likely effect of lower pressures is to slow the rates of third-body reactions. Another effect to consider is the opening of additional reaction pathways under different pressure conditions. A detailed study of the effects of pressure on reaction rates in this system is outside the scope of this work, but would be an extremely valuable addition to the chemical kinetic model.

From the numerical models of the three flames, it is easy to calculate the heat flux to the burner surface, as an estimate of the degree of cooling of the flame by the burner. A comparison of the surface heat fluxes to the total heat produced by the flame (local heat release integrated along the flame coordinate) is given in Table 8.2. Note that these flames lose significant fractions of their heat release energy to the burner surface, up to 20 percent in the  $\phi = 1.2$  case.

Equivalence Ratio	Calculated Surface Heat Flux [J/cm <sup>2</sup> /s]	Calculated Total Heat Release [J/cm <sup>2</sup> /s]	Percent Heat Loss to Burner
0.9	1.33	11.14	11.9
1.0	1.34	11.94	11.2
1.2	1.72	7.90	21.8

**Table 8.2** Heat loss versus heat release for burner-stabilized propane-air flames.

## 8.7 Conclusions

The experiments discussed in this chapter demonstrate the applicability of the flame control, positioning, sampling and analysis techniques to the types of systems we wish to observe. Sampling resolution and repeatability is sufficient to observe species profiles within the pre-flame zone, even though the thickness of this region may be only a few millimeters. The concentration profile results are insensitive to the radial positioning of the probe, despite the use of a drilled rather than sintered plate for the burner surface. Sample retention between runs was never observed in the FT/IR analysis, and was eliminated from the GC/MS absorption trap system. Nevertheless, the sample retention test described in this chapter should be used frequently to

check for hydrocarbon absorption effects as seals and other components of the sampling system age and are exposed to large amounts of sample mass flow.

The agreement between the observed concentration profiles and numerical simulation results is promising. While not exact, the numerical simulations of the experimental flames can provide a realistic thermal and chemical environment to use as a basis for examining the deposit precursor formation chemistry that occurs in the toluene-doped propane-air flames, as discussed in the following chapters.

## 8.8 References

- P. Dagaut, M. Cathonnet, and J-C. Boettner, "Kinetics of Ethane Oxidation," *International Journal of Chemical Kinetics*, Vol. 23, 437-455 (1991).
- P. Dagaut, M. Cathonnet, and J-C. Boettner, "Kinetic Modeling of Propane Oxidation and Pyrolysis," *International Journal of Chemical Kinetics*, Vol. 25, 813-837 (1992).
- R.J. Kee, J.F. Grcar, M.D. Smooke, and J.A. Miller, "A FORTRAN Program for Modeling Steady Laminar One-Dimensional Premixed Flames," *Sandia National Laboratories Report SAND85-8240* (1985).
- R.J. Kee, F.M. Rupley, and J.A. Miller, "The CHEMKIN Thermodynamic Data Base," *Sandia National Laboratories Report SAND87-8215B* (1990).



*Experimental Observations of Toluene Oxidation Chemistry in the Pre-Flame Zone***9.1 Experimental Objectives**

The study of toluene-doped propane-air flames presented in this chapter is intended to address a number of the goals outlined in Chapter 3; namely, the direct identification of deposit precursor molecules formed from engine-relevant fuels in the pre-flame region of the experimental burner, the characterization of these precursors in terms of chemical structure and molecular weight, and the observation of interactions between the competing physical processes that contribute to the formation and transport of these molecules in the gas phase. In addition to identifying candidate deposit precursor species, the measurement of their concentration profiles in the flames can provide a starting point for describing the chemical mechanisms by which toluene is converted into deposit precursor species in the pre-flame region.

Flames at four different equivalence ratios were observed, ranging from  $\phi = 0.86$  to  $\phi = 1.1$ , with other flame properties maintained as constant as possible across the series, in order to isolate the role of oxygen concentration in the deposit precursor formation process.

**9.2 Experimental Method**

The main parameters that define the flames used for these experiments are equivalence ratio, toluene-to-propane ratio, unburned gas velocity, system pressure, and burner surface temperature. A listing of these values for each flame, along with the flow rates used to achieve each set of conditions, is given in Table 9.1. The toluene to propane ratio is defined as the percent of total carbon in the fuel mixture supplied by the toluene. As a function of mass flow rates, this ratio is given by the following expression:

$$F_{tol} = \frac{\gamma \dot{m}_{tol} / w_{tol}}{\gamma \dot{m}_{tol} / w_{tol} + 3 \dot{m}_{pro} / w_{pro}} \quad (9.1)$$

where  $\dot{m}_{tol}$  is the mass flow rate of toluene,  $w_{tol}$  is the molecular weight of toluene (92 g/mol),  $\dot{m}_{pro}$  is the mass flow rate of propane and  $w_{pro}$  is the molecular weight of propane (44 g/mol). To provide toluene vapor to the system, the toluene evaporator (described in Chapter 7) was operated

with the source tank pressurized to 2 atmospheres with dry nitrogen, and the evaporation zone heated to 150 °C. In changing equivalence ratios, the toluene to propane ratio, unburned gas velocity, pressure and burner surface temperature were kept constant as far as was possible. As with the undoped flame experiments, no gas flow was needed in the outer ring section of the burner; the flames were sufficiently one-dimensional and stable using the central flow section alone. The heating value per unit mass of the fuel-air mixtures with toluene is approximately one percent higher than a pure propane mixture with the same equivalence ratio and unburned gas velocity.

Equivalence Ratio	Toluene to Propane Ratio	Unburned Gas Velocity [cm/sec]	Pressure [mbar]	Burner Surface Temperature [°C]	Propane Flow Rate [mg/sec]	Toluene Flow Rate [mg/sec]	Air Flow Rate [mg/sec]
0.86 ± 0.01	10.7 ± 0.2	20.5 ± 0.2	144.3 ± 0.5	66 ± 2	8.5 ± 0.1	0.91 ± 0.05	169 ± 2
0.96 ± 0.01	10.7 ± 0.2	20.5 ± 0.2	142.8 ± 0.5	71 ± 2	9.5 ± 0.1	1.02 ± 0.05	168 ± 2
1.00 ± 0.01	11.4 ± 0.2	20.3 ± 0.2	143.5 ± 0.5	69 ± 2	9.8 ± 0.1	1.13 ± 0.05	167 ± 2
1.10 ± 0.01	11.5 ± 0.2	20.5 ± 0.2	143.0 ± 0.5	68 ± 2	10.8 ± 0.1	1.25 ± 0.05	167 ± 2


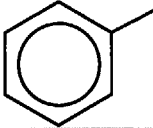
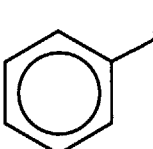
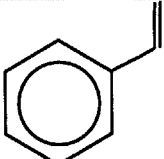
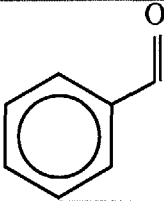
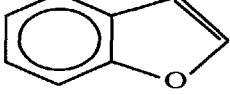
**Table 9.1.** Flame characteristic parameters for toluene-doped propane flame experiments.

For each flame, major and minor species profiles were collected via FTIR and GCMS, along with temperature profiles and flame images. The FTIR samples were recorded at sample cell pressures of 50 to 65 millibar; sample collection times ranged from eight to fourteen minutes. GC/MS samples were collected on adsorption traps for eight minutes at each sampling point. The pressure at the traps was not controlled, as the sensitivity of the trapping efficiency to pressure is negligible; values varied from 5 to 10 millibar. Two traps were used in series for each sample; no peaks were observed in the GCMS data for any of the second traps; indicating that no sample breakthrough or saturation occurred. FTIR and GCMS data were analyzed according to the procedures described in Chapter 7 in order to produce concentration values from the spectra and chromatograms.

### 9.3 Observed Species and Temperature Profiles in Toluene-Doped Propane-Air Flames

Figures 9.1 through 9.8 show the flame images, temperatures and species profiles for each of the four equivalence ratios. The error bars shown in the plots are largely due to thermocouple offset for the temperature, FTIR sample cell pressure measurement error for the major species concentrations, and errors in probe mass flow due to temperature uncertainty for the minor species concentrations.

The major species and temperature profiles are generally similar to those observed in the undoped propane-air flames (see Chapter 8). Visually, the flames are also indistinguishable from their undoped counterparts at the same equivalence ratios and unburned gas velocities. Thus, these flames appear to provide a minimally interfering environment for the study of the detailed

Species	Boiling Point (K)	Structure
Benzene	353.0	
Toluene	383.8	
Ethylbenzene	409.4	
Styrene	418.4	
Benzaldehyde	451.2	
Benzofuran	447.2	

**Table 9.2.** Observed toluene reaction products from toluene-doped propane-air flames.

chemistry involved in the toluene oxidation process.

A number of toluene reaction products are observed in all of the flames. Table 9.2 lists the various species observed, along with their standard boiling points and representations of their chemical structures. As noted in the previous chapters, smaller saturated or partially unsaturated hydrocarbons are not resolved by the current analytical method; benzene is the lightest hydrocarbon that produces a distinct peak in the chromatograms. However, the total concentration of the unresolved hydrocarbons never exceeded 100 ppm which, while not

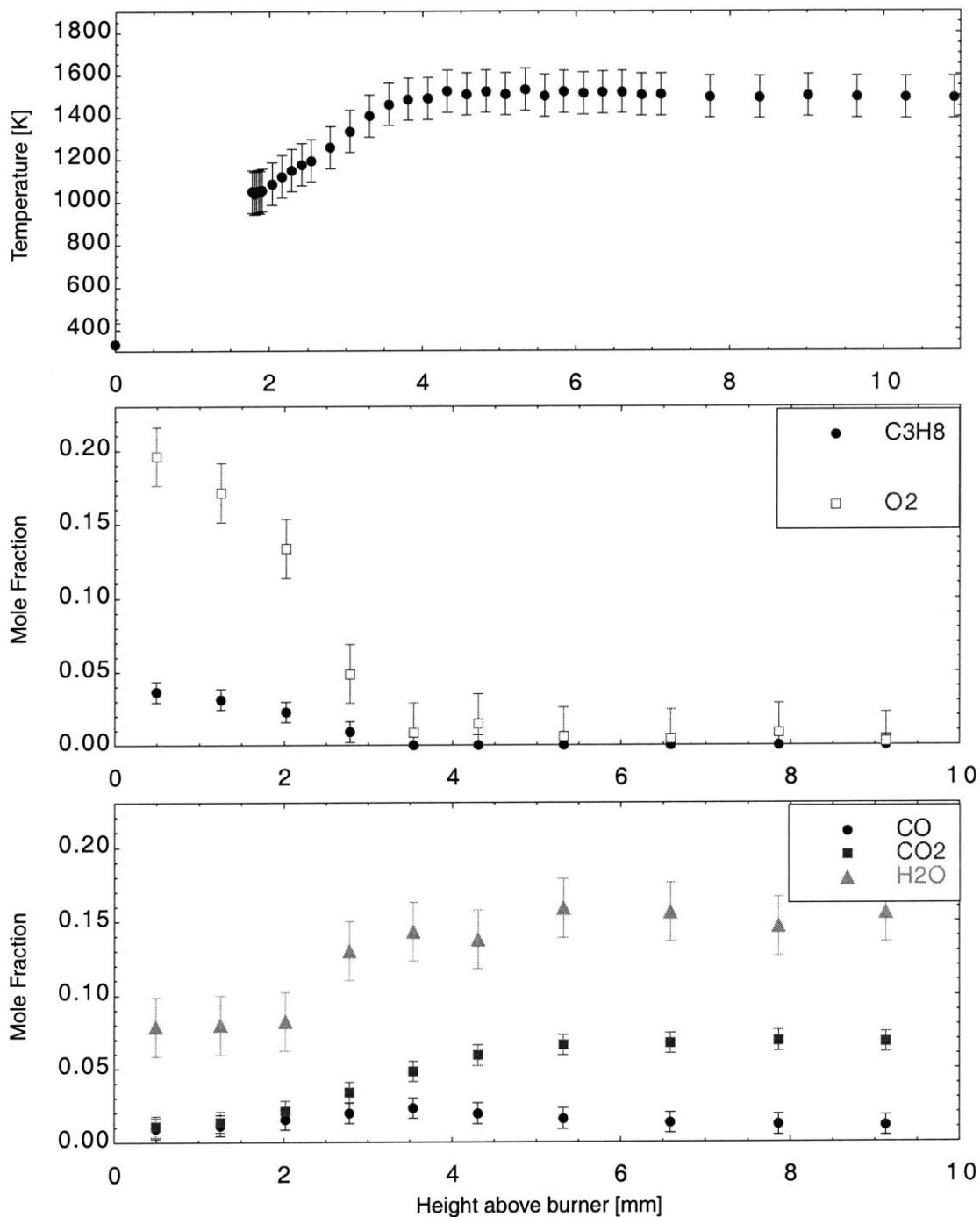
negligible, is smaller than most of the observed toluene reaction product concentrations (see Figures 9.2, 9.4, 9.6, 9.8).

Several observations about the chemical reaction mechanism of toluene oxidation in the quench layer can be made based simply on the structures of the observed species. The toluene does undergo some limited amount of addition chemistry, leading to compounds of increasing molecular weight, such as benzofuran. However, the multi-ring aromatics that would result from soot-like growth processes are not observed. As noted above, the total concentration of smaller, partially unsaturated hydrocarbons that would result from ring breaking is relatively low, especially in the quench region where the major toluene reactions are taking place. This suggests that ring-breaking chemistry is not as important as addition chemistry in the quench zone (although ring-breaking mechanisms certainly are important in the hotter region of the flame, where the input toluene and its derivatives are oxidized completely. Another point to note is that oxygen addition is observed in the gas phase in the quench layer; both benzaldehyde and benzofuran contain a single oxygen atom.

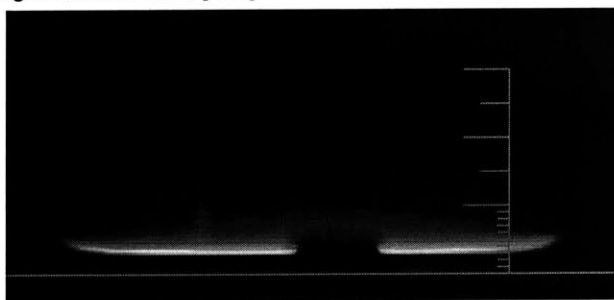
The effect of oxygen concentration on the toluene oxidation chemistry does not appear to be particularly strong in this range of equivalence ratios. Slight shifts in the concentration profiles are observed, but almost all the main products listed in Table 9.2 are found in all four flames at similar concentration levels. Figure 9.9 shows the effect of changing equivalence ratio on benzaldehyde, benzofuran and styrene. All three species seem to have reduced overall concentrations at leaner equivalence ratios, by up to a factor of four. It also appears that the species profiles shift away from the burner surface as the equivalence ratio increases, but this effect is within the range of experimental error.

No significant deposition was observed on the burner surface after approximately 20 hours of toluene-doped propane flame burning; however, deposition is likely to be low under the experimental conditions due to the reduced pressures and convective fluxes away from the burner surface.





**Figure 9.1.** Major species and temperature profiles for a toluene-doped propane flame at  $\phi = 0.86$ , pressure of 144 millibar, and unburned gas velocity of 20.5 cm/s. Flame image is shown at right; shadow in image is due to a bolt between the flame and camera.



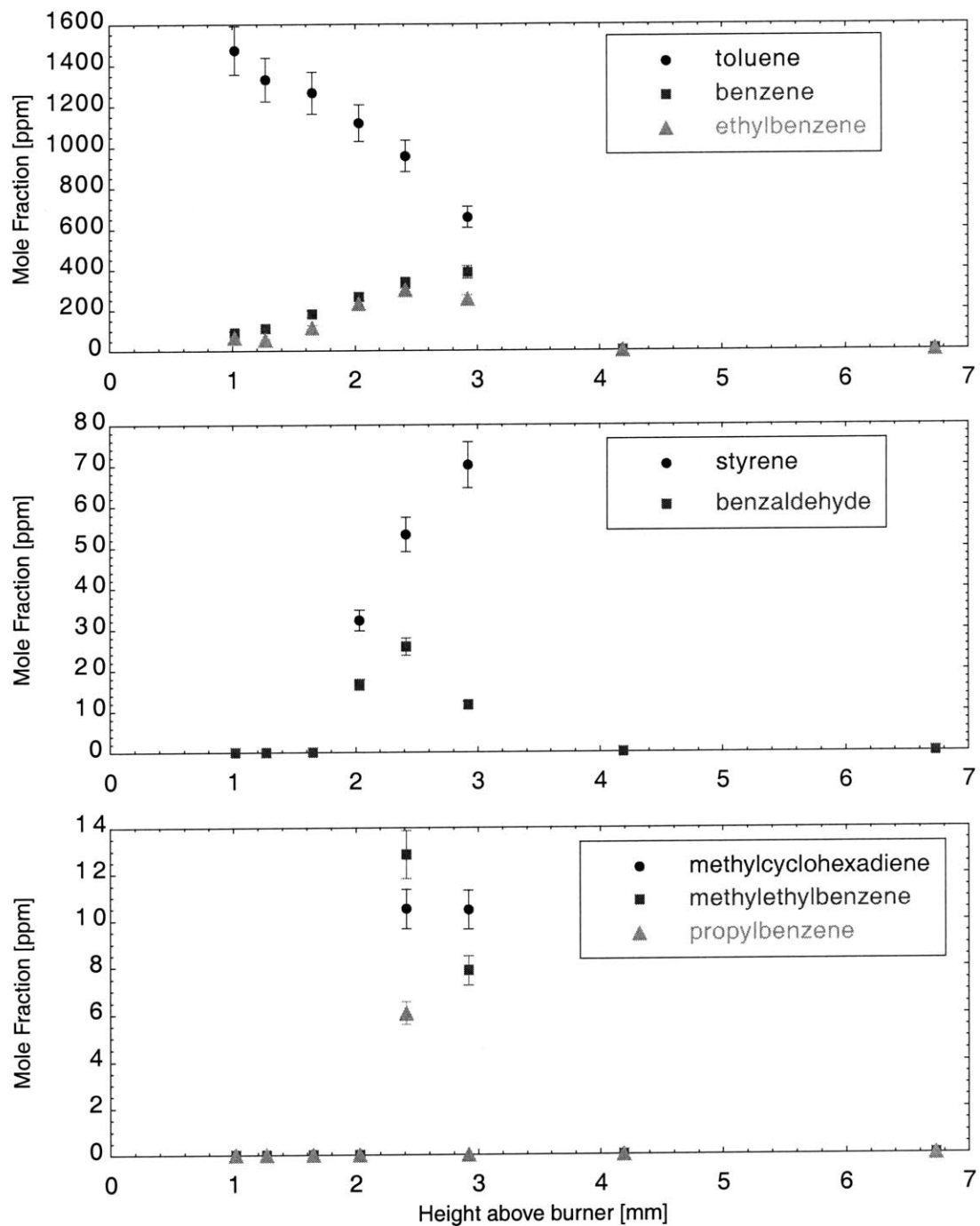
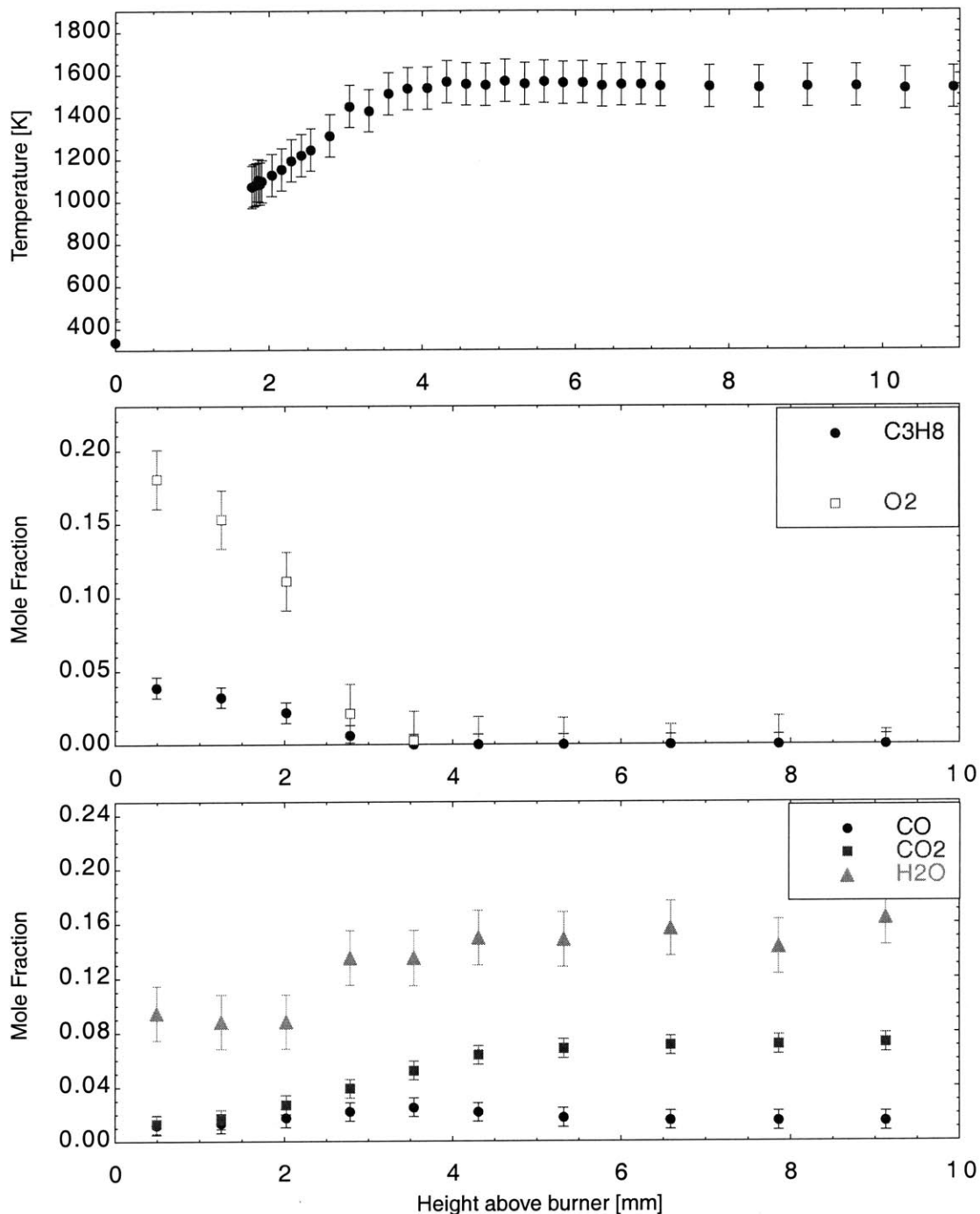
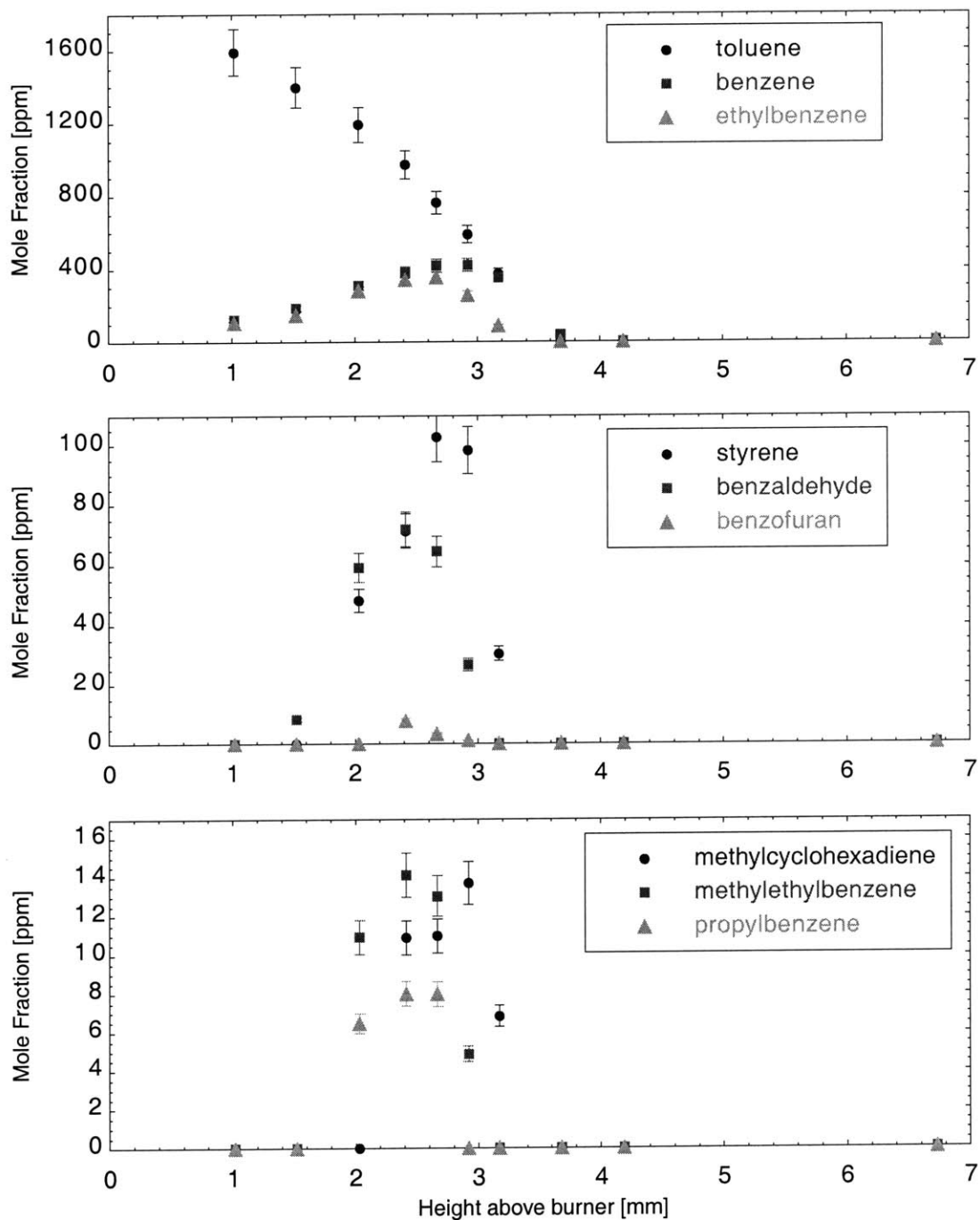


Figure 9.2. Minor species profiles for a toluene-doped propane flame at  $\phi = 0.86$  (see Figure 9.1).

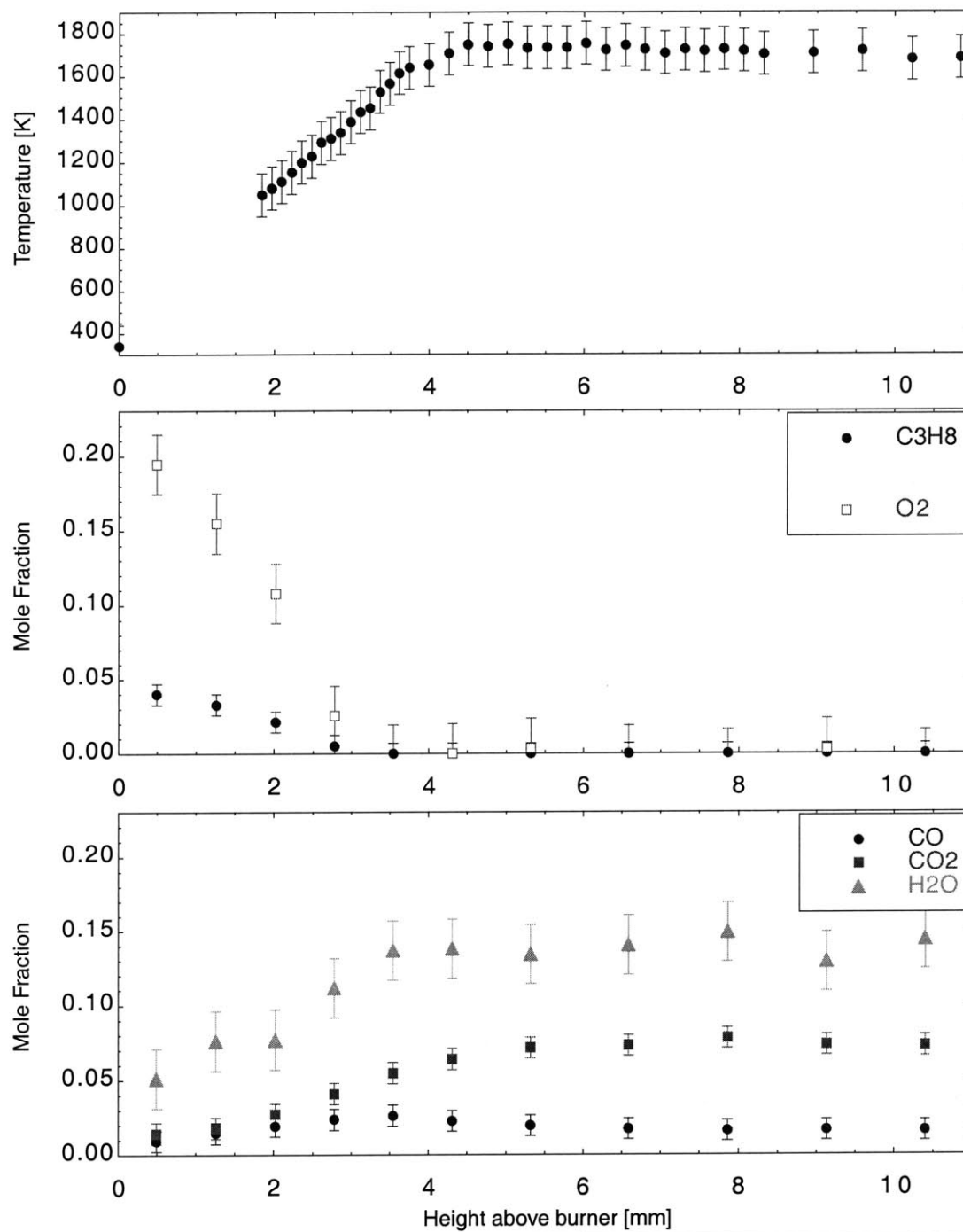


**Figure 9.3.** Major species and temperature profiles for a toluene-doped propane flame at  $\phi = 0.96$ , pressure of 143 millibar, and unburned gas velocity of 20.5 cm/s. Flame image is shown at right; shadow in image is due to a bolt between the flame and camera.





**Figure 9.4.** Minor species profiles for a toluene-doped propane flame at  $\phi = 0.96$  (see Figure 9.3).



**Figure 9.5.** Major species and temperature profiles for a toluene-doped propane flame at  $\phi = 1.00$ , pressure of 144 millibar, and unburned gas velocity of 20.3 cm/s. Flame image is shown at right; shadow in image is due to a bolt between the flame and camera.



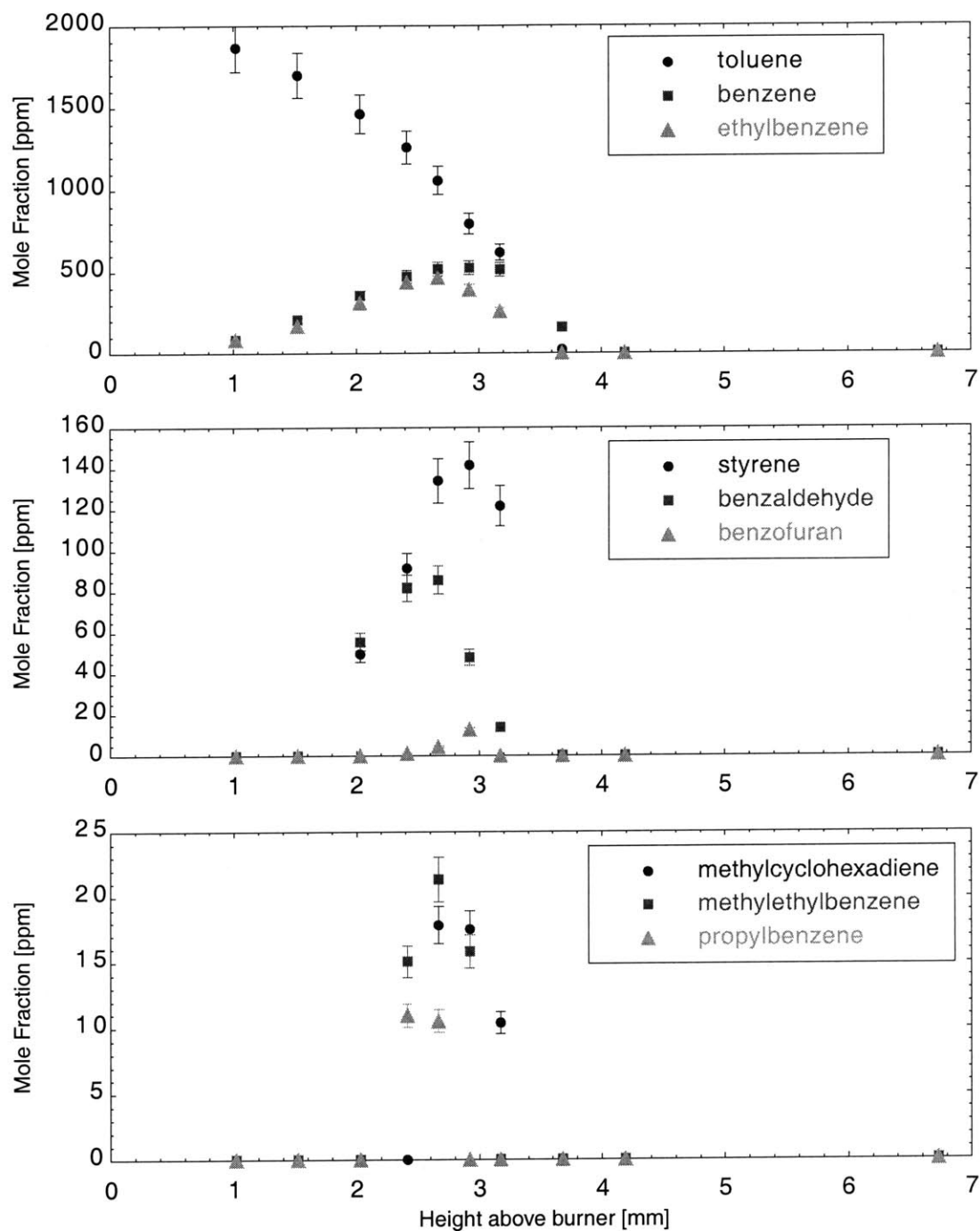
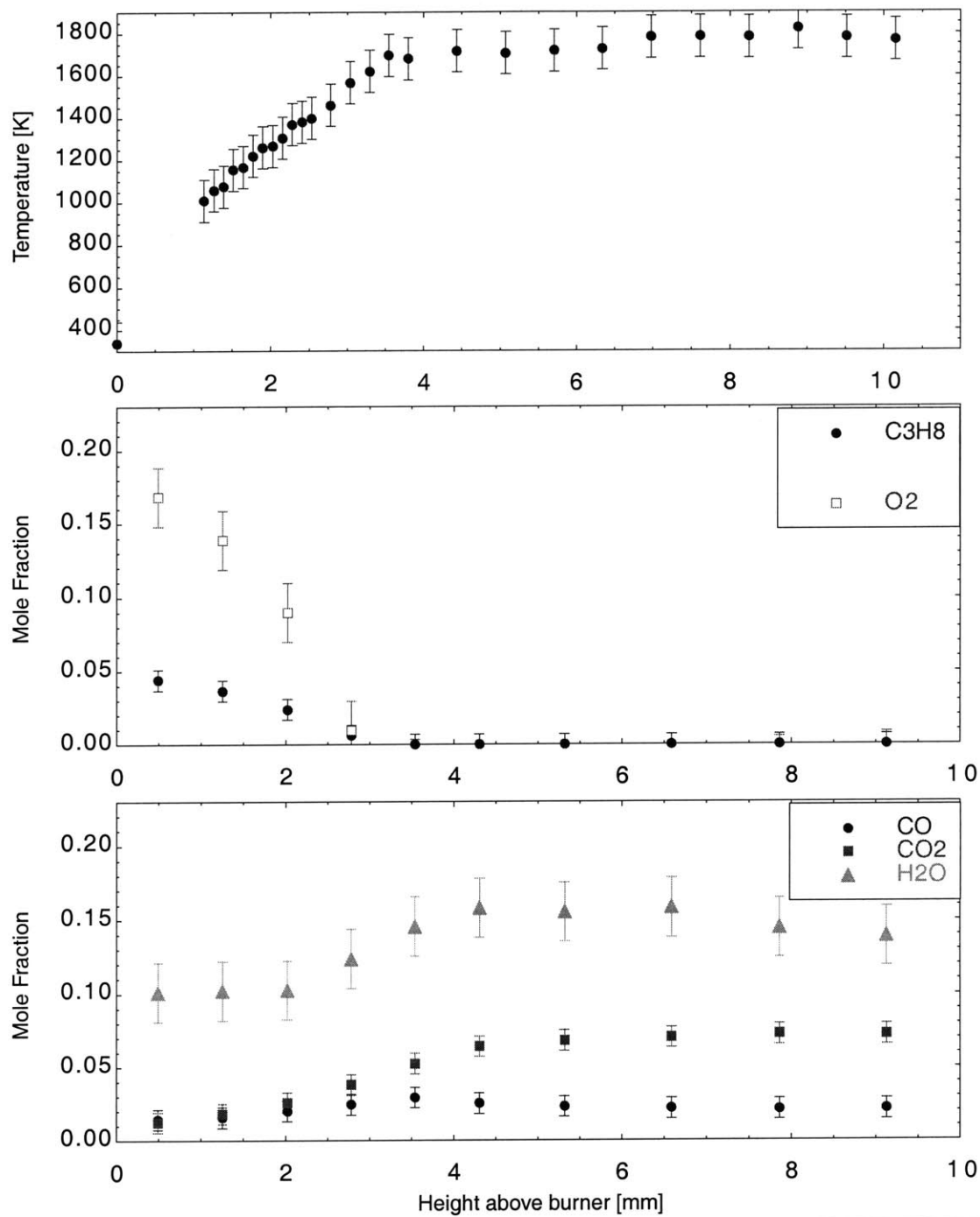
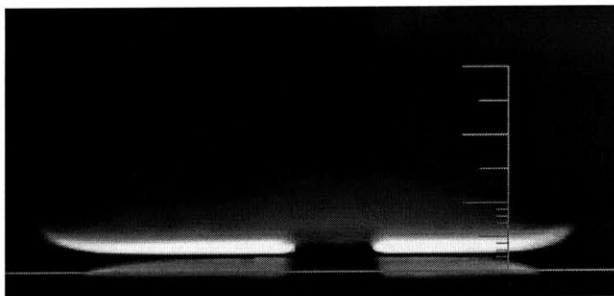
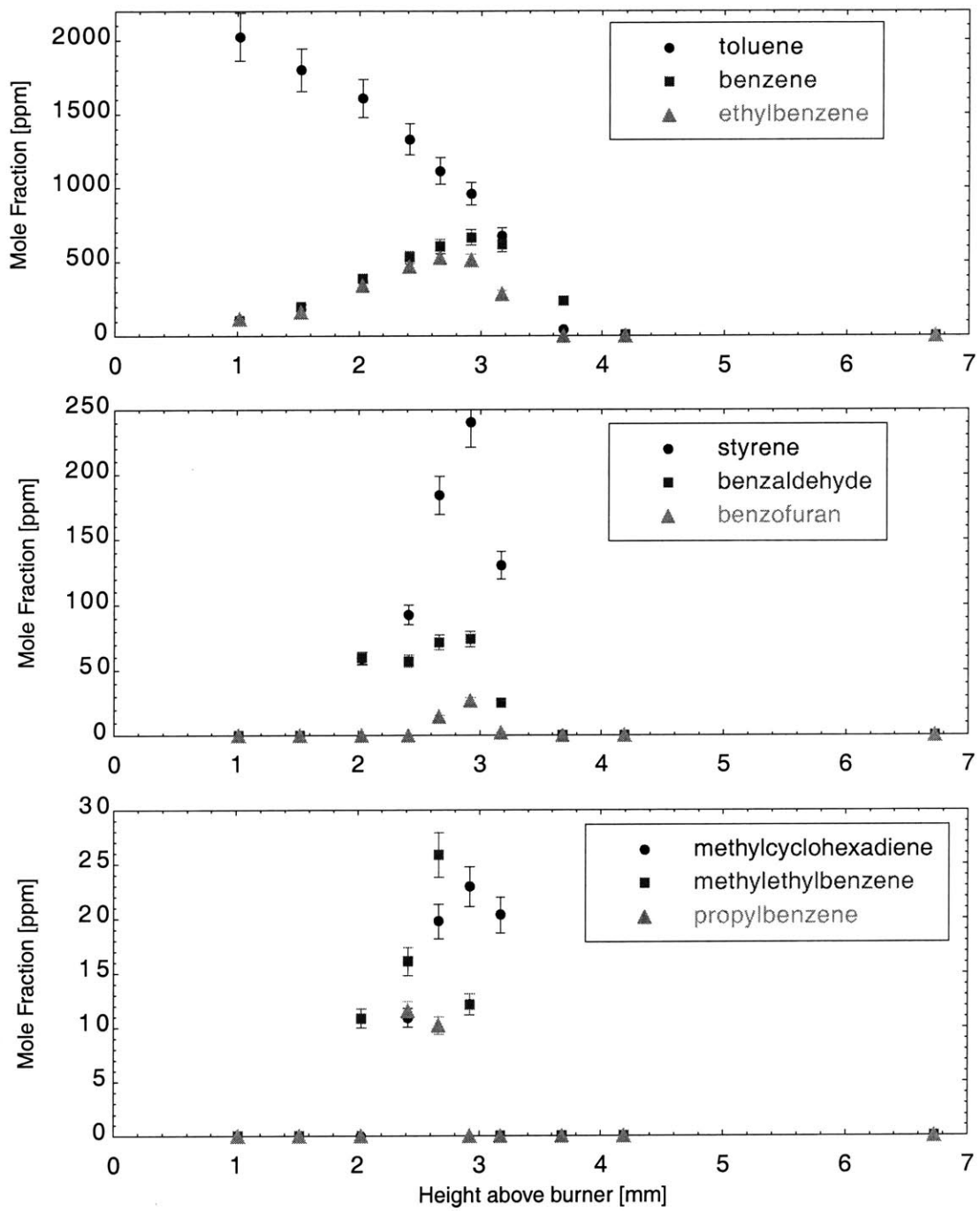


Figure 9.6. Minor species profiles for a toluene-doped propane flame at  $\phi = 1.00$  (see Figure 9.5).



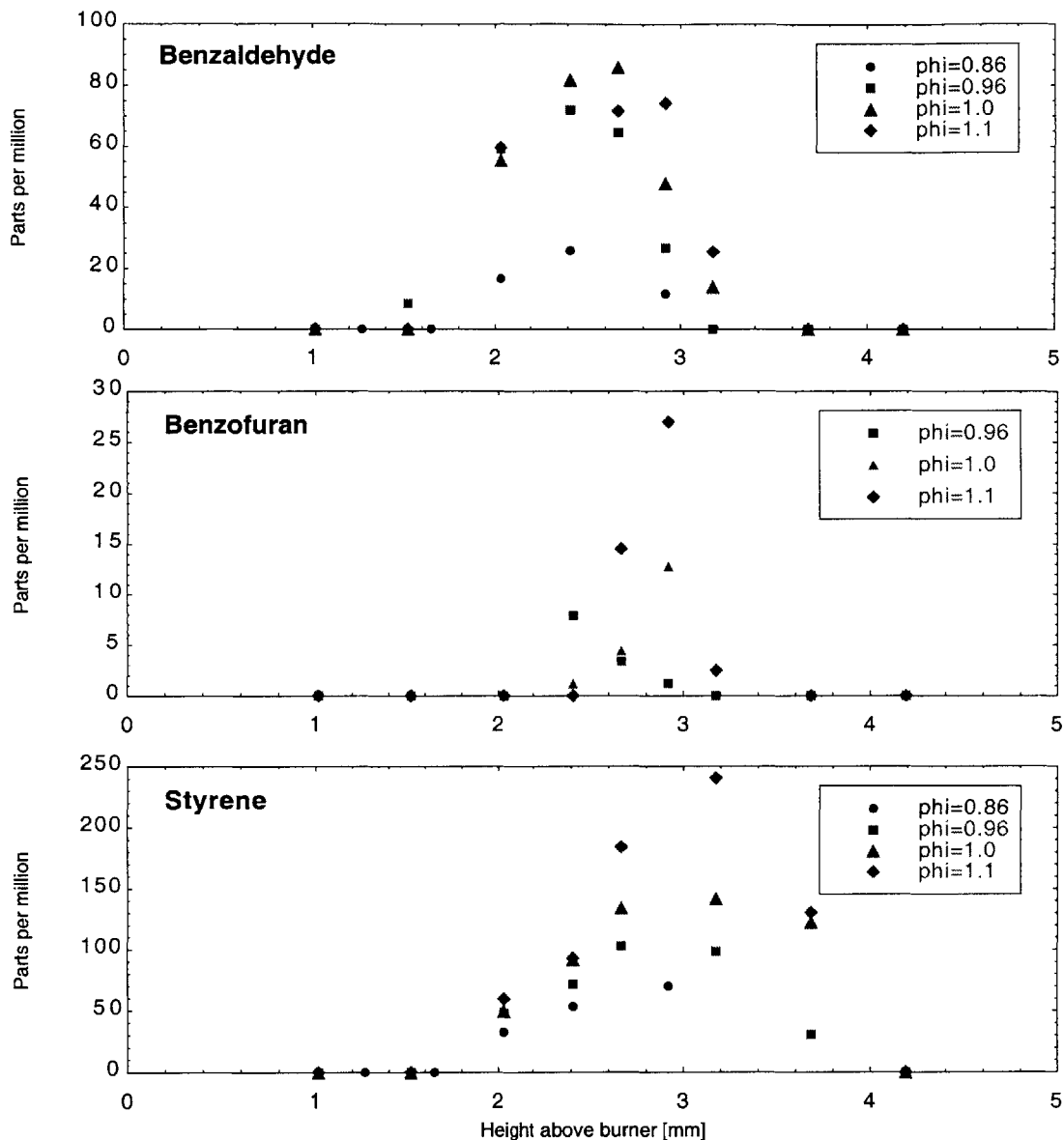
**Figure 9.7.** Major species and temperature profiles for a toluene-doped propane flame at  $\phi = 1.10$ , pressure of 143 millibar, and unburned gas velocity of 20.5 cm/s. Flame image is shown at right; shadow in image is due to a bolt between the flame and camera.





**Figure 9.8.** Minor species profiles for a toluene-doped propane flame at  $\phi = 1.10$  (see Figure 9.7).





**Figure 9.9.** Comparison of benzaldehyde, benzofuran, and styrene profiles resulting from different equivalence ratios.

#### 9.4 Identification of Deposit Precursor Candidate Species

From the toluene derivatives discussed above, we can choose likely candidates for deposit precursor molecules. As can be seen in Table 9.2, both benzaldehyde and benzofuran have boiling points around 450 K, as opposed to toluene which boils at 384 K. A major reason for the higher boiling points of these two species is the presence of oxygen in their molecular structures. Both the lower volatility and oxygen content suggest these molecules as the most

likely candidates for deposit precursors. Styrene and ethylbenzene are also potential candidates, due to their relatively high boiling points.

### 9.5 Suggested Toluene Partial Oxidation Mechanism

The range of toluene-derived species observed in the experiments strongly suggests a reaction mechanism centered around the benzyl radical ( $C_6H_5CH_2\cdot$ ). This radical may be formed by a simple hydrogen abstraction from toluene; it is resonance stabilized, making it relatively unreactive, so that it may survive for long periods of time in the flame. Most of the other observed species can be created through simple reactions of benzyl with other common radicals or through abstraction of functional groups: methyl plus benzyl can produce ethylbenzene, oxygen or OH can lead to benzaldehyde, etc.

Major reaction pathways involving the benzyl radical have been proposed for toluene oxidation chemistry by other authors (Emdee, 1992, Seuwen, 1996). Other major reaction pathways, notably those which involve oxygen addition to the aromatic ring, are not observed in these experiments. For example, none of the species one would expect from the creosol pathway proposed by Emdee *et al.* are observed in the current experimental results.

Thus, from the limited amount of data available from these experiments, it seems that the major mechanism for deposit precursor formation from toluene under the experimental conditions consists of an initial step of producing a benzyl radical, followed by a small set of relatively fast reactions leading to heavier and oxygenated species such as ethylbenzene, benzaldehyde and benzofuran. This mechanism outline will be developed further in the following chapter.

### 9.6 Reaction / Diffusion / Convection Analysis for Identified Precursor Candidates

It is possible to form a quick estimate of the diffusion of the potential deposit precursors to the wall, taking advantage of the steady-state nature of the experimental flame. At any point in the domain, the species conservation equation 9.2 must be satisfied:

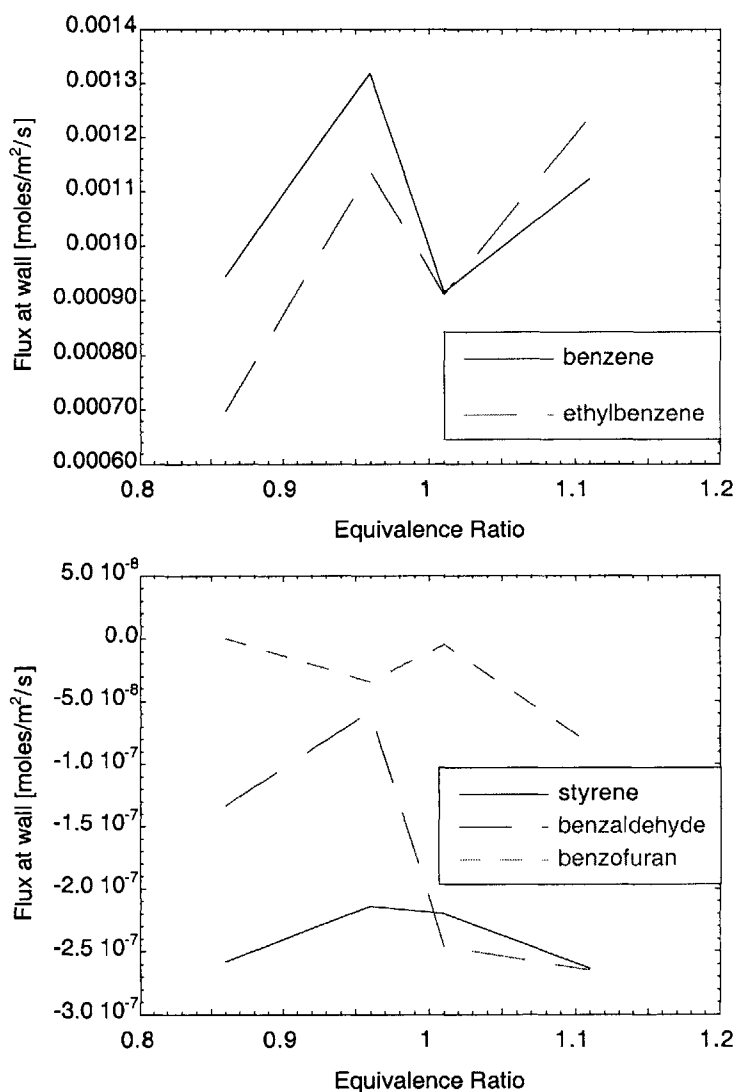
$$\frac{\partial}{\partial x} \left( \rho u Y_i - \rho D_i \frac{\partial Y_i}{\partial x} \right) + \dot{w}_i = 0 \quad (9.2)$$

where  $\rho$  is the gas density,  $u$  the gas velocity,  $D_i$  the diffusion coefficient for species  $i$ ,  $Y_i$  the mass fraction of species  $i$  and  $w_i$  is the chemical production rate of species  $i$ . If we choose a location in the flame where the production rate of the species is negligible, then Equation 9.2 reduces to

$$\rho u Y_i - \rho D_i \frac{\partial Y_i}{\partial x} = \text{constant} = \dot{m}_{i,0} \quad (9.3)$$

in which the constant  $\dot{m}_{i,0}$  is equal to the mass flux of the species  $i$  at the wall, or zero point of the domain). If we assume the reaction mechanism discussed above, and further assume that no significant amounts of reaction occur before the beginning of toluene conversion to the benzyl radical, we can define a region in the experimental flames where Equation 9.3 is valid, extending from the burner surface to the beginning of the rapid rise in toluene conversion rate

If we solve Equation 9.3 for the various toluene derived species seen in the experimental flames, using the earliest measurable points



**Figure 9.10.** Calculated fluxes at the wall surface for several experimentally observed toluene derivatives. All fluxes are in moles/m<sup>2</sup>/s. Benzene and ethylbenzene demonstrate fluxes away from the wall, this is physically unreasonable for species produced in the flame, and indicates that the assumption of insignificant reaction in the area before the first measurable concentrations is not valid for these species; styrene, benzaldehyde and benzofuran show fluxes towards the wall.

in the profiles in order to remain in the reaction-free region, we find that several of the species, notably benzaldehyde and benzofuran, show fluxes towards the burner surface. Calculated fluxes for some of the species are shown in Figure 9.10. The fluxes of ethylbenzene and benzene, which are positive and hence directed away from the surface, are physically unreasonable since these two species are produced in the flame, and are not contained in the incoming gas stream. This suggests that the reaction fluxes for these species are significant in the region near the burner surface, which is reasonable considering their large concentrations in the early part of the flame. Hence, this analysis method is not applicable for these species, and the fluxes toward the surface obtained for the other species should be considered with the potential errors due to the negligible reaction assumption in mind.

## 9.7 Conclusions

The experiments discussed in this chapter have demonstrated the ability of the experimental system to resolve concentration profiles of deposit precursor candidate species in the quench region of low pressure flames. With toluene used as the dopant, a number of toluene derivatives were formed, most corresponding to addition reactions to the benzyl radical. The derived species generally had higher boiling points than toluene, ranging as high as 451 K. Two oxygenated species were observed, benzaldehyde and benzofuran. These two species, along with styrene, are likely candidates for deposit precursor molecules. As additional support to this hypothesis, a flux analysis shows that styrene, benzaldehyde and benzofuran all exhibit fluxes towards the burner surface, although the assumption of small reaction contributions may introduce significant error into these flux values.

## 9.8 References

- J.L. Emdee, K. Brezinsky, and I. Glassman, "A Kinetic Model for the Oxidation of Toluene Near 1200 K," *Journal of Physical Chemistry* Vol. 96, 2151-2161 (1992).
- R. Seuwen and P. Warneck, "Oxidation of Toluene in NO<sub>x</sub> Free Air: Product Distribution and Mechanism," *International Journal of Chemical Kinetics*, Vol. 28, 315-332 (1996).

### 10.1 Mechanistic Evidence from Experiments

The toluene-doped propane-air flame concentration profiles described in the preceding chapter provide a fairly clear picture of the main features of the chemistry of toluene in the pre-flame zones of the experimental flames. The differences in molecular weight between toluene and its derivatives produced in the flame were minor, and most of the observed reaction products corresponded to side-chain reactions, with very small amounts of ring-breaking chemistry occurring. This relatively constrained set of products affords us the opportunity to build a reasonably simple chemical mechanism to describe the reactions consuming toluene and producing potential deposit precursor molecules such as benzaldehyde and benzofuran.

This chapter describes the development of a reaction mechanism for the partial oxidation of toluene in the pre-flame region. This mechanism is not intended to be a complete model of all the reaction pathways available to toluene under these conditions, but rather to capture some of the main features of the observed toluene chemistry in a straightforward way. The mechanism will be used in two cases: first, to model one of the experimental flames and compare with the results of the simple flux analysis presented in Chapter 9, and secondly to model deposition during a flame quench event with toluene-doped fuel. The second case will allow us to assess the ability of species observed in the experimental data to act as deposit precursors.

### 10.2 Comparison of Observed Species Profiles With Literature Mechanisms

Few chemical kinetic mechanisms for toluene oxidation have been produced, as it is a complex molecule and thus requires models with large numbers of reactions. However, as one of the simplest aromatic hydrocarbons, it has received some study. Seuwen and Warneck (1996) studied the oxidation of toluene in chlorine-radical initiated reactions at low temperatures. They observed very different product distributions from those seen in this study, with cresols as major products, and benzaldehyde and benzyl alcohol as a minor pathway only. It is quite reasonable that significantly different reaction pathways would be observed under these atmospheric

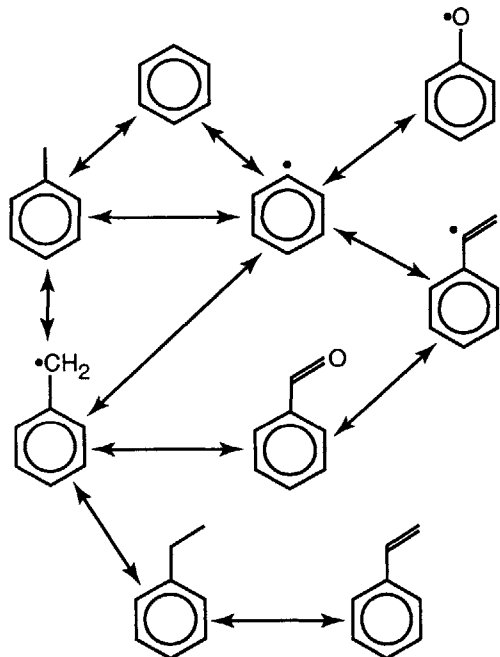
chemistry conditions, as opposed to combustion. Brezinsky and others have performed numerous mechanistic studies on toluene at combustion conditions; their work is more comparable to the situation observed in our experiments (Brezinsky, 1986; Emdee *et al.*, 1992; Davis *et al.*, 1996; Zeppieri, *et al.*, 1997). It was found under their experimental conditions (a flow reactor) that the benzyl radical ( $C_6H_5CH_2\bullet$ ) is the major intermediate in the side-chain chemistry of toluene. As has been observed in our experiments, Emdee *et al.* (1992) found that ring-breaking chemistry was of only minor importance in the early stages of toluene oxidation; instead, the reactions of the side group dominate. Emdee *et al.* also found cresols and benzyl alcohol to be important products of toluene oxidation, whereas neither of these species was observed in any of the experimental flames examined here; conversely, they find ethylbenzene to be a minor product only, while in the data presented in Chapter 9 it is the dominant product, and in some cases accounts for over 50 percent of the carbon input as toluene. This discrepancy could be due to the propane that makes up the majority of the fuel in these experiments; this should lead to an environment rich in ethyl radicals, which could enhance production of ethylbenzene and styrene through reaction with the phenyl radical.

Our work, and both of the mechanisms discussed above, all point to an important role for benzyl radical in the partial or full oxidation of toluene, despite the wide variations in experimental conditions. Thus, the simple mechanism discussed in the following section will be structured around this radical.

### 10.3 Proposed Mechanism of Toluene Partial Oxidation in the Quench Layer

Drawing inferences from the above work and the experimentally observed species profiles, the simplified mechanism for toluene oxidation in the pre-flame region that is outlined in Figure 10.1 can be proposed. It is essentially a two-step mechanism from toluene to several of the major products observed in the flame. The reaction pathway is initiated by the production of benzyl via reaction of toluene with any of a number of radical species (H, OH, H) or with molecular oxygen, and followed by combination reactions of benzyl with other radicals to create product molecules such as benzaldehyde and ethylbenzene. Note that benzofuran is not included

in this mechanism, as significantly less rate information is available for this particular species than for the others; given the limited purposes for which the model is intended, benzaldehyde may serve as a surrogate for both of the observed oxygenated quench zone products.



**Figure 10.1.** Simplified reaction mechanism for the partial oxidation of toluene in flame quench zones.

fuel in all cases considered here, the added heat release is relatively minor (on the order of 5 percent of the total), and the mechanism without ring oxidation is much less computationally demanding. A listing of reactions and rate coefficients for the mechanism is given in Table 10.1.

A reaction scheme for the mechanism shown in Figure 10.1 has been developed from the toluene oxidation submechanism of Emdee, Brezinsky and Glassman (1992). Reaction pathways from the original mechanism that were based on products not observed in our experiments were eliminated; the focus of the resulting mechanism is to capture the consumption of toluene and production of benzaldehyde. The mechanism does not include complete oxidation of the aromatic ring; since toluene represents only a small fraction of the

Reaction	A	b	E <sub>a</sub>
C <sub>6</sub> H <sub>5</sub> CH <sub>2</sub> + H = C <sub>6</sub> H <sub>5</sub> CH <sub>3</sub>	1.80E+14	0.00	0
C <sub>6</sub> H <sub>5</sub> CH <sub>3</sub> = C <sub>6</sub> H <sub>5</sub> + CH <sub>3</sub>	1.40E+16	0.00	99800
C <sub>6</sub> H <sub>5</sub> CH <sub>3</sub> + O <sub>2</sub> = C <sub>6</sub> H <sub>5</sub> CH <sub>2</sub> + HO <sub>2</sub>	3.00E+14	0.00	41400
C <sub>6</sub> H <sub>5</sub> CH <sub>3</sub> + OH = C <sub>6</sub> H <sub>5</sub> CH <sub>2</sub> + H <sub>2</sub> O	1.26E+13	0.00	2583
C <sub>6</sub> H <sub>5</sub> CH <sub>3</sub> + H = C <sub>6</sub> H <sub>5</sub> CH <sub>2</sub> + H <sub>2</sub>	1.20E+14	0.00	8235
C <sub>6</sub> H <sub>5</sub> CH <sub>3</sub> + H = C <sub>6</sub> H <sub>6</sub> + CH <sub>3</sub>	1.20E+13	0.00	5148
CH <sub>3</sub> + C <sub>6</sub> H <sub>5</sub> CH <sub>3</sub> = CH <sub>4</sub> + C <sub>6</sub> H <sub>5</sub> CH <sub>2</sub>	3.16E+11	0.00	9500
C <sub>6</sub> H <sub>5</sub> + C <sub>6</sub> H <sub>5</sub> CH <sub>3</sub> = C <sub>6</sub> H <sub>6</sub> + C <sub>6</sub> H <sub>5</sub> CH <sub>2</sub>	2.10E+12	0.00	4400
C <sub>6</sub> H <sub>5</sub> CH <sub>2</sub> + O = C <sub>6</sub> H <sub>5</sub> CHO + H	2.50E+14	0.00	0
C <sub>6</sub> H <sub>5</sub> CH <sub>2</sub> + O = C <sub>6</sub> H <sub>5</sub> + CH <sub>2</sub> O	8.00E+13	0.00	0
C <sub>6</sub> H <sub>5</sub> CH <sub>2</sub> + HO <sub>2</sub> = C <sub>6</sub> H <sub>5</sub> CHO + H + OH	2.50E+14	0.00	0
C <sub>6</sub> H <sub>5</sub> CH <sub>2</sub> + HO <sub>2</sub> = C <sub>6</sub> H <sub>5</sub> + CH <sub>2</sub> O + OH	8.00E+13	0.00	0
C <sub>6</sub> H <sub>5</sub> C <sub>2</sub> H <sub>5</sub> => C <sub>6</sub> H <sub>5</sub> CH <sub>2</sub> + CH <sub>3</sub>	2.00E+15	0.00	72700
C <sub>6</sub> H <sub>5</sub> CH <sub>2</sub> + CH <sub>3</sub> => C <sub>6</sub> H <sub>5</sub> C <sub>2</sub> H <sub>5</sub>	9.05E+06	1.49	-7160
C <sub>6</sub> H <sub>5</sub> CHO + O <sub>2</sub> = C <sub>6</sub> H <sub>5</sub> CO + HO <sub>2</sub>	1.02E+13	0.00	38950
C <sub>6</sub> H <sub>5</sub> CHO + OH = C <sub>6</sub> H <sub>5</sub> CO + H <sub>2</sub> O	1.71E+09	1.18	-447
C <sub>6</sub> H <sub>5</sub> CHO + H = C <sub>6</sub> H <sub>5</sub> CO + H <sub>2</sub>	5.00E+13	0.00	4928
C <sub>6</sub> H <sub>5</sub> CHO + H = C <sub>6</sub> H <sub>6</sub> + HCO	1.20E+13	0.00	5148
C <sub>6</sub> H <sub>5</sub> CHO + O = C <sub>6</sub> H <sub>5</sub> CO + OH	9.04E+12	0.00	3080
C <sub>6</sub> H <sub>5</sub> CH <sub>2</sub> + C <sub>6</sub> H <sub>5</sub> CHO = C <sub>6</sub> H <sub>5</sub> CH <sub>3</sub> + C <sub>6</sub> H <sub>5</sub> CO	2.77E+03	2.81	5773
CH <sub>3</sub> + C <sub>6</sub> H <sub>5</sub> CHO = CH <sub>4</sub> + C <sub>6</sub> H <sub>5</sub> CO	2.77E+03	2.81	5773
C <sub>6</sub> H <sub>5</sub> + C <sub>6</sub> H <sub>5</sub> CHO = C <sub>6</sub> H <sub>6</sub> + C <sub>6</sub> H <sub>5</sub> CO	7.01E+11	0.00	4400
C <sub>6</sub> H <sub>5</sub> C <sub>2</sub> H <sub>5</sub> + OH = C <sub>6</sub> H <sub>5</sub> C <sub>2</sub> H <sub>3</sub> + H <sub>2</sub> O + H	8.43E+12	0.00	2583
C <sub>6</sub> H <sub>5</sub> C <sub>2</sub> H <sub>5</sub> + H = C <sub>6</sub> H <sub>5</sub> C <sub>2</sub> H <sub>3</sub> + H <sub>2</sub> + H	8.00E+13	0.00	8235
C <sub>6</sub> H <sub>5</sub> C <sub>2</sub> H <sub>5</sub> + O <sub>2</sub> = C <sub>6</sub> H <sub>5</sub> C <sub>2</sub> H <sub>3</sub> + HO <sub>2</sub> + H	2.00E+14	0.00	41400
C <sub>6</sub> H <sub>5</sub> CO = C <sub>6</sub> H <sub>5</sub> + CO	3.98E+14	0.00	29400
C <sub>6</sub> H <sub>5</sub> + H = C <sub>6</sub> H <sub>6</sub>	2.20E+14	0.00	0
C <sub>6</sub> H <sub>6</sub> + O <sub>2</sub> = C <sub>6</sub> H <sub>5</sub> + HO <sub>2</sub>	6.30E+13	0.00	60000
C <sub>6</sub> H <sub>6</sub> + OH = C <sub>6</sub> H <sub>5</sub> + H <sub>2</sub> O	2.11E+13	0.00	4570
C <sub>6</sub> H <sub>6</sub> + O = C <sub>6</sub> H <sub>5</sub> O + H	2.78E+13	0.00	4910
C <sub>6</sub> H <sub>6</sub> + H = C <sub>6</sub> H <sub>5</sub> + H <sub>2</sub>	2.50E+14	0.00	16000
C <sub>6</sub> H <sub>5</sub> + O <sub>2</sub> = C <sub>6</sub> H <sub>5</sub> O + O	2.09E+12	0.00	7470
C <sub>6</sub> H <sub>5</sub> O = CO + C <sub>5</sub> H <sub>5</sub>	2.51E+11	0.00	43900

**Table 10.1** Reactions and rate coefficients for the mechanism shown in Figure 10.1. (Subset of Emdee, Brezinsky and Glassman, 1992). Units of A are moles, seconds, cm and K, depending on the reaction stoichiometry; E<sub>a</sub> units are cal/mole. Reaction rates are calculated as in Equation 4.2.

#### 10.4 Numerical Simulation of Toluene Partial Oxidation in Propane Flames

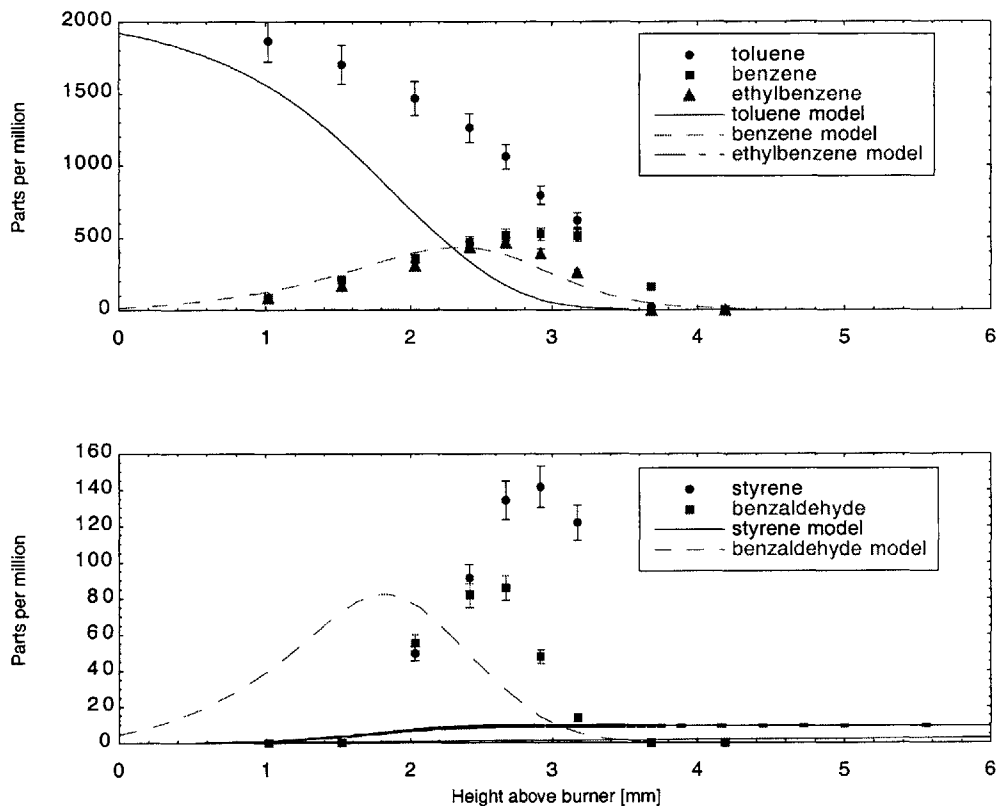
In order to validate the mechanism of Table 10.1, it was used in conjunction with the propane oxidation mechanism of Dagaut *et al.* (1992), which showed good agreement with measured propane-air flame profiles (see Chapter 8), to model one of the experimental flames



presented in Chapter 9. The stoichiometric flame (equivalence ratio  $\phi = 1$ ) was chosen as the test case.

The PREMIX steady-state modeling code was again used to simulate the burner flame, with a temperature profile specified from the experiment (Kee *et al.*, 1985). The input conditions were determined from the  $\phi = 1.0$  flame; specifically, a toluene to propane ratio of 10% by carbon, overall equivalence ratio of one, unburned gas flow of 180 mg/s ( $3.6 \text{ mg/cm}^2/\text{s}$ ), and burner surface temperature of  $70^\circ\text{C}$ .

Figure 10.2 shows some selected species profiles from the simulation result, compared with the measured experimental values. The agreement for toluene decay and benzaldehyde formation is fairly good, although some offsets are observed; it has been noted previously that the mechanism from which rate constants were obtained has some difficulty predicting burner flame profiles with extreme accuracy, so this level of agreement seems sufficient (Davis *et al.*, 1989).



**Figure 10.2.** Comparison of measured and calculated toluene partial oxidation product concentrations in a toluene-doped propane-air burner flame, with toluene at 10 percent by carbon,  $\phi = 1.0$ , and unburned gas flow of  $3.6 \text{ mg/m}^2/\text{s}$ .

Benzene is also predicted fairly well, although again with some offset. The predicted levels of ethylbenzene and styrene are extremely low compared to the experimental values; as mentioned above, ethyl radicals produced from propane could contribute significantly to the production of these two species.

From the numerical results, we can calculate directly the boundary fluxes that were estimated for the experimental concentration profiles using equation 9.3. The numerical simulation predicts a wall flux of  $-5.6\text{E-}7$  moles/m<sup>2</sup>/s for benzaldehyde; which is only a factor of two different from the estimated value of  $-2.8\text{E-}7$  moles/m<sup>2</sup>/s (see Figure 9.11).

While this mechanism is far from being a precise predictive tool, the general agreement of the toluene and benzaldehyde profiles (particularly the good agreement of the peak value of the benzaldehyde concentration profile), as well as the benzaldehyde wall flux, suggests that it can be a useful tool for simulating realistic quench layer deposit precursor formation chemistry in conjunction with the numerical model.

### 10.5 Simulated Deposition with Toluene Fuel

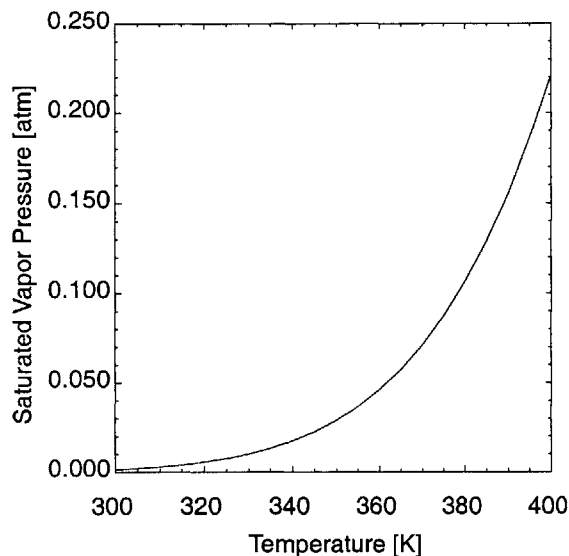
The mechanism presented above provides a reasonable simulation of the production of benzaldehyde from toluene in the flame. Since benzaldehyde is one of the most likely deposit precursors observed in the experiments, the next step is to use this mechanism with the numerical model to evaluate the likelihood that benzaldehyde does act as a deposit precursor; given these kinetics, is it possible for benzaldehyde formed from toluene in the flame quench process to deposit on the wall surface?

As part of this evaluation, we again use as a reference the results of Price *et al.* (1995) in their quenched flame deposition apparatus. In their experiments, deposition was observed from quenching of toluene-doped propane flames. The maximum deposition of approximately 200 milligrams of deposit per mole of toluene (a deposit mass fraction of 0.002) was observed at the highest input toluene mole fraction of 0.01; we will use this amount of toluene as the initial condition for the simulations. It should be noted here that the goal of this simulation is not to model the results of Price *et al.*, or to predict deposition rates from toluene fuel; rather, it is to use

the chemical mechanism derived above under conditions in which toluene is known to cause deposition in order to gain insight into the role of benzaldehyde as a potential deposit precursor.

The chemical mechanism used is based on the reduced ethylene oxidation mechanism listed in Appendix I, which is much less computationally intensive than the propane oxidation mechanism used above, and sufficient for the approximate nature of these simulations. The reactions from Table 10.1 are added to this mechanism to provide for production of benzaldehyde (and other species) from toluene.

The boundary condition for benzaldehyde deposition is based on its saturation vapor pressure, using a vapor-liquid equilibrium assumption; if the partial pressure of benzaldehyde at the wall surface exceeds the saturated vapor pressure, condensation occurs to lower the partial pressure to the vapor pressure. The variation of the saturated vapor pressure of benzaldehyde with temperature is shown in Figure 10.3 (Stull, 1947). Since deposition rates from benzaldehyde should be low, evaporation from the surface is only allowed if condensation has occurred previously (*i.e.* it is assumed that there is no condensed benzaldehyde on the wall at the beginning of the simulation).

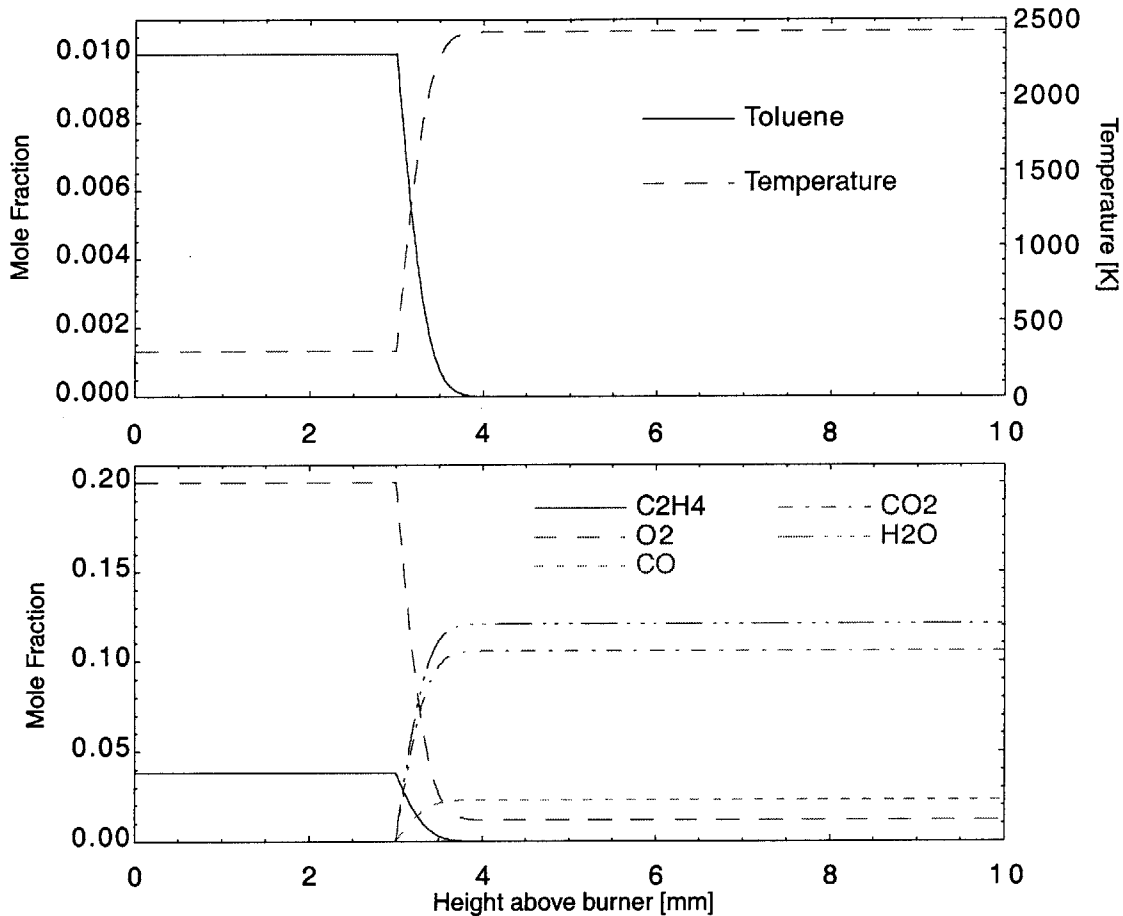


**Figure 10.3.** Saturated vapor pressure of benzaldehyde as a function of temperature (Stull, 1947).

mm from the wall; equilibrium combustion products are used for the mixture composition behind the flame front. The initial shape of the flame front is unimportant, as the profiles relax to a

The simulations were performed for three initial conditions, to indicate the strong effect of wall temperature; wall surface temperatures were fixed at 300 K, 320 K, and 340 K. The apparatus in which Price *et al.* (1995) observed deposition used a wall temperature of 340 K. An example of the initial condition is shown in Figure 10.4. Unburned gas mixture is between the wall surface and the flame front, which is located at approximately 3

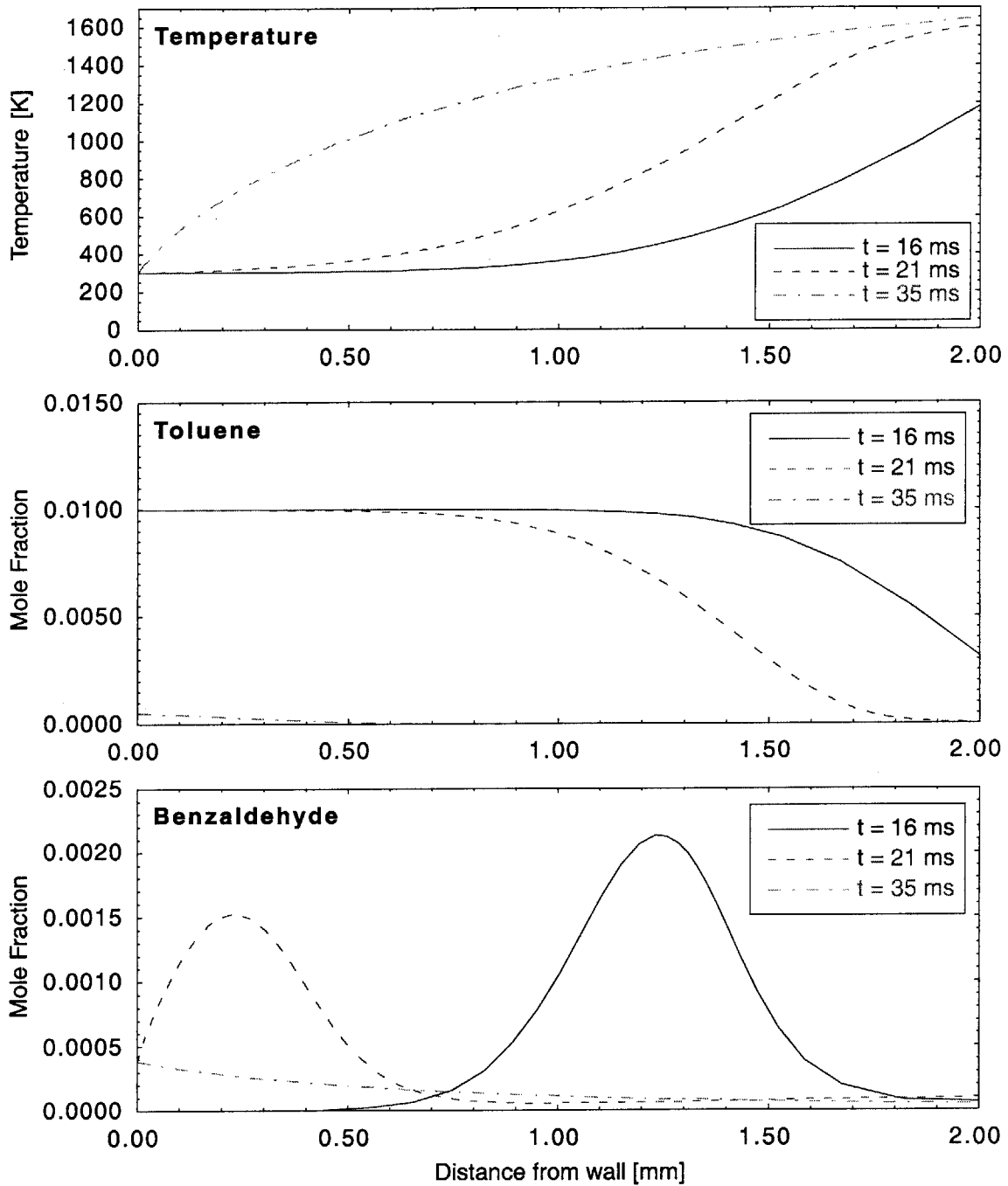
physically reasonable flame during the first few timesteps of the simulation, before the flame begins to reach the wall surface.



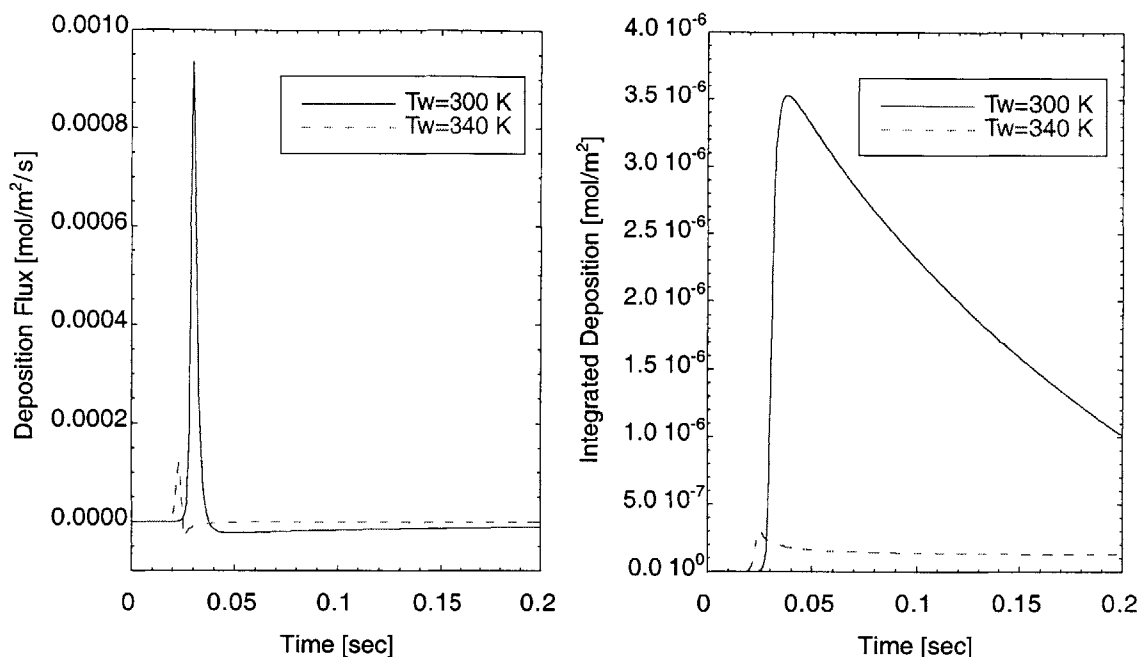
**Figure 10.4.** Initial condition for simulation of flame quenching and deposition with toluene / benzaldehyde chemistry.

Results of the three simulations are presented in Figures 10.5 and 10.6. Figure 10.5 shows the time evolution of toluene, benzaldehyde and temperature profiles during the flame propagation and quenching for the 300 K wall temperature case. The benzaldehyde concentration at the wall is barely able to exceed the saturated vapor pressure under these conditions. This results in a strong competition between deposition and oxidation; as the latter rapidly consumes the benzaldehyde near the wall during the time available for deposition. Figure 10.6 shows deposition rates and integrated deposition amounts for high and low wall temperature cases. While a small amount of deposition is observed in the 300 K wall temperature case, this

decreases rapidly with increasing temperature, and no deposition is observed for a wall temperature of 340 K.



**Figure 10.5.** Time evolution of toluene, benzaldehyde and temperature profiles during a flame quench event at a wall temperature of 300 K.



**Figure 10.6.** Calculated deposition fluxes and integrated deposition amounts for benzaldehyde as a function of wall surface temperature. The deposition for the  $T_w = 340$  K case is within the numerical error.

This leads to several conclusions regarding the deposition process for toluene fuel. First, it is highly unlikely that the species observed in the burner experiments (benzaldehyde, benzofuran, etc.) cause deposition via condensation at engine conditions; 340 K would be a relatively low surface temperature in the engine cylinder, and yet it is too high for these species to condense based on their formation rates from toluene. Although pressures are higher in the engine environment (up to 20 atm), this has a linear effect on the species partial pressures, as opposed to the exponential effect of wall temperature on the saturated vapor pressures, and hence is not likely to be sufficient to drive deposition by condensation. Since deposition is observed from toluene fuel under similar conditions to those modeled here (Price *et al.*, 1995), we must consider other means by which that deposition could take place. It is possible that chemical pathways and precursor species that are not observed at our experimental conditions may be more prevalent at the conditions modeled here, and at which deposition is observed. If this is the case, species of significantly lower volatilities than benzaldehyde would need to be produced to act as deposit precursors (for example, by addition of oxygen to the aromatic ring of toluene). Another possibility is that adsorption processes are important means of deposition at the wall surface. Adsorption kinetics and equilibria are not necessarily related to the species volatility, and hence

could provide a path for deposition of species like benzaldehyde despite the high wall temperatures. However, it should be noted that adsorption would not easily account for the exponential dependence of deposition on fuel boiling point that has often been observed (Shore and Ockert, 1958; Price *et al.*, 1995).

## 10.6 Conclusions

The analysis presented in this chapter has demonstrated the possibility of determining useful chemical reaction mechanisms related to deposit precursor formation via the species concentration profile data taken in the experimental burner. Even a very simple mechanism for partial oxidation of toluene, with a single radical intermediate, showed relatively close agreement with measured species profiles (of course, the availability of good reaction rate data was crucial to this process). Using such mechanisms in conjunction with the numerical model, it is possible to evaluate the ability of experimentally observed species to act as deposit precursors under realistic conditions.

Some direct conclusions about the toluene system can be made based on this analysis. Toluene does produce partially oxidized derivatives with relatively high boiling points that are transported to the wall surface by diffusion and flame motion. However, the saturated vapor pressures of the observed toluene derivatives are high enough that a pure condensation boundary condition will not be sufficient to allow significant deposition of these species, especially at higher wall temperatures; either some sort of chemisorption or physisorption must be assumed, or the involvement of reaction pathways and/or precursor species that were not observed under our experimental conditions.

## 10.7 References

K. Brezinsky, *Progress in Energy and Combustion Science*, Vol. 12, 1 (1986).

P. Dagaut, M. Cathonnet, and J-C. Boettner, "Kinetic Modeling of Propane Oxidation and Pyrolysis," *International Journal of Chemical Kinetics*, Vol. 25, 813-837 (1992).

- S. Davis, H. Wang, K. Brezinsky and C.K. Law, "Laminar Flame Speeds and Oxidation Kinetics of Benzene-Air and Toluene-Air Flames," *26<sup>th</sup> Symposium (International) on Combustion [Proceedings]*, 1063 (1989).
- J.L. Emdee, K. Brezinsky, and I. Glassman, "A Kinetic Model for the Oxidation of Toluene near 1200 K," *Journal of Physical Chemistry*, Vol. 96, 2151-2161 (1992).
- R.J. Kee, J.F. Grcar, M.D. Smooke, and J.A. Miller, "A FORTRAN Program for Modeling Steady Laminar One-Dimensional Premixed Flames," *Sandia National Laboratories Report SAND85-8240* (1985).
- R.J. Price, J.P.T. Wilkinson, D.A.J. Jones, and C. Morley, "A Laboratory Simulation and Mechanism for the Fuel Dependence of SI Combustion Chamber Deposit Formation," *Society of Automotive Engineers* 952445 (1995).
- R. Seuwen and P. Warneck, "Oxidation of Toluene in NO<sub>x</sub> Free Air: Product Distribution and Mechanism," *International Journal of Chemical Kinetics*, Vol. 28, 315-332 (1996).
- D.R. Stull, "Vapor Pressure of Pure Substances: Organic Compounds," *Industrial and Engineering Chemistry*, Vol. 39, 517-540 (1947).
- S. Zeppieri, K. Brezinsky, and I. Glassman, "Pyrolysis Studies of Methylcyclohexane and Oxidation Studies of Methylcyclohexane and Methylcyclohexane/Toluene Blends," *Combustion and Flame* **108**, 266-286 (1997).



### **11.1 Introduction**

The conclusions and comments below are divided into four sections: direct conclusions from the experimental results, conclusions derived from the combination of experimental inferences and numerical modeling, a discussion of the merits and difficulties of the joint numerical-experimental method employed in this work, and suggestions for future work and extensions to the project. It should be kept in mind that, while interesting information about the formation mechanisms of combustion chamber deposits has been derived from the experimental and numerical work presented in this thesis, an equally important goal of the project has been to determine the feasibility of applying fundamental flame chemistry experiments to such a complex practical problem in a useful manner. Hence, the conclusions from the experimental and numerical results, which can be found in detail in earlier chapters, are briefly summarized here, while their implications for the methodology and future studies are discussed in greater detail.

### **11.2 Experimental Conclusions**

The results of the flat flame burner experiments are able to address a number of the questions outlined at the start of this work. Potential deposit precursor species have been directly identified in the pre-flame zone of the cooled burner flames; for toluene fuel, some candidates are benzaldehyde, styrene and benzofuran. Also, oxygen addition in the gas phase has been observed; if species such as benzaldehyde are in fact depositing at the wall surface, the oxygen that they carry in their structure would be sufficient to supply the majority of the oxygen mass found in the final deposit. These results support the hypothesis that depositing species are produced from fuel and air in the flame quench zone via partial oxidation reactions.

The identification of partial oxidation products of toluene in the pre-flame region, along with measurements of their concentration profiles, provides sufficient information to construct a simplified mechanism of deposit precursor formation from toluene that shows promising ability to reproduce experimentally measured species profiles. In the range of conditions studied, there

was little discernible effect of overall equivalence ratio on the quench layer chemistry. As the range of equivalence ratios examined so far is relatively small, a broader study in this area would be necessary to determine the full effect of this important parameter.

### 11.3 Numerical Analysis Conclusions

Even without a detailed precursor formation mechanism, the numerical model was able to provide insights into the interactions of transport and condensation processes during deposition events. Using simulated precursor species to model a range of fuel component volatilities, the numerical model was able to reproduce trends with fuel component boiling points and amounts of deposit-forming species in the fuel mixture that were observed experimentally by other researchers. In this case, a simple condensation-evaporation condition at the wall surface was sufficient to reproduce all the observed behavior.

In conjunction with the precursor formation mechanism developed from the experimental results, the numerical model was used to examine the interactions between reaction, transport and deposition for quenching flames containing toluene. It was found that, while the precursor candidate molecules benzaldehyde and styrene were produced in the flame and transported to the wall surface, the gas-phase formation rate of these species was insufficient to produce high enough partial pressures for significant condensation. Thus, while species are produced that could condense on the wall in some situations, it appears that a stronger deposition mechanism such as chemisorption or physisorption would be required for styrene or benzaldehyde to act as deposit precursors at realistic engine surface temperatures. For less volatile fuel components (multi-ring aromatics, for example), chemical mechanisms similar to those observed here could lead to formation of deposits by condensation alone at engine conditions. However, as single-ring aromatics are known to cause significant deposition, and ring-building chemistry was not observed in these experiments, simple condensation as the main mechanism for deposition at the engine wall is not supported by these results. Nevertheless, it is not possible to rule out condensation as a major deposition mechanism, since there is a good possibility that different

chemical mechanisms may be prevalent at engine pressures, leading to product species of lower volatility than those observed in these low-pressure experiments.

#### 11.4 Comments on Methodology

One of the most important aspects of this study has been the development of the project methodology. The goal was to investigate the fundamental gas-phase chemical and physical processes that lead to the formation of chemical species capable of deposition at the engine wall through direct experimental measurements, while remaining relevant to the high-pressure, transient conditions that characterize the flame quenching and deposition processes in engines. With this in mind, the following discussion outlines some of the benefits and shortcomings of the numerical-experimental method employed in this study.

The methods used for this work have been able to produce results that provide unique contributions to the study of combustion chamber deposits. The direct identification of possible precursor species provides a concrete basis for discussion of the chemical production, transport and deposition processes involved in deposit formation; the use of these precursor candidates in the numerical model, with appropriate chemical mechanisms, allows the interactions between these processes to be examined quantitatively at more practical conditions. An important benefit of the numerical analysis is that trends may be examined critically and provide useful information even without exact chemical mechanisms. This is extremely helpful in framing questions to address in further experimental analysis and mechanism development (for example: are there major changes in product distribution, corresponding to activation of alternate chemical reaction pathways, at higher operating pressures?) There are a number of key variables that can be studied with this technique, including equivalence ratio, flame heat loss to the surface, and chemical structure of the dopant, among others.

There are also some clear difficulties inherent in this method. Chief among these is the effect of pressure on chemical reaction rates and reaction mechanisms. As mentioned above, the chemical mechanisms that dominate at experimental conditions may be different from those that are most active at engine conditions. However, as measurements of this sort are currently

impractical at high pressures, this strategy, while fundamentally indirect, is still a useful way to observe chemistry effects and precursor formation mechanisms, which otherwise would not be possible at all. An additional drawback to the methods used in this work is that the important heterogeneous processes of deposition cannot be directly studied via the experimental results, as flow conditions at the burner surface are significantly different from those at engine cylinder surfaces.

### 11.5 Future Directions

In this thesis, a novel method for the investigation of the fundamental mechanisms of combustion chamber deposit formation has been developed. As such, there are numerous possibilities for extensions of the work described in this thesis, as well as for related research directions; the laboratory facilities, diagnostic methods, and numerical tools described here may be used to investigate a wide range of questions in the area of deposit formation.

The clearest avenue on which to proceed with this work is to continue the investigations of precursor formation chemistry via single-component doping of propane-air flames. One of the first effects to consider should be the impact of equivalence ratio. As noted above, no major trends with overall equivalence ratio were observed in the limited number of experiments performed for this thesis. However, as it is known that the equivalence ratio strongly affects engine deposits, and not solely through thermal interactions, a detailed study of changes in precursor formation chemistry over a broad range of equivalence ratios could provide important insights into the role of oxygen in the precursor or deposit formation process.

A number of other directions may be pursued using this methodology. On the experimental front, the effects of dopants from different chemical families, dopant concentrations, burner surface temperature and heat loss from the flame to the burner surface, gas flow velocities, and operating pressures should be examined. In addition to these extensions of the parameter space, some alterations to the analysis procedure could be helpful. Through modifications to the gas chromatography methods, the unresolved non-aromatic hydrocarbons in the flame samples could be separated, identified and quantified, which would provide important information for

mechanism development. Also, by increasing sample collection time for the adsorption traps, lower concentration levels of most species could be resolved, allowing more accurate determination of concentration gradients and species fluxes near the burner surface.

There are also further directions to pursue with the numerical analysis. As the current results do not support condensation as the deposition mechanism with the observed precursor candidate species, it would be very useful to model alternative deposition boundary conditions, such as heterogeneous reaction or adsorption. Such a model could be as simple as an assumption of complete adsorption of any precursor species molecules that reach the surface, or could account for adsorption kinetics with appropriate adsorption isotherms. A comparison between results produced with different deposition boundary conditions could be very informative. Another informative use of the numerical model would be the simulation of additional reaction pathways known to occur in toluene oxidation under higher pressure conditions, which would allow one to consider whether these chemical mechanisms would be likely to contribute enough to precursor formation to make condensation a viable deposition mechanism.

## 11.6 Summary

This thesis, like most research works, has raised more questions than it answered. If species like benzaldehyde are deposit precursors, what type of deposition process can account for reported deposition rates at engine temperatures? Are chemical mechanisms other than those observed in the experiments important in engine deposition, and if so, at what pressures do their effects become significant? Is there an effect of overall equivalence ratio on the formation chemistry of deposit precursors? However, in the process, the background information and analytical tools to frame these questions well and begin to address them have been provided. Future work in this area could be a very productive addition to the field of combustion chamber deposit study, filling a gap in the current array of research methods and providing a new perspective on many of the issues in this complex problem.



*Simplified Hydrocarbon Combustion and Deposit Formation Mechanism***I.1 Introduction**

The mechanism listed in this appendix is based on the reduced mechanism for alkane combustion of Griffiths, *et al.* (1995). The majority of the rate expressions are taken from the GRI-MECH ethylene oxidation mechanism (Bowman *et al.*, 1995); thermodynamic data is from the CHEMKIN thermodynamic database (Kee *et al.*, 1990), using polynomial fits to thermodynamic properties in the NASA polynomial format (Burcat, 1984).

**I.2 Ethylene Oxidation Mechanism**

The following is the complete mechanism, in CHEMKIN-II format, including the elements and chemical species considered, thermodynamic data in NASA polynomial format, reactions and reaction rate coefficients:

```

ELEMENTS
O H C N
END
SPECIES
H2 H O O2 OH
H2O HO2 H2O2 CO CO2
HCO CH2O CH3 C2H3 C2H4
C2H5 N2 C7H8 CO
END
THERMO ALL
300.0 1000.0 5000.0
H2 TPIS78H 2 00 00 00G 200.000 3500.000 1000.000 1
3.33727920E+00 -4.94024731E-05 4.99456778E-07 -1.79566394E-10 2.00255376E-14 2
-9.50158922E+02 -3.20502331E+00 2.34433112E+00 7.98052075E-03 -1.94781510E-05 3
2.01572094E-08 -7.37611761E-12 -9.17935173E+02 6.83010238E-01 8.46810200E+03 4
H L 7/88H 1 00 00 00G 200.000 3500.000 1000.000 1
2.50000001E+00 -2.30842973E-11 1.61561948E-14 -4.73515235E-18 4.98197357E-22 2
2.54736599E+04 -4.46682914E-01 2.50000000E+00 7.05332819E-13 -1.99591964E-15 3
2.30081632E-18 -9.27732332E-22 2.54736599E+04 -4.46682853E-01 6.19742800E+03 4
O L 1/90O 1 00 00 00G 200.000 3500.000 1000.000 1
2.56942078E+00 -8.59741137E-05 4.19484589E-08 -1.00177799E-11 1.22833691E-15 2
2.92175791E+04 4.78433864E+00 3.16826710E+00 -3.27931884E-03 6.64306396E-06 3
-6.12806624E-09 2.11265971E-12 2.91222592E+04 2.05193346E+00 6.72540300E+03 4
O2 TPIS89O 2 00 00 00G 200.000 3500.000 1000.000 1
3.28253784E+00 1.48308754E-03 -7.57966669E-07 2.09470555E-10 -2.16717794E-14 2
-1.08845772E+03 5.45323129E+00 3.78245636E+00 -2.99673416E-03 9.84730201E-06 3
-9.68129509E-09 3.24372837E-12 -1.06394356E+03 3.65767573E+00 8.68010400E+03 4
OH RUS 78O 1H 1 00 00G 200.000 3500.000 1000.000 1
3.09288767E+00 5.48429716E-04 1.26505228E-07 -8.79461556E-11 1.17412376E-14 2
3.85865700E+03 4.47669610E+00 3.99201543E+00 -2.40131752E-03 4.61793841E-06 3
-3.88113333E-09 1.36411470E-12 3.61508056E+03 -1.03925458E-01 8.81310600E+03 4
H2O L 8/89H 2O 1 00 00G 200.000 3500.000 1000.000 1
3.03399249E+00 2.17691804E-03 -1.64072518E-07 -9.70419870E-11 1.68200992E-14 2
-3.00042971E+04 4.96677010E+00 4.19864056E+00 -2.03643410E-03 6.52040211E-06 3

```

-5.48797062E-09	1.77197817E-12	-3.02937267E+04	-8.49032208E-01	9.90409200E+03	4
HO2	L 5/89H	1O	2	00 00G	200.000 3500.000 1000.000
4.01721090E+00	2.23982013E-03	-6.33658150E-07	1.14246370E-10	-1.07908535E-14	2
1.11856713E+02	3.78510215E+00	4.30179801E+00	-4.74912051E-03	2.11582891E-05	3
-2.42763894E-08	9.29225124E-12	2.94808040E+02	3.71666245E+00	1.00021620E+04	4
H2O2	L 7/88H	2O	2	00 00G	200.000 3500.000 1000.000
4.16500285E+00	4.90831694E-03	-1.90139225E-06	3.71185986E-10	-2.87908305E-14	2
-1.78617877E+04	2.91615662E+00	4.27611269E+00	-5.42822417E-04	1.67335701E-05	3
-2.15770813E-08	8.62454363E-12	-1.77025821E+04	3.43505074E+00	1.11588350E+04	4
CO	TPIS79C	1O	1	00 00G	200.000 3500.000 1000.000
2.71518561E+00	2.06252743E-03	-9.98825771E-07	2.30053008E-10	-2.03647716E-14	2
-1.41518724E+04	7.81868772E+00	3.57953347E+00	-6.10353680E-04	1.01681433E-06	3
9.07005884E-10	-9.04424499E-13	-1.43440860E+04	3.50840928E+00	8.67100000E+03	4
CO2	L 7/88C	1O	2	00 00G	200.000 3500.000 1000.000
3.85746029E+00	4.41437026E-03	-2.21481404E-06	5.23490188E-10	-4.72084164E-14	2
-4.87591660E+04	2.27163806E+00	2.35677352E+00	8.98459677E-03	-7.12356269E-06	3
2.45919022E-09	-1.43699548E-13	-4.83719697E+04	9.90105222E+00	9.36546900E+03	4
HCO	L12/89H	1C	1O	1 00G	200.000 3500.000 1000.000
2.77217438E+00	4.95695526E-03	-2.48445613E-06	5.89161778E-10	-5.33508711E-14	2
4.01191815E+03	9.79834492E+00	4.22118584E+00	-3.24392532E-03	1.37799446E-05	3
-1.33144093E-08	4.33768865E-12	3.83956496E+03	3.39437243E+00	9.98945000E+03	4
CH2O	L 8/88H	2C	1O	1 00G	200.000 3500.000 1000.000
1.76069008E+00	9.20000082E-03	-4.42258813E-06	1.00641212E-09	-8.83855640E-14	2
-1.39958323E+04	1.36563230E+01	4.79372315E+00	-9.90833369E-03	3.73220008E-05	3
-3.79285261E-08	1.31772652E-11	-1.43089567E+04	6.02812900E-01	1.00197170E+04	4
CH3	L11/89C	1H	3	00 00G	200.000 3500.000 1000.000
2.28571772E+00	7.23990037E-03	-2.98714348E-06	5.95684644E-10	-4.67154394E-14	2
1.67755843E+04	8.48007179E+00	3.67359040E+00	2.01095175E-03	5.73021856E-06	3
-6.87117425E-09	2.54385734E-12	1.64449988E+04	1.60456433E+00	1.03663400E+04	4
C2H3	L 2/92C	2H	3	00 00G	200.000 3500.000 1000.000
3.01672400E+00	1.03302292E-02	-4.68082349E-06	1.01763288E-09	-8.62607041E-14	2
3.46128739E+04	7.78732378E+00	3.21246645E+00	1.51479162E-03	2.59209412E-05	3
-3.57657847E-08	1.47150873E-11	3.48598468E+04	8.51054025E+00	1.05750490E+04	4
C2H4	L 1/91C	2H	4	00 00G	200.000 3500.000 1000.000
2.03611116E+00	1.46454151E-02	-6.71077915E-06	1.47222923E-09	-1.25706061E-13	2
4.93988614E+03	1.03053693E+01	3.95920148E+00	-7.57052247E-03	5.70990292E-05	3
-6.91588753E-08	2.69884373E-11	5.08977593E+03	4.09733096E+00	1.05186890E+04	4
C2H5	L12/92C	2H	5	00 00G	200.000 3500.000 1000.000
1.95465642E+00	1.73972722E-02	-7.98206668E-06	1.75217689E-09	-1.49641576E-13	2
1.28575200E+04	1.34624343E+01	4.30646568E+00	-4.18658892E-03	4.97142807E-05	3
-5.99126606E-08	2.30509004E-11	1.28416265E+04	4.70720924E+00	1.21852440E+04	4
N2	121286N	2		G	300.000 5000.000 1000.000
0.02926640E+02	0.14879768E-02	-0.05684760E-05	0.10097038E-09	-0.06753351E-13	2
-0.09227977E+04	0.05980528E+02	0.03298677E+02	0.14082404E-02	-0.03963222E-04	3
0.05641515E-07	-0.02444854E-10	-0.10208999E+04	0.03950372E+02		4
! The following are surrogate deposit former and deposit precursor species, ! based on toluene					
C7H8	V06/92C	7H	8	G	0300.00 5000.00 1399.00
1.74312011E+01	2.01275750E-02	-6.68039086E-06	1.01501587E-09	-5.79660539E-14	2
-8.10171145E+02	-6.80780500E+01	1.34267628E+01	2.83327620E-02	-1.40926934E-05	3
4.63091379E-09	-8.06631925E-13	8.67338257E+02	-4.58805156E+01		4
CCD	V06/92C	7H	8	G	0300.00 5000.00 1399.00
1.74312011E+01	2.01275750E-02	-6.68039086E-06	1.01501587E-09	-5.79660539E-14	2



```

-8.10171145E+02-6.80780500E+01 1.34267628E+01 2.83327620E-02-1.40926934E-05 3
4.63091379E-09-8.06631925E-13 8.67338257E+02-4.58805156E+01 4
END
REACTIONS
O+H2<=>H+OH 5.000E+04 2.670 6290.00
2H+M<=>H2+M 1.000E+18 -1.000 .00
H2/ .00/ H2O/ .00/ CO2/ .00/
2H+H2<=>2H2 9.000E+16 -.600 .00
2H+H2O<=>H2+H2O 6.000E+19 -1.250 .00
H+O2<=>O+OH 8.300E+13 .000 14413.00
2OH<=>O+H2O 3.570E+04 2.400 -2110.00
H+O2+M<=>HO2+M 2.800E+18 -.860 .00
O2/ .00/ H2O/ .00/ CO/ .75/ CO2/1.50/ N2/ .00/
OH+HO2<=>O2+H2O 2.900E+13 .000 -500.00
2HO2<=>O2+H2O2 1.300E+11 .000 -1630.00
DUPLICATE
2HO2<=>O2+H2O2 4.200E+14 .000 12000.00
DUPLICATE
2OH(+M) <=>H2O2(+M) 7.400E+13 -.370 .00
LOW / 2.300E+18 -.900 -1700.00/
TPOE/ .7346 94.00 1756.00 5182.00 /
H2/2.00/ H2O/6.00/ CO/1.50/ CO2/2.00/
H+OH+M<=>H2O+M 2.200E+22 -2.000 .00
H2/ .73/ H2O/3.65/
2O+M<=>O2+M 1.200E+17 -1.000 .00
H2/ 2.40/ H2O/15.40/ CO/ 1.75/ CO2/ 3.60/
OH+CO<=>H+CO2 4.760E+07 1.228 70.00
HO2+CO<=>OH+CO2 1.500E+14 .000 23600.00
O+CO+M<=>CO2+M 6.020E+14 .000 3000.00
H2/2.00/ O2/6.00/ H2O/6.00/ CO/1.50/ CO2/3.50/
HCO+O2<=>HO2+CO 7.600E+12 .000 400.00
HCO+M<=>H+CO+M 1.870E+17 -1.000 17000.00
H2/2.00/ H2O/ .00/ CO/1.50/ CO2/2.00/
O+CH2O<=>OH+HCO 3.900E+13 .000 3540.00
OH+CH2O<=>HCO+H2O 3.430E+09 1.180 -447.00
HO2+CH2O<=>HCO+H2O2 1.000E+12 .000 8000.00
O2+CH2O<=>HO2+HCO 1.000E+14 .000 40000.00
CH3+O2<=>OH+CH2O 3.600E+10 .000 8940.00
C2H3+O2<=>HCO+CH2O 3.980E+12 .000 -240.00
OH+C2H4<=>C2H3+H2O 3.600E+06 2.000 2500.00
C2H5+O2<=>HO2+C2H4 8.400E+11 .000 3875.00
O+C2H4<=>CH3+HCO 1.920E+07 1.830 220.00
C7H8=>CCD 1.000E+12 0.000 100000.00
END

```

### I.3 References

- A. Burcat, "Thermochemical Data for Combustion Calculations," in W.C. Gardiner, ed., Combustion Chemistry, Springer-Verlag (1984).
- C.T. Bowman, R.K. Hanson, D.F. Davidson, W.C. Gardiner, Jr., V. Lissianski, G.P. Smith, D. Golden, M. Frenklach, M. Goldenberg, "GRI-MECH Version 2.11," [http://www.me.berkeley.edu/gri\\_mech](http://www.me.berkeley.edu/gri_mech) (1995).
- J.F. Griffiths, K.J. Hughes, M. Schreiber and C. Poppe, "A Unified Approach to the Reduced Kinetic Modeling of Alkane Combustion," *Combustion and Flame*, Vol. 99, 533-540 (1995).
- R.J. Kee, F.M. Rupley, and J.A. Miller, "The CHEMKIN Thermodynamic Data Base," Sandia National Laboratories Report SAND87-8215B (1990).

Appendix II  
Propane Oxidation Mechanism

## II.1 Introduction

This mechanism for oxidation of propane is taken directly from the work of Dagaut, *et al.* (1991, 1992). Thermodynamic data is from the CHEMKIN thermodynamic database (Kee *et al.*, 1990), using polynomial fits to thermodynamic properties in the NASA polynomial format (Burcat, 1984).

## II.2 Propane Oxidation Mechanism

The following is the complete mechanism, in CHEMKIN-II format, including the elements and chemical species considered, thermodynamic data in NASA polynomial format, reactions and reaction rate coefficients:

```

ELEMENTS
C H O N
END
SPECIES
H      OH      HO2     H2      H2O     H2O2    N2      O       O2
CH     HCO     CH2     CH2O    CH3     CH2OH   CH3O    CH4     CH3OH   CO      CO2
C2H    HCCO    C2H2    CH2CO   C2H3    C2H4    CH3CHO  C2H4O   C2H5    C2H6
C3H3   AC3H4   PC3H4   AC3H5   SC3H5   TC3H5   C3H6    C3H6O   IC3H7   NC3H7   C3H8
C4H    C4H2    C4H3    C4H6    C4H7    PC4H8   TRAC4H8
END
THERMO ALL
300.000 1000.000 5000.000
H      KEE87H  1      G  0300.00  5000.00  1000.00  1
  0.025000000E+02  0.000000000E+00  0.000000000E+00  0.000000000E+00  0.000000000E+00  0.000000000E+00  2
  0.02547162E+06-0.04601176E+01  0.025000000E+02  0.000000000E+00  0.000000000E+00  0.000000000E+00  3
  0.000000000E+00  0.000000000E+00  0.02547162E+06-0.04601176E+01  4
OH     KEE87O  1H    1      G  0300.00  5000.00  1000.00  1
  0.02882730E+02  0.10139743E-02-0.02276877E-05  0.02174683E-09-0.05126305E-14  2
  0.03886888E+05  0.05595712E+02  0.03637266E+02  0.01850910E-02-0.16761646E-05  3
  0.02387202E-07-0.08431442E-11  0.03606781E+05  0.13588605E+01  4
HO2    KEE87H  1O    2      G  0300.00  5000.00  1000.00  1
  4.07219124E+00  2.13129632E-03-5.30814532E-07  6.11226902E-11-2.84116471E-15  2
 -1.57972702E+02  3.47602940E+00  2.97996306E+00  4.99669695E-03-3.79099697E-06  3
  2.35419240E-09-8.08902424E-13  1.76227387E+02  9.22272396E+00  4
H2     KEE87H  2      G  0300.00  5000.00  1000.00  1
  0.02991423E+02  0.07000644E-02-0.05633828E-06-0.09231578E-10  0.15827519E-14  2
 -0.08350340E+04-0.13551101E+01  0.03298124E+02  0.08249441E-02-0.08143015E-05  3
 -0.09475434E-09  0.04134872E-11-0.10125209E+04-0.03294094E+02  4
H2O    KEE87H  2O    1      G  0300.00  5000.00  1000.00  1
  0.02672145E+02  0.03056293E-01-0.08730260E-05  0.12009964E-09-0.06391618E-13  2
 -0.02989921E+06  0.06862817E+02  0.03386842E+02  0.03474982E-01-0.06354696E-04  3
  0.06968581E-07-0.02506588E-10-0.03020811E+06  0.02590232E+02  4
H2O2   KEE87H  2O    2      G  0300.00  5000.00  1000.00  1
  0.04573167E+02  0.04336136E-01-0.14746888E-05  0.02348903E-08-0.14316536E-13  2

```

-0.01800696E+06	0.05011369E+01	0.03388753E+02	0.06569226E-01	-0.14850125E-06	3
-0.04625805E-07	0.02471514E-10	-0.01766314E+06	0.06785363E+02		4
N2	KEE87N	2	G	0300.00 5000.00 1000.00	1
0.02926640E+02	0.14879768E-02	-0.05684760E-05	0.10097038E-09	-0.06753351E-13	2
-0.09227977E+04	0.05980528E+02	0.03298677E+02	0.14082404E-02	-0.03963222E-04	3
0.05641515E-07	-0.02444854E-10	-0.10208999E+04	0.03950372E+02		4
O	KEE87O	1	G	0300.00 5000.00 1000.00	1
0.02542059E+02	-0.02755061E-03	-0.03102803E-07	0.04551067E-10	-0.04368051E-14	2
0.02923080E+06	0.04920308E+02	0.02946428E+02	-0.16381665E-02	0.02421031E-04	3
-0.16028431E-08	0.03890696E-11	0.02914764E+06	0.02963995E+02		4
O2	KEE87O	2	G	0300.00 5000.00 1000.00	1
0.03697578E+02	0.06135197E-02	-0.12588420E-06	0.01775281E-09	-0.11364354E-14	2
-0.12339301E+04	0.03189165E+02	0.03212936E+02	0.11274864E-02	-0.05756150E-05	3
0.13138773E-08	-0.08768554E-11	-0.10052490E+04	0.06034737E+02		4
CH	KEE87C	1H 1	G	0300.00 5000.00 1000.00	1
0.02196223E+02	0.02340381E-01	-0.07058201E-05	0.09007582E-09	-0.03855040E-13	2
0.07086723E+06	0.09178373E+02	0.03200202E+02	0.02072875E-01	-0.05134431E-04	3
0.05733890E-07	-0.01955533E-10	0.07045259E+06	0.03331587E+02		4
HCO	KEE87H	1C 1O 1	G	0300.00 5000.00 1000.00	1
0.03557271E+02	0.03345572E-01	-0.13350060E-05	0.02470572E-08	-0.01713850E-12	2
0.03916324E+05	0.05552299E+02	0.02898329E+02	0.06199146E-01	-0.09623084E-04	3
0.10898249E-07	-0.04574885E-10	0.04159922E+05	0.08983614E+02		4
CH2	KEE87C	1H 2	G	0250.00 4000.00 1000.00	1
0.03636407E+02	0.01933056E-01	-0.01687016E-05	-0.10098994E-09	0.01808255E-12	2
0.04534134E+06	0.02156560E+02	0.03762237E+02	0.11598191E-02	0.02489585E-05	3
0.08800836E-08	-0.07332435E-11	0.04536790E+06	0.01712577E+02		4
CH2O	KEE87C	1H 2O 1	G	0300.00 5000.00 1000.00	1
0.02995606E+02	0.06681321E-01	-0.02628954E-04	0.04737153E-08	-0.03212517E-12	2
-0.15320369E+05	0.06912572E+02	0.16527311E+01	0.12631439E-01	-0.01888168E-03	3
0.02050031E-06	-0.08413237E-10	-0.14865404E+05	0.13784820E+02		4
CH3	KEE87C	1H 3	G	0300.00 5000.00 1000.00	1
0.02844051E+02	0.06137974E-01	-0.02230345E-04	0.03785161E-08	-0.02452159E-12	2
0.16437809E+05	0.05452697E+02	0.02430442E+02	0.11124099E-01	-0.01680220E-03	3
0.16218288E-07	-0.05864952E-10	0.16423781E+05	0.06789794E+02		4
CH2OH	KEE87H	3C 1O 1	G	0250.00 4000.00 1000.00	1
0.06327520E+02	0.03608270E-01	-0.03201547E-05	-0.01938750E-08	0.03509704E-12	2
-0.04474509E+05	-0.08329365E+02	0.02862628E+02	0.10015273E-01	-0.05285435E-05	3
-0.05138539E-07	0.02246041E-10	-0.03349678E+05	0.10397938E+02		4
CH3O	KEE87C	1H 3O 1	G	0300.00 3000.00 1000.00	1
0.03770799E+02	0.07871497E-01	-0.02656384E-04	0.03944431E-08	-0.02112616E-12	2
0.12783252E+03	0.02929575E+02	0.02106204E+02	0.07216595E-01	0.05338472E-04	3
-0.07377636E-07	0.02075610E-10	0.09786011E+04	0.13152177E+02		4
CH4	KEE87C	1H 4	G	0300.00 5000.00 1000.00	1
0.01683478E+02	0.10237236E-01	-0.03875128E-04	0.06785585E-08	-0.04503423E-12	2
-0.10080787E+05	0.09623395E+02	0.07787415E+01	0.01747668E+00	-0.02783409E-03	3
0.03049708E-06	-0.12239307E-10	-0.09825229E+05	0.13722195E+02		4
CH3OH	KEE87C	1H 4O 1	G	0300.00 5000.00 1000.00	1
0.04029061E+02	0.09376593E-01	-0.03050254E-04	0.04358793E-08	-0.02224723E-12	2
-0.02615791E+06	0.02378195E+02	0.02660115E+02	0.07341508E-01	0.07170050E-04	3
-0.08793194E-07	0.02390570E-10	-0.02535348E+06	0.11232631E+02		4
CO	KEE87C	1O 1	G	0300.00 5000.00 1000.00	1
3.02507806E+00	1.44268852E-03	-5.63082779E-07	1.01858133E-10	-6.91095156E-15	2
-1.42683496E+04	6.10821772E+00	3.26245165E+00	1.51194085E-03	-3.88175522E-06	3

5.58194424E-09-2.47495123E-12-1.43105391E+04	4.84889698E+00	4
CO2	KEE87C 1O 2 G 0300.00 5000.00 1000.00	1
4.45362282E+00 3.14016873E-03-1.27841054E-06	2.39399667E-10-1.66903319E-14	2
-4.89669609E+04-9.55395877E-01 2.27572465E+00	9.92207229E-03-1.04091132E-05	3
6.86668678E-09-2.11728009E-12-4.83731406E+04	1.01884880E+01	4
C2H	KEE87C 2H 1 G 0300.00 5000.00 1000.00	1
0.04427688E+02 0.02216268E-01-0.06048952E-05	0.09882517E-09-0.07351179E-13	2
0.06590415E+06-0.11994418E+01 0.03050667E+02	0.06051674E-01-0.04956634E-04	3
0.02804159E-07-0.08193332E-11 0.06630011E+06	0.05954361E+02	4
HCCO	KEE87H 1C 2O 1 G 0300.00 4000.00 1000.00	1
0.06758073E+02 0.02000400E-01-0.02027607E-05-0.10411318E-09	0.01965164E-12	2
0.01901513E+06-0.09071262E+02 0.05047965E+02	0.04453478E-01 0.02268282E-05	3
-0.14820945E-08 0.02250741E-11 0.01965891E+06	0.04818439E+01	4
C2H2	KEE87C 2H 2 G 0300.00 5000.00 1000.00	1
4.43677044E+00 5.37603907E-03-1.91281674E-06	3.28637895E-10-2.15670953E-14	2
2.56676641E+04-2.80033827E+00 2.01356220E+00	1.51904458E-02-1.61631888E-05	3
9.07899178E-09-1.91274600E-12 2.61244434E+04	8.80537796E+00	4
CH2CO	KEE87C 2H 2O 1 G 0300.00 5000.00 1000.00	1
0.06038817E+02 0.05804840E-01-0.01920953E-04	0.02794484E-08-0.14588676E-13	2
-0.08583402E+05-0.07657581E+02 0.02974970E+02	0.12118712E-01-0.02345045E-04	3
-0.06466685E-07 0.03905649E-10-0.07632636E+05	0.08673553E+02	4
C2H3	KEE87C 2H 3 G 0300.00 5000.00 1000.00	1
5.93346787E+00 4.01774561E-03-3.96673954E-07-1.44126655E-10	2.37864351E-14	2
3.18543457E+04-8.53031254E+00 2.45927644E+00	7.37147639E-03 2.10987287E-06	3
-1.32164213E-09-1.18478383E-12 3.33522500E+04	1.15562019E+01	4
C2H4	KEE87C 2H 4 G 0300.00 5000.00 1000.00	1
3.52841878E+00 1.14851845E-02-4.41838529E-06	7.84460053E-10-5.26684849E-14	2
4.42828857E+03 2.23038912E+00-8.61487985E-01	2.79616285E-02-3.38867721E-05	3
2.78515220E-08-9.73787891E-12 5.57304590E+03	2.42114868E+01	4
CH3CHO	KEE87C 2O 1H 4 G 0300.00 5000.00 1000.00	1
0.05868650E+02 0.10794241E-01-0.03645530E-04	0.05412912E-08-0.02896844E-12	2
-0.02264568E+06-0.06012946E+02 0.02505695E+02	0.13369907E-01 0.04671953E-04	3
-0.11281401E-07 0.04263566E-10-0.02124588E+06	0.13350887E+02	4
C2H4O	BURC84C 2H 4O 1 G 0300.00 5000.00	1
0.59249249E+01 0.11120714E-01-0.37434083E-05	0.55413918E-09-0.29549886E-13	2
-0.93028008E+04-0.93792849E+01-0.24173594E+00	0.20761095E-01 0.21481201E-05	3
-0.16948157E-07 0.81075771E-11-0.71720117E+04	0.24432190E+02	4
C2H5	KEE87C 2H 5 G 0300.00 5000.00 1000.00	1
0.07190480E+02 0.06484077E-01-0.06428064E-05-0.02347879E-08	0.03880877E-12	2
0.10674549E+05-0.14780892E+02 0.02690701E+02	0.08719133E-01 0.04419838E-04	3
0.09338703E-08-0.03927773E-10 0.12870404E+05	0.12138195E+02	4
C2H6	KEE87C 2H 6 G 0300.00 4000.00 1000.00	1
0.04825938E+02 0.13840429E-01-0.04557258E-04	0.06724967E-08-0.03598161E-12	2
-0.12717793E+05-0.05239506E+02 0.14625388E+01	0.15494667E-01 0.05780507E-04	3
-0.12578319E-07 0.04586267E-10-0.11239176E+05	0.14432295E+02	4
C3H3	KEE87C 3H 3 G 0300.00 3000.00 1000.00	1
0.80916252E+01 0.37372850E-02 0.13886647E-05-0.12298604E-08	0.20681585E-12	2
0.35437793E+05-0.18204468E+02 0.25097322E+01	0.17103866E-01-0.45710858E-05	3
-0.82841574E-08 0.54362287E-11 0.37040680E+05	0.11011264E+02	4
AC3H4	KEE87C 3H 4 G 0300.00 5000.00 1000.00	1
5.72914410E+00 1.23680448E-02-4.80562676E-06	8.60136407E-10-5.81280223E-14	2
2.01298418E+04-9.44866753E+00-2.13196874E-01	3.35871354E-02-3.80487036E-05	3
2.74583787E-08-8.69004434E-12 2.16204844E+04	2.02939262E+01	4

PC3H4	KEE87C	3H	4	G	0300.00	5000.00	1000.00	1	
0.05511034E+02	0.12469562E-01	-0.04814164E-04	0.08573770E-08	-0.05771561E-12				2	
0.01961967E+06	-0.10794748E+02	0.06271447E+01	0.03116179E+00	-0.03747663E-03				3	
0.02964117E-06	-0.09987381E-10	0.02083492E+06	0.13468796E+02					4	
AC3H5	KEE87C	3H	5	G	0300.00	5000.00		1	
0.79091978E+01	0.12115255E-01	-0.41175863E-05	0.61566796E-09	-0.33235733E-13				2	
0.12354156E+05	-0.19672333E+02	-0.54100400E+00	0.27284101E-01	-0.96365329E-06				3	
-0.19129462E-07	0.98394175E-11	0.15130395E+05	0.26067337E+02					4	
SC3H5	KEE87C	3H	5	G	0300.00	5000.00		1	
0.79091978E+01	0.12115255E-01	-0.41175863E-05	0.61566796E-09	-0.33235733E-13				2	
0.12354156E+05	-0.19672333E+02	-0.54100400E+00	0.27284101E-01	-0.96365329E-06				3	
-0.19129462E-07	0.98394175E-11	0.15130395E+05	0.26067337E+02					4	
TC3H5	KEE87C	3H	5	G	0300.00	5000.00		1	
0.79091978E+01	0.12115255E-01	-0.41175863E-05	0.61566796E-09	-0.33235733E-13				2	
0.12354156E+05	-0.19672333E+02	-0.54100400E+00	0.27284101E-01	-0.96365329E-06				3	
-0.19129462E-07	0.98394175E-11	0.15130395E+05	0.26067337E+02					4	
C3H6	KEE87C	3H	6	G	0300.00	5000.00	1000.00	1	
0.06732257E+02	0.14908336E-01	-0.04949899E-04	0.07212022E-08	-0.03766204E-12				2	
-0.09235703E+04	-0.13313348E+02	0.14933071E+01	0.02092517E+00	0.04486794E-04				3	
-0.16689121E-07	0.07158146E-10	0.10748264E+04	0.16145340E+02					4	
C3H6O	BURC84C	3H	6O	1	G	0300.00	5000.00	1	
0.87072573E+01	0.15987653E-01	-0.53762797E-05	0.79422535E-09	-0.42212622E-13				2	
-0.69370352E+04	-0.22579315E+02	0.48378503E+00	0.28574701E-01	0.28022350E-05				3	
-0.22371523E-07	0.10581544E-10	-0.40665557E+04	0.22616104E+02					4	
IC3H7	KEE87C	3H	7	G	0300.00	5000.00	1000.00	1	
0.08063369E+02	0.15744876E-01	-0.05182391E-04	0.07477245E-08	-0.03854422E-12				2	
0.05313871E+05	-0.02192646E+03	0.01713299E+02	0.02542616E+00	0.15808083E-05				3	
-0.01821286E-06	0.08827710E-10	0.07535808E+05	0.12979008E+02					4	
NC3H7	KEE87C	3H	7	G	0300.00	5000.00	1000.00	1	
0.07978290E+02	0.15761134E-01	-0.05173243E-04	0.07443892E-08	-0.03824978E-12				2	
0.07579402E+05	-0.01935611E+03	0.01922536E+02	0.02478927E+00	0.01810249E-04				3	
-0.01783265E-06	0.08582996E-10	0.09713281E+05	0.13992715E+02					4	
C3H8	KEE87C	3H	8	G	0300.00	5000.00	1000.00	1	
0.07525217E+02	0.01889034E+00	-0.06283924E-04	0.09179373E-08	-0.04812410E-12				2	
-0.16464548E+05	-0.01784390E+03	0.08969208E+01	0.02668986E+00	0.05431425E-04				3	
-0.02126000E-06	0.09243330E-10	-0.13954918E+05	0.01935533E+03					4	
C4H	KEE87C	4H	1	G	0300.00	5000.00	1000.00	1	
0.06242882E+02	0.06193682E-01	-0.02085931E-04	0.03082203E-08	-0.16364826E-13				2	
0.07568019E+06	-0.07210806E+02	0.05023247E+02	0.07092375E-01	-0.06073762E-07				3	
-0.02275752E-07	0.08086994E-11	0.07623812E+06	-0.06942594E+00					4	
C4H2	KEE87C	4H	2	G	0300.00	5000.00	1000.00	1	
0.09031407E+02	0.06047252E-01	-0.01948788E-04	0.02754863E-08	-0.13856080E-13				2	
0.05294735E+06	-0.02385067E+03	0.04005191E+02	0.01981000E+00	-0.09865877E-04				3	
-0.06635158E-07	0.06077413E-10	0.05424065E+06	0.01845736E+02					4	
C4H3	KEE87C	4H	3	G	0300.00	5000.00	1000.00	1	
0.84874201E+01	0.86908937E-02	-0.28544437E-05	0.41200798E-09	-0.21301093E-13				2	
0.47970555E+05	-0.19018509E+02	0.35539713E+01	0.19461986E-01	-0.48102484E-05				3	
-0.97301225E-08	0.62390535E-11	0.49453863E+05	0.70829868E+01					4	
C4H6	KEE87C	4H	6	G	0300.00	5000.00	1000.00	1	
8.04658318E+00	1.64852515E-02	-5.52222718E-06	8.12359291E-10	-4.29507843E-14				2	
1.37013047E+04	-1.80045776E+01	3.19710827E+00	2.02559158E-02	6.51019218E-06				3	
-1.65844227E-08	6.40028221E-12	1.57152031E+04	9.89566040E+00					4	
C4H7	3/29/92 THERMC	4H	7	0	OG	300.000	5000.000	1403.000	1

1.05935646E+01	1.60463506E-02	-5.34797608E-06	8.15542396E-10	-4.67160653E-14	2
9.20905760E+03	-3.05278591E+01	8.65239759E-01	3.91949210E-02	-2.66899074E-05	3
9.88387503E-09	-1.53932827E-12	1.25601669E+04	2.15924380E+01		4
PC4H8	KEE87C	4H	8	G	0300.00 5000.00 1000.00
0.02053584E+02	0.03435050E+00	-0.15883196E-04	0.03308966E-07	-0.02536104E-11	2
-0.02139723E+05	0.15543201E+02	0.11811380E+01	0.03085338E+00	0.05086524E-04	3
-0.02465488E-06	0.11110192E-10	-0.01790400E+05	0.02106247E+03		4
TRAC4H8	BURC84C	4H	8	0	OG 300.000 5000.000
0.82797676E+00	0.35864539E-01	-0.16634498E-04	0.34732759E-08	-0.26657398E-12	2
-0.30521033E+04	0.21342545E+02	0.12594252E+01	0.27808424E-01	0.87013932E-05	3
-0.24402205E-07	0.98977710E-11	-0.29647742E+04	0.20501129E+02		4

END

REACTIONS

H+H+M = H2+M	7.310E+17	-1.0	0.0
O+O+M = O2+M	1.140E+17	-1.0	0.0
O+H+M = OH+M	6.200E+16	-0.6	0.0
H2+O2 = OH+OH	1.700E+13	0.0	47800.0
O+H2 = OH+H	3.870E+04	2.7	6260.0
H+O2 = OH+O	1.900E+14	0.0	16812.0
H+O2+M = HO2+M	8.000E+17	-0.8	0.0
H+OH+M = H2O+M	8.615E+21	-2.0	0.0
H2+OH = H2O+H	2.161E+08	1.51	3430.0
H2O+O = OH+OH	1.500E+10	1.14	17260.0
HO2+OH = H2O+O2	2.890E+13	0.0	-497.0
HO2+O = OH+O2	1.810E+13	0.0	-400.0
H+HO2 = H2+O2	4.216E+13	0.0	1411.0
H+HO2 = OH+OH	4.951E+13	0.0	143.0
H+HO2 = H2O+O	1.180E+14	0.0	2730.0
HO2+HO2 = H2O2+O2	4.075E+02	3.321	1979.0
OH+OH = H2O2	1.559E+16	-1.508	149.0
H2O2+OH = HO2+H2O	1.783E+12	0.0	326.0
H2O2+H = HO2+H2	1.700E+12	0.0	3750.0
H2O2+H = H2O+OH	1.000E+13	0.0	3590.0
H2O2+O = HO2+OH	2.800E+13	0.0	6400.0
CO+HO2 = CO2+OH	1.500E+14	0.0	23650.0
CO+OH = CO2+H	4.400E+06	1.5	-740.0
CO+O+M = CO2+M	2.830E+13	0.0	-4540.0
CO+O2 = CO2+O	2.530E+12	0.0	47700.0
HCO+M = H+CO+M	1.850E+17	-1.0	17000.0
HCO+OH = CO+H2O	1.000E+14	0.0	0.0
HCO+O = CO+OH	3.000E+13	0.0	0.0
HCO+O = CO2+H	3.000E+13	0.0	0.0
HCO+H = CO+H2	7.224E+13	0.0	0.0
HCO+O2 = CO+HO2	1.175E+09	1.21	-570.0
HCO+CH3 = CO+CH4	1.200E+14	0.0	0.0
HCO+HO2 = CO2+OH+H	3.000E+13	0.0	0.0
HCO+C2H6 = CH2O+C2H5	4.700E+04	2.72	18235.0
HCO+HCO = CH2O+CO	1.800E+13	0.0	0.0
HCO+HCO = H2+CO+CO	3.000E+12	0.0	0.0
CH4 = CH3 + H	2.132E+31	-5.30	104906.0
CH4+HO2 = CH3+H2O2	1.122E+13	0.0	24641.0
CH4+OH = CH3 + H2O	1.548E+07	1.83	2774.0
CH4+O = CH3+OH	6.923E+08	1.56	8486.0

CH4+H = CH3+H2	8.583E+03	3.05	7941.0
CH4+CH2 = CH3+CH3	4.300E+12	0.0	10038.0
CH3+M = CH2+H+M	1.900E+16	0.0	91600.0
CH3+HO2 = CH3O+OH	4.000E+13	0.0	5000.0
CH4+O2 = CH3+HO2	7.630E+13	0.0	58590.0
CH3+OH = CH2OH+H	2.640E+19	-1.8	8068.0
CH3+OH = CH3O+H	5.740E+12	-0.23	13931.0
CH3+OH = CH2+H2O	8.900E+18	-1.8	8067.0
CH3+OH = CH2O+H2	3.190E+12	-0.53	10810.0
CH3+O = CH2O+H	8.430E+13	0.0	0.0
CH3+H = CH2+H2	7.000E+13	0.0	15100.0
CH3+O2 = CH3O+O	6.000E+12	0.0	33700.0
CH3+O2 = CH2O+OH	3.053E+30	-4.69	36571.0
CH3+CH3 = C2H5+H	3.011E+13	0.0	13513.0
CH3+CH3 = C2H6	2.393E+38	-7.581	11359.0
CH3+CH3O = CH4+CH2O	2.409E+13	0.0	0.0
CH3+CH2OH = CH4+CH2O	2.410E+12	0.0	0.0
CH2+OH = CH+H2O	1.130E+07	2.0	3000.0
CH2+OH = CH2O+H	2.500E+13	0.0	0.0
CH2+O = CO+H+H	9.080E+13	0.0	656.0
CH2+O = CO+H2	3.890E+13	0.0	-149.0
CH2+H = CH+H2	5.517E+12	0.0	-2026.0
CH2+O2 = HCO+OH	4.300E+10	0.0	-500.0
CH2+O2 = CO2+H2	6.900E+11	0.0	500.0
CH2+O2 = CO2+H+H	1.600E+12	0.0	1000.0
CH2+O2 = CO+H2O	1.870E+10	0.0	-1000.0
CH2+O2 = CO+OH+H	8.640E+10	0.0	-500.0
CH2+O2 = CH2O+O	1.000E+14	0.0	4500.0
CH2+CO2 = CH2O+CO	1.100E+11	0.0	1000.0
CH2+CH2 = C2H2+H2	3.200E+13	0.0	0.0
CH2+CH3 = C2H4+H	4.000E+13	0.0	0.0
CH2+CH = C2H2+H	4.000E+13	0.0	0.0
CH2+C2H2 = H+C3H3	1.200E+13	0.0	6620.0
CH2+C2H4 = C3H6	4.300E+12	0.0	10038.0
CH2+C2H6 = CH3+C2H5	6.500E+12	0.0	7911.0
CH2+C3H8 = CH3+IC3H7	2.190E+12	0.0	6405.0
CH2+C3H8 = CH3+NC3H7	1.790E+12	0.0	6405.0
CH+OH = HCO+H	3.000E+13	0.0	0.0
CH+O = CO+H	1.000E+14	0.0	0.0
CH+O2 = HCO+O	3.300E+13	0.0	0.0
CH+O2 = CO+OH	2.000E+13	0.0	0.0
CH+CO2 = HCO+CO	3.400E+12	0.0	690.0
CH+CH4 = C2H4+H	6.000E+13	0.0	0.0
CH+CH3 = C2H3+H	3.000E+13	0.0	0.0
CH3O+M = CH2O+H+M	4.880E+15	0.0	22773.0
CH3O+HO2 = CH2O+H2O2	3.000E+11	0.0	0.0
CH3O+OH = CH2O+H2O	1.000E+13	0.0	0.0
CH3O+O = CH2O+OH	1.300E+13	0.0	0.0
CH3O+H = CH2O+H2	2.000E+13	0.0	0.0
CH3O+O2 = CH2O+HO2	2.349E+10	0.0	1788.0
CH3O+CH2O = CH3OH+HCO	1.150E+11	0.0	1280.0
CH3O+CO = CH3+CO2	1.566E+13	0.0	11804.0
CH3O+HCO = CH3OH+CO	9.000E+13	0.0	0.0



CH3O+C2H5 = CH2O+C2H6	2.410E+13	0.0	0.0
CH3O+C2H3 = CH2O+C2H4	2.410E+13	0.0	0.0
CH3O+C2H4 = CH2O+C2H5	1.200E+11	0.0	7000.0
CH2O+M = HCO+H+M	5.720E+16	0.0	76480.0
CH2O+HO2 = HCO+H2O2	4.000E+12	0.0	11665.0
CH2O+OH = HCO+H2O	3.433E+09	1.18	-447.0
CH2O+O = HCO+OH	1.807E+13	0.0	3088.0
CH2O+H = HCO+H2	1.116E+08	1.685	2127.0
CH2O+O2 = HCO+HO2	2.040E+13	0.0	39000.0
CH2O+CH3 = HCO+CH4	3.224E-04	5.011	3160.0
C2H6 = C2H5+H	2.080E+38	-7.08	106507.0
C2H6+HO2 = C2H5+H2O2	1.210E+12	0.0	17600.0
C2H6+OH = C2H5+H2O	5.125E+06	2.06	860.0
C2H6+O = C2H5+OH	1.144E-07	6.5	274.0
C2H6+H = C2H5+H2	5.000E+02	3.5	5210.0
C2H6+O2 = C2H5+HO2	1.000E+13	0.0	51000.0
C2H6+CH3O = C2H5+CH3OH	3.020E+11	0.0	7000.0
C2H6+CH3 = C2H5+CH4	3.969E+05	2.5	17684.0
C2H5+HO2 = C2H4+H2O2	3.000E+11	0.0	0.0
C2H5+HO2 = CH3+CH2O+OH	2.500E+13	0.0	0.0
C2H5+OH = C2H4+H2O	2.409E+13	0.0	0.0
C2H5+OH = CH3+CH2O+H	2.409E+13	0.0	0.0
C2H5+O = CH2O+CH3	4.238E+13	0.0	0.0
C2H5+O = C2H4+OH	3.046E+13	0.0	0.0
C2H5+H = C2H4+H2	1.250E+14	0.0	8000.0
C2H5+O2 = C2H4+HO2	1.700E+10	0.0	-670.0
C2H5+CH3 = C2H4+CH4	4.265E-04	5.0	8300.0
C2H5+C2H5 = C2H4+C2H6	1.400E+12	0.0	0.0
C2H4+M = C2H2+H2+M	3.000E+17	0.0	79350.0
C2H4+M = C2H3+H+M	2.970E+17	0.0	96560.0
C2H4+HO2 = C2H4O+OH	6.224E+12	0.0	18962.0
C2H4+OH = C2H3+H2O	2.024E+13	0.0	5960.0
C2H4+O = CH3+HCO	1.084E+14	0.0	7432.0
C2H4+O = CH2+HCO+H	5.661E+12	0.0	1488.0
C2H4+H = C2H3+H2	1.325E+06	2.53	12241.0
C2H4+H = C2H5	1.051E+14	-0.5	655.0
C2H4+O2 = C2H3+HO2	4.000E+13	0.0	61500.0
C2H4+C2H4 = C2H5+C2H3	5.000E+14	0.0	64700.0
C2H4+CH3 = C2H3+CH4	3.970E+05	2.5	20000.0
C2H4O = CH3+HCO	3.160E+14	0.0	57000.0
C2H3 = C2H2+H	2.164E+44	-8.447	51106.0
C2H3+HO2 = CH3+CO+OH	3.000E+13	0.0	0.0
C2H3+OH = C2H2+H2O	3.000E+13	0.0	0.0
C2H3+O = CH3+CO	3.000E+13	0.0	0.0
C2H3+H = C2H2+H2	3.000E+13	0.0	0.0
C2H3+O2 = CH2O+HCO	3.000E+12	0.0	-250.0
C2H3+CH3 = C2H2+CH4	4.365E-04	5.0	8300.0
C2H3+C2H6 = C2H4+C2H5	1.500E+13	0.0	10000.0
C2H3+HCO = C2H4+CO	9.034E+13	0.0	0.0
C2H3+CH2O = C2H4+HCO	5.420E+03	2.81	5862.0
C2H3+C2H3 = C2H2+C2H4	1.084E+13	0.0	0.0
C2H3+C2H3 = C4H6	4.938E+13	0.0	0.0
C2H2 = C2H+H	2.372E+32	-5.28	130688.0

C2H2+HO2 = CH2CO+OH	1.000E+13	0.0	18280.0
C2H2+OH = C2H+H2O	3.385E+07	2.0	14000.0
C2H2+OH = CH2CO+H	2.192E-04	4.5	-1000.0
C2H2+OH = CH3+CO	4.848E-04	4.0	-2000.0
C2H+H2 = C2H2+H	4.090E+05	2.39	864.0
C2H2+O = CH2+CO	2.168E+06	2.09	1562.0
C2H2+O = HCCO+H	5.059E+06	2.09	1562.0
C2H2+O2 = HCCO+OH	2.000E+08	1.5	30100.0
C2H2+O2 = C2H+HO2	1.200E+13	0.0	74520.0
C2H2+CH3 = SC3H5	1.610E+40	-8.58	20331.0
PC3H4+H = C2H2+CH3	1.300E+05	2.5	1000.0
C2H2+CH3 = AC3H5	2.610E+46	-9.82	36951.0
C2H2+CH3 = AC3H4+H	6.740E+19	-2.08	31591.0
C2H+OH = HCCO+H	2.000E+13	0.0	0.0
C2H+O = CO+CH	1.000E+13	0.0	0.0
C2H+O2 = CO+CO+H	2.530E+13	0.0	0.0
CH2CO+M = CH2+CO+M	4.110E+15	0.0	59270
CH2CO+O2 = CH2O+CO2	2.000E+13	0.0	61500
CH2CO+HO2 = CH2O+CO+OH	6.000E+11	0.0	12738
CH2CO+OH = HCCO+H2O	7.500E+12	0.0	2000
CH2CO+O = CH2+CO2	1.760E+12	0.0	1349
CH2CO+O = HCCO+OH	1.000E+13	0.0	8000
CH2CO+H = CH3+CO	1.500E+04	2.827	673
CH2CO+H = HCCO+H2	5.000E+13	0.0	8000
HCCO+M = CH+CO+M	6.000E+15	0.0	58821
HCCO+OH = HCO+CO+H	1.000E+13	0.0	0
HCCO+O = CO+CO+H	1.930E+14	0.0	590
HCCO+H = CH2+CO	1.500E+14	0.0	0
HCCO+O2 = CO+CO+OH	1.460E+12	0.0	2500
HCCO+CH2 = C2H+CH2O	1.000E+13	0	2000
HCCO+CH2 = C2H3+CO	3.000E+13	0	0
CH3OH = CH3+OH	1.565E+46	-9.28	103522
CH3OH+HO2 = CH2OH+H2O2	6.300E+12	0	19360
CH3OH+OH = CH2OH+H2O	4.532E+11	0.33	1160
CH3OH+OH = CH3O+H2O	3.629E+11	0.7	5868
CH3OH+O = CH2OH+OH	1.000E+13	0	4690
CH3OH+H = CH2OH + H2	4.000E+13	0	6100
CH3OH+CH2O = CH3O+CH3O	1.549E+12	0	79570
CH3OH+CH3 = CH2OH+CH4	3.566E+11	0	8663
CH3OH+CH3 = CH3O+CH4	4.677E+05	2.328	12764
CH2OH+M = CH2O+H+M	1.000E+14	0	25100
CH2OH+H = CH2O+H2	3.000E+13	0	0
CH2OH+O2 = CH2O+HO2	2.168E+14	0	4690
C3H8 = C2H5+CH3	6.033E+94	-22.7	130427
C3H8+O2 = NC3H7+HO2	4.000E+13	0	47500
C3H8+O2 = IC3H7+HO2	4.000E+13	0	47500
C3H8+HO2 = NC3H7+H2O2	4.760E+04	2.55	16494
C3H8+HO2 = IC3H7+H2O2	9.640E+03	2.6	13910
C3H8+OH = NC3H7+H2O	4.155E+07	1.47	540
C3H8+OH = IC3H7+H2O	1.841E+05	2.38	-573
C3H8+O = NC3H7+OH	3.715E+06	2.4	5505
C3H8+O = IC3H7+OH	5.495E+05	2.5	3140
C3H8+H = NC3H7+H2	1.995E+14	0	9959

C3H8+H = IC3H7+H2	1.300E+13	0	5638
C3H8+CH3 = NC3H7+CH4	3.000E+12	0	11710
C3H8+CH3 = IC3H7+CH4	8.070E+11	0	10110
C3H8+C2H5 = NC3H7+C2H6	3.160E+11	0	12300
C3H8+C2H5 = IC3H7+C2H6	5.010E+10	0	10400
C3H8+C2H3 = NC3H7+C2H4	6.000E+02	3.3	10502
C3H8+C2H3 = IC3H7+C2H4	1.000E+03	3.1	8829
C3H8+IC3H7 = NC3H7+C3H8	1.000E+11	0	12900
C3H8+AC3H5 = NC3H7+C3H6	7.940E+11	0	20500
C3H8+AC3H5 = IC3H7+C3H6	7.940E+11	0	16200
C3H8+CH3O = NC3H7+CH3OH	3.180E+11	0	7050
C3H8+CH3O = IC3H7+CH3OH	7.200E+10	0	4470
NC3H7 = C2H4+CH3	4.070E+12	0	29580
NC3H7+O2 = C3H6+HO2	3.580E+09	0	-3532
IC3H7 = C2H4+CH3	1.000E+14	0	45000
IC3H7+O2 = C3H6+HO2	1.836E+10	0	-2151
C3H6 = AC3H5+H	4.570E+14	0	88900
C3H6 = SC3H5+H	7.590E+14	0	101300
C3H6 = TC3H5+H	1.450E+15	0	98060
C3H6 = C2H3+CH3	7.100E+15	0	87240
C3H6+HO2 = C3H6O+OH	1.020E+12	0	14964
C3H6+HO2 = AC3H5+H2O2	1.500E+11	0	14190
C3H6+HO2 = SC3H5+H2O2	7.500E+09	0	12570
C3H6+HO2 = TC3H5+H2O2	3.000E+09	0	9930
C3H6+OH = AC3H5+H2O	7.698E+05	2.214	622
C3H6+OH = SC3H5+H2O	1.012E+13	0	5960
C3H6+OH = TC3H5+H2O	1.166E+09	0.965	-424
C3H6+OH = C2H5+CH2O	3.914E+145	-40.0	65733
C3H6+O = C2H5+HCO	5.219E+07	1.57	-628
C3H6+O = C2H4+CH2O	3.484E+07	1.57	-628
NC3H7 = C3H6+H	6.300E+13	0	36807
C3H6+H = IC3H7	3.000E+12	0	960
C3H6+H = AC3H5+H2	6.457E+12	0	4445
C3H6+H = SC3H5+H2	3.250E+11	0	4445
C3H6+O2 = SC3H5+HO2	2.000E+13	0	47600
C3H6+O2 = TC3H5+HO2	2.000E+13	0	44000
C3H6+O2 = AC3H5+HO2	1.950E+12	0	39000
C3H6+CH3 = AC3H5+CH4	1.600E+11	0	8800
C3H6+CH3 = SC3H5+CH4	3.300E+11	0	10110
C3H6+CH3 = TC3H5+CH4	5.000E+10	0	8030
C3H6+C2H5 = AC3H5+C2H6	1.000E+11	0	9800
C3H6O => C2H5+HCO	1.260E+14	0	58000
AC3H5+O2 => CH2O+CH2O+CH	6.310E+11	0	17210
AC3H5+HO2 => C2H3+CH2O+OH	4.500E+12	0	0
AC3H5+H = AC3H4+H2	3.333E+12	0	0
AC3H5+O => C2H4+CO+H	1.807E+14	0	0
AC3H5+CH3 = AC3H4+CH4	1.000E+11	0	0
AC3H5+C2H5 = AC3H4+C2H6	4.000E+11	0	0
AC3H5+C2H3 = AC3H4+C2H4	1.000E+12	0	0
SC3H5+HO2 => CH2CO+CH3+OH	4.500E+12	0	0
SC3H5+H = AC3H4+H2	3.333E+12	0	0
SC3H5+O => CH2CO+CH3	1.807E+14	0	0
SC3H5+C2H5 = AC3H4+C2H6	1.000E+11	0	0

SC3H5+C2H3 = AC3H4+C2H4	1.000E+11	0	0
TC3H5+HO2 => CH2CO+CH3+OH	4.500E+12	0	0
TC3H5+H = AC3H4+H2	3.333E+12	0	0
TC3H5+O => HCCO+CH3+H	1.807E+14	0	0
TC3H5+CH3 = AC3H4+CH4	1.000E+11	0	0
TC3H5+C2H5 = AC3H4+C2H6	1.000E+11	0	0
TC3H5+C2H3 = AC3H4+C2H4	1.000E+11	0	0
AC3H4+M = C3H3+H+M	2.000E+18	0	80000
AC3H4+AC3H4 = AC3H5+C3H3	5.000E+14	0	64700
AC3H4 = PC3H4	1.202E+15	0	92400
AC3H4+O2 = C3H3+HO2	4.000E+13	0	61500
AC3H4+HO2 => CH2CO+CH2+OH	8.000E+12	0	19000
AC3H4+OH = CH2CO+CH3	3.120E+12	0	-397
AC3H4+OH = C3H3+H2O	1.445E+13	0	4173
AC3H4+O = C2H3+HCO	1.100E-02	4.613	-4243
AC3H4+H = AC3H5	2.000E+12	0	2700
AC3H4+H = TC3H5	6.500E+12	0	2000
AC3H4+H = C3H3+H2	1.000E+12	0	1500
AC3H4+CH3 = C3H3+CH4	2.000E+12	0	7700
AC3H4+AC3H5 = C3H3+C3H6	2.000E+12	0	7700
AC3H4+C2H = C3H3+C2H2	1.000E+13	0	0
PC3H4+M = C3H3+H+M	4.700E+18	0	80000
PC3H4 = C2H+CH3	4.200E+16	0	100000
PC3H4+O2 => HCCO+OH+CH2	2.000E+08	1.5	30100
PC3H4+O2 = C3H3+HO2	5.000E+12	0	51000
PC3H4+HO2 => C2H4+CO+OH	3.000E+12	0	19000
PC3H4+OH = C3H3+H2O	3.000E+03	3	200
PC3H4+OH = CH2CO+CH3	5.000E-04	4.5	-1000
PC3H4+O = CH2CO+CH2	6.400E+12	0	2010
PC3H4+O = C2H3+HCO	3.200E+12	0	2010
PC3H4+O = HCCO+CH3	6.300E+12	0	2010
PC3H4+O => HCCO+CH2+H	3.200E+11	0	2010
PC3H4+H = TC3H5	6.500E+12	0	2000
PC3H4+H = C3H3+H2	1.000E+12	0	1500
PC3H4+CH3 = C3H3+CH4	2.000E+12	0	7700
PC3H4+C2H = C3H3+C2H2	1.000E+12	0	0
PC3H4+C2H3 = C3H3+C2H4	1.000E+12	0	7700
PC3H4+AC3H5 = C3H3+C3H6	2.000E+12	0	7700
C3H3+O => C2H+HCO+H	1.385E+14	0	0
C3H3+O => C2H2+CO+H	1.400E+14	0	0
C3H3+O2 = CH2CO+HCO	3.010E+10	0	2870
C3H3+CH3 = C2H5+C2H	1.000E+13	0	37500
C3H3+CH3 = C4H6	1.000E+12	0	0
C2H3+C2H4 = C4H6+H	1.000E+12	0	7300
C2H2+C2H2 = C4H3+H	2.000E+12	0	45900
C2H2+C2H = C4H2+H	3.500E+13	0	0
C4H3+M = C4H2+H+M	1.000E+16	0	59700
C4H7 = C4H6+H	1.200E+14	0	49300
C4H7 = C2H4+C2H3	1.000E+11	0	37000
C4H7+H = C4H6+H2	3.160E+12	0	0
C4H7+O2 = C4H6+HO2	1.000E+11	0	0
C4H7+CH3 = C4H6+CH4	1.000E+13	0	0
C4H7+C2H3 = C4H6+C2H4	4.000E+12	0	0

C4H7+C2H5 = C4H6+C2H6	4.000E+12	0	0
C4H7+AC3H5 = C4H6+C3H6	4.000E+13	0	0
C4H6+OH = AC3H5+CH2O	7.230E+12	0	-994
C4H6+O = C2H4+CH2CO	1.000E+12	0	0
C4H6+O = PC3H4+CH2O	1.000E+12	0	0
C4H2+M = C4H+H+M	3.5000E+17	0	80000
END			

### II.3 References

- A. Burcat, "Thermochemical Data for Combustion Calculations," in W.C. Gardiner, ed., Combustion Chemistry, Springer-Verlag (1984).
- P. Dagaut, M. Cathonnet, and J-C. Boettner, "Kinetics of Ethane Oxidation," *International Journal of Chemical Kinetics*, Vol. 23, 437-455 (1991).
- P. Dagaut, M. Cathonnet, and J-C. Boettner, "Kinetic Modeling of Propane Oxidation and Pyrolysis," *International Journal of Chemical Kinetics*, Vol. 25, 813-837 (1992).
- R.J. Kee, F.M. Rupley, and J.A. Miller, "The CHEMKIN Thermodynamic Data Base," *Sandia National Laboratories Report SAND87-8215B* (1990).